

OPTICAL AND SPIN DYNAMICS OF QUANTUM EMITTERS IN
HEXAGONAL BORON NITRIDE AT ROOM TEMPERATURE

Raj Nanalal Patel

A DISSERTATION

in

Electrical and Systems Engineering

Presented to the Faculties of the University of Pennsylvania

in

Partial Fulfillment of the Requirements for the

Degree of Doctor of Philosophy

2022

Supervisor of Dissertation

Lee C. Bassett, Associate Professor of Electrical and Systems Engineering

Graduate Group Chairperson

Troy Olsson, Associate Professor of Electrical and Systems Engineering

Dissertation Committee

Deep Jariwala, Assistant Professor of Electrical and Systems Engineering

Anthony J. Sigillito, Assistant Professor of Electrical and Systems Engineering

Eric Stach, Robert D. Bent Professor of Engineering, Department of Materials Science and Engineering

OPTICAL AND SPIN DYNAMICS OF QUANTUM EMITTERS IN
HEXAGONAL BORON NITRIDE AT ROOM TEMPERATURE

© COPYRIGHT

2022

Raj Nanalal Patel

This work is licensed under the
Creative Commons Attribution
NonCommercial-ShareAlike 4.0
License

To view a copy of this license, visit

<http://creativecommons.org/licenses/by-nc-sa/4.0/>

Dedicated to my life partner, parents and sisters

ACKNOWLEDGEMENTS

Lee, thank you for giving me the opportunity to be part of the Quantum Engineering Lab. Under your mentorship, I have grown tremendously as a researcher and an individual.

Yung, I cannot imagine the past five years in the lab without you. I have learned a lot from you, both professionally and personally. I cannot thank you enough for all your help, support and advise. You have been there by my side during the best and worst of times, cheering me in my accomplishments and picking me up in my failures. I admire and learn from your dedication and persistence. I will cherish the fond memories of hours long conversations and miss the coffee runs. I cannot ask for a better colleague, but more importantly I cannot ask for a better friend.

Becca, thank you for your friendship. I feel privileged to have worked closely with you. It has been a pleasure to getting to know you. I feel fortunate to have gotten to work, grow, laugh and cry with you. Thank you for your help and support whenever I needed and calling me out on just coffee breakfasts. I will miss our Penn Park walks – talking everything from research to playing twenty questions. While we met as colleagues, I am lucky to have made a lifelong friend.

David, thank you for everything. You have been a great teacher, collaborator and friend since my first day in the lab. I am glad you were always there, be it to build setups, get lunch and coffee, answer quick questions or fix my Git merge errors. I will always be thankful to you for teaching me how to code well, build robust analysis frameworks and do meaningful science. Most importantly, thank you for helping me pull out the magnet having a pull force of over 300 lbs. I greatly appreciate you always instantly walking to lab from office when I come running to you. Thank you for all the baking you and Amy did for the lab. Will miss those tasty treats!

The Quantum Engineering Lab members and alumni - Annemarie, Richard, Benjamin,

Jordan, Sarah, Henry, Joseph, Amelia, Mathieu, Alex, Leah and Winston, it has been a pleasure knowing and working with you. Jordan, thank you for the opportunity to be a mentor to you. Benjamin, I feel lucky to have mentored you and worked with you. You made great contributions to my work having prepared every sample I measured during my PhD. I have learned a lot from your meticulousness. To all of you, I wish you the best of success in all your endeavours.

Abhinav and Jiken, the past few years in Philadelphia wouldn't have been the same without you. Thank you for all the fun times, exciting weekends of board games and cheering me through these past few years. To all my friends, especially Aastha, Nupur, Pratik, Ashima, Nihit, Akhil, Surabhi, Abhinandan, Akhila, Shreyas, Nupura, Sumil and Vishwanth, thank you for your support and encouragement.

To the Agarwal family, thank you for welcoming me into your family. I am grateful for your support and appreciate you celebrating all my accomplishments, big or small. To my uncle Shashi and aunt Shobhna, thank you for being second parents to me and always looking after my well being and success. To my grandmother, aunts Rakhi and Panna, uncles Hitesh and Piyush, cousins Nishtha and Pritesh, and the rest of the family, I greatly appreciate your support and motivation.

Rani and Kushan, thank you for your support and help whenever I needed and encouraging me through all my endeavours. Avani and Rupesh, thank you for always believing in me, supporting and encouraging me. Binny and Brijesh, thank you for always standing behind me and supporting me in every step. Mayur and Meera, thank you for your support and encouragement. I couldn't have accomplished all I have today without the unconditional love and support of you all. I love you all.

To my parents, I don't know where to begin in thanking you. I wouldn't have been where I am today without your help, support and sacrifices. Thank you for always believing in me and supporting me in all my decisions. You have taught me to be kind, helpful, sincere,

honest and selfless. Thank you for teaching me the value of hard work and dedication. Even partially following in your footsteps make me a better person everyday. Thank you for always being there, I love you both.

To my life partner Oshin, I feel the luckiest being with you. Your sincerity, honesty and open-mindedness inspire me to be a better person. As a scientist, your passion, dedication and determination motivates me. I feel the most fortunate to have been on this PhD journey together with you. I couldn't have accomplished all I did the past few years without you. I have smoothly sailed through the most difficult of times because of your unwavering support, help and advise, knowing you will always be there to listen, laugh and cry with me. You are and forever will be the best thing that happened to me. I look forward to the new and exciting chapter of our life together to come. I love you, forever.

ABSTRACT

OPTICAL AND SPIN DYNAMICS OF QUANTUM EMITTERS IN HEXAGONAL BORON NITRIDE AT ROOM TEMPERATURE

Raj Nanalal Patel

Lee C. Bassett

Hexagonal boron nitride (h-BN) is a van der Waals material that hosts defect-based quantum emitters (QEs) at room temperature, providing an unparalleled platform for realizing devices for quantum technologies and studying light-matter interactions. Recent observations suggest the existence of multiple distinct defect structures responsible for QEs. Theoretical proposals suggest vacancies, substitutional atoms, and their complexes as likely defect candidates. However, experimental identification of the QEs' electronic structure is lacking, and key details of the QEs' charge and spin properties remain unknown. This thesis focuses on understanding the optical and spin dynamics of QEs in h-BN at room temperature. Starting with the motivation for studying quantum systems and QEs in Chapter 1, this thesis introduces QEs in h-BN in Chapter 2 and discusses its current understanding in Chapter 3. Chapter 4 discusses the materials and methods developed and utilized during the course of this thesis. Chapter 5 discusses the optical dynamics acquired using photoluminescence spectroscopy and photon emission correlation spectroscopy (PECS) and shows several QEs exhibit pure single-photon emission. It discusses the complex optical dynamics associated with excitation and relaxation through multiple electronic excited states - revealed by PECS and polarization-resolved excitation and emission. Following, it presents the optical dynamics simulations of electronic structure models that are consistent with the observations, and discusses the results in the context of *ab initio* theoretical calculations. Chapter 6 discusses magnetic-field-dependent PECS that can be used as a framework to probe the presence of single spins that are otherwise elusive. Following, it presents detection and confirmation of single spin using optically detected magnetic resonance. Finally, it discusses the

spin dynamics and time-domain measurements acquired using optical and microwave pulse protocols crucial to developing methods to coherently control the QE's spin. To conclude, Chapter 7 discusses the future directions that can help identify the chemical nature of QEs in h-BN and establish it as a scalable material platform for quantum technologies.

TABLE OF CONTENTS

ACKNOWLEDGEMENTS	iv
ABSTRACT	vii
LIST OF TABLES	xii
LIST OF ILLUSTRATIONS	xiii
CHAPTER 1 : Introduction	1
CHAPTER 2 : The Quantum Emitters in Hexagonal Boron Nitride	5
2.1 Solid-State Host Materials: Hexagonal Boron Nitride	5
2.2 Experimental Observations	6
2.3 Proposed Defect Structures	10
2.4 Spin-Based Quantum Emitters	13
2.5 Applications	15
CHAPTER 3 : Current Understanding of Visible Quantum Emitters	20
3.1 Electronic Level Structure, Vibronic and Polarization Properties	20
3.2 Optical Dynamics	21
3.3 Spin Dynamics	22
CHAPTER 4 : Materials and Experimental Methods	24
4.1 Sample Preparation	24
4.2 Experimental Setup	28
4.3 Microwave Chip	31
4.4 Photoluminescence Characterization	32
4.5 Photon Emission Correlation Spectroscopy	34

4.6	Electronic Level Structure Simulations	39
CHAPTER 5 : Optical Dynamics of Quantum Emitters		42
5.1	Introduction	43
5.2	Photoluminescence, Spectral and Polarization Properties	45
5.3	Verifying Single-Photon Emission	51
5.4	Probing the Optical Dynamics	53
5.5	Electronic Model and Optical Dynamics Simulations	56
5.6	Interpreting the Photoluminescence, Spectral and Polarization Properties	58
5.7	Interpreting the Optical Dynamics	62
5.8	Consistency with Theoretical Defect Proposals	65
5.9	Conclusion	67
CHAPTER 6 : Spin Dynamics of Quantum Emitters		69
6.1	Introduction	69
6.2	Searching for Single Spin	71
6.3	Single-Spin Resonance, Zero-Field Splitting and g-factor Anisotropy	76
6.4	Time-Domain and Spin Dynamics	81
6.5	Conclusion	85
CHAPTER 7 : Conclusion and Future Directions		87
APPENDICES		92
APPENDIX A : Experimental Setup		92
APPENDIX B : Custom Software Control		94
APPENDIX C : Annealing Study		97
C.1	Effect of Annealing on Hexagonal Boron Nitride	97
C.2	Effect of Annealing on Microwave Substrates	99

APPENDIX D : Photon Correlations: Acquisition, Analysis and Application	101
D.1 Framework	101
D.2 Automated Processing	102
D.3 Adaptive Fitting	102
APPENDIX E : Optical Dynamics - Supporting Information	105
E.1 Nitrogen Vacancy Center in Diamond	105
E.2 Antibunching Amplitude	106
E.3 Quantum Emitter A	107
E.4 Simulating Optical Dynamics for Non-Zero Ratio of Pumping Rates	108
E.5 Empirical Fits to Photon Emission Statistics	108
E.6 Generalized Electronic Level Structure	112
E.7 Theoretical Calculations	112
BIBLIOGRAPHY	115

LIST OF TABLES

TABLE 1 :	Long-Timescale Autocorrelation Function Fit Parameters.	36
TABLE 2 :	The Samples, Quantum Emitters and Sample Treatments.	45
TABLE 3 :	Steady-State PL as a Function of Power, PL Spectra Analysis and Optical Polarization Properties.	48
TABLE 4 :	Result of Simultaneous Fit of QE C's Emission and Excitation Po- larization.	51
TABLE 5 :	Summary of Annealing Study of Exfoliated h-BN	98
TABLE 6 :	Results of Fitting Empirical Functions in Eq. 5.3a - 5.3d to PECS: Rates	110
TABLE 7 :	Results of Fitting Empirical Functions in Eq. 5.3a - 5.3d to PECS: Amplitudes	111

LIST OF ILLUSTRATIONS

FIGURE 1 : Geometry of Various Proposed Defects in Hexagonal Boron Nitride	11
FIGURE 2 : Fabrication	26
FIGURE 3 : Scanning Electron Microscope and Optical Images	27
FIGURE 4 : Experimental Setup	29
FIGURE 5 : Microwave Circuit for Time-Domain and Spin Dynamics Measurements	30
FIGURE 6 : Microwave Chip	32
FIGURE 7 : Second-Order Photon Autocorrelation Function	35
FIGURE 8 : Photoluminescence Characterization	47
FIGURE 9 : Photoluminescence Emission Lineshapes	49
FIGURE 10 : Quantum Emitter C: Emission and Excitation Polarization with Green Excitation	50
FIGURE 11 : Single-Photon Emission Characteristics	52
FIGURE 12 : Photon Emission Correlation Spectroscopy	55
FIGURE 13 : Electronic Level Structure and Optical Dynamics Simulations	58
FIGURE 14 : Optical and Temporal Characterization	73
FIGURE 15 : Magnetic-Field-Dependent PECS at various Dipole Orientations	75
FIGURE 16 : Photoluminescence at various Dipole Orientations	75
FIGURE 17 : Total Bunching at various Dipole Orientations	76
FIGURE 18 : Optically Detected Magnetic Resonance	77
FIGURE 19 : Optically Detected Magnetic Resonance Contrast and Linewidth	78
FIGURE 20 : Resonance Frequency at various Dipole Orientations	79
FIGURE 21 : Estimating Spin Relaxation and Coherence Times	80
FIGURE 22 : Time-Domain and Spin Dynamics	84
FIGURE 23 : Optical Spin Contrast	85
FIGURE 24 : Signal-to-Noise Ratio	86

FIGURE 25 : Free-Space Optics and Controls	92
FIGURE 26 : Excitation and Collection Optical Paths	93
FIGURE 27 : Sample Stage and Magnetic Field Control	93
FIGURE 28 : Measurement Controls	95
FIGURE 29 : Stage Control	96
FIGURE 30 : Photoluminescence Scan	96
FIGURE 31 : S-Parameters of Microwave Substrates Post Annealing	100
FIGURE 32 : Framework for using Photon Correlations to Model Electronic Level Structure	101
FIGURE 33 : Procedure for Autocorrelation Data Processing and Empirical Fitting	103
FIGURE 34 : Antibunching Rate of NV Centers in Nanodiamonds	105
FIGURE 35 : Antibunching Amplitudes	106
FIGURE 36 : Quantum Emitter A: γ_4 and C_4 for Orange Excitation	107
FIGURE 37 : Quantum Emitter A: Lifetime Measurement	107
FIGURE 38 : Simulating Optical Dynamics of QE A	109
FIGURE 39 : Simulation of Optical Dynamics for Different Γ_{12}/Γ_{13}	109
FIGURE 40 : General Electronic Level Structure	112
FIGURE 41 : Calculated Parameters and Capture Coefficient for Capture of an Electron from the Conduction Band into the Neutral Boron Dan- gling Bond, as a Function of Applied Distortion h	113

CHAPTER 1 : Introduction

Since the information age, computation and information technology have come a long way from the first transistors the size of a hand to billions of transistors on a single chip the size of a fingertip. This translated to first computers that occupied an entire room to today's handheld computers that are not just smaller and portable but more powerful. Over the past few decades, the exponentially growing needs of computing power and information storage led to rapid growth of hardware that enabled faster data processing and communication. This revolutionized every aspect of our lives from being able to accurately predict the weather, making us global citizens with easy and fast access to information and travel, enabling and speeding up discovery of medicines and vaccines, taking us to outer space, and much more. With rapid growth came demand for more computing power and information storage driven by Moore's law that led to doubling of transistors on an integrated circuit every two years as transistor size shrank. As the transistor size approaches that of a few atoms, we are approaching the fundamental limit of how small a transistor can be as well as how many can be packed together, and thus the limits of scaling classical computers. Further, there are various computational problems that cannot be solved by a classical or even a supercomputer altogether.

Quantum mechanics allows us computational power beyond that of classical computers. Instead of a classical bit of a transistor that works as a switch by being in ON or OFF state, a quantum bit can be in a superposition of the two states. In a classical system, N bits would result into a state with each bit being 0 or 1. For instance, a state from 2 classical bits would be either 00, 01, 10 or 11. With N quantum bits, entanglement will result in a general state having 2^N eigenstates. For instance, a state from 2 quantum bits will be an entangled state of 00, 01, 10 and 11, each having a probability such that the total probability is 100%. Thus, compared to classical counterparts, N quantum bits can potentially process and store exponentially more information by representing all 2^N possible states in a single state via entanglement. However, before we throw out our classical computers and replace

them with quantum computers, it is important to understand that quantum computers are not to replace classical computers. Rather, they are to make classically intractable problems possible to solve. When a system with N quantum bits is measured, it collapses into a single state with an associated probability – making it prudent to correct for errors and repeating the measurement several times. Thus, quantum computation is well suited for problems such as optimization where a classical computer would have to individually evaluate 2^N possibilities for N variables, each in 0 or 1 state whereas a quantum computer can evaluate all the possibilities simultaneously.

Today’s quantum computers are as large as their classical counterparts several decades ago. This brings a variety of challenges and opportunities to revolutionize the information technology with the promise and potential of quantum systems governed by principles of quantum mechanics [50]. Quantum systems are promising for various applications such as quantum computing [58, 183], sensing [174] and communication [79]. A variety of technological platforms exist that enable quantum systems both for fundamental understanding as well as scalable technologies [32]. The list includes optical defects in solid-state materials [13, 16, 20], superconducting circuits [53, 224], trapped ions and atoms [45, 145], and photonic circuits [113]. Each of the platform has its own advantages and disadvantages. Several solid-state materials that host optically addressable spins have one distinct advantage - it gives rise to quantum coherent properties at room temperature [20, 101, 214]. Compared to quantum systems that strictly operate inside a dilution refrigerator, that is a tremendous advantage that opens up multitude of practical applications.

In the last couple of decades, multiple solid-state materials have emerged for realizing quantum technologies [105, 226]. Solid-state systems such as diamond and silicon carbide have emerged as favorable hosts of optical defects that give rise to quantum emission, commonly known as quantum emitters (QEs) [4, 13, 20, 226]. These are single-photon emitters (SPEs) and some of them have optically-addressable spin, making them ideal for light-matter interface or building spin qubits [17]. Compared to other quantum systems,

solid-state spins' robustness to decoherence at room temperature make them well suited for quantum applications such as memory [29], sensing [3, 51, 174] and communication [79]. More recently, two-dimensional materials have garnered interests as novel solid-state systems for quantum applications [5, 37, 65, 194]. Hexagonal boron nitride (h-BN) has gained the most attention as a wide bandgap (~ 6 eV) material which hosts QEs from ultraviolet to infrared. Within last couple of years, some of these QEs have been found to exhibit spin-dependent fluorescence [39, 66, 83, 184]. The presence of single-photon sources and single spins at room temperature combined with low dimensionality make h-BN a unique material for quantum technological applications. However, even as wide range of quantum defects have been shown in h-BN, the identification and creation of these defects prove to be challenging. While theoretical predictions exist [209], conclusive experimental evidence of QEs' electronic and chemical structure remains elusive.

Interest in h-BN defects go back several decades [10, 106, 230]. The first report in 2016 of quantum emission from defects in h-BN [193] sparked a great interest in understanding its nature and applications, resulting in over 250 published reports since then. The established technique of tape-exfoliation of van der Waals materials enabled low barrier entry to studying quantum defects in h-BN. In the past few years, rapid progress has been made in understanding the photophysical properties of QEs in h-BN and its potential applications. However, the nature of defects giving rise to quantum emission remain unknown. The heterogeneity of QEs make it challenging to identify the underlying defect structures. While optically-addressable spins have been observed, their origin as well as spin dynamics remain unresolved. Experimental confirmation of electronic and chemical structure of QEs in h-BN will provide the foundation to further develop h-BN as a solid-state quantum platform. The work discussed here is aimed in that direction with the overarching goal of conclusively identifying QEs in h-BN. Two groundbreaking developments in this thesis are the first ever reported observation of pure single-photon emission and first observation of pure single-photon emitter with spin at room temperature. These are major results that solidifies the position of QEs in h-BN as a leading platform for room-temperature quantum

technologies that require single-photon emission and single spins.

This thesis is geared toward answering some of the key outstanding questions regarding QEs in h-BN – its optical and spin dynamics. This thesis focuses on probing the optical and spin dynamics crucial to optical coherent control of spin. Probing the optical dynamics provide a framework for predicting the electronic level structure using photon emission correlation spectroscopy (PECS) that can aid in designing experiments geared toward answering specific unknowns such as presence of charge and spin manifolds. This is a powerful technique because not only can it confirm single-photon emission, it can also provide us further insight regarding the electronic level structure and bring us one step closer to identifying the defect. Probing the spin dynamics help understand spin transitions crucial to understanding the electronic level structure of QEs with spin degree of freedom. The presence of spin opens new avenues of study on light-matter interaction in two-dimensional materials as well as applications. Furthermore, the methods discussed in this thesis can be readily applied to other solid-state systems.

The remaining chapters are organized as follows: Chapter 2 introduces the QEs in h-BN and discusses observed photophysical properties, theoretical and experimental defect proposals along with spin-based QEs and applications; Chapter 3 reviews visible QEs discussing the current understanding of its electronic level structure along with vibronic and polarization properties and optical and spin dynamics; Chapter 4 overviews the materials - sample preparation and fabrication techniques, experimental methodology and numerical simulations that enabled the work presented in this thesis; Chapter 5 discusses probing the optical dynamics of QEs at room temperature using photoluminescence spectroscopy and PECS and modeling the electronic level structure; Chapter 6 discusses the framework based on PECS for finding single spins, confirmation of spin using optically detected magnetic resonance (ODMR) and probing its optical and spin dynamics using optical and microwave pulse protocols, all at room temperature; and Chapter 7 concludes this thesis and discusses the future directions.

CHAPTER 2 : The Quantum Emitters in Hexagonal Boron Nitride

This chapter introduces the QEs in h-BN and is organized as follows: Section 2.1 discusses the properties of h-BN and its advantages as a host material; Section 2.2 discusses experimental observations of QEs in h-BN; Section 2.3 discusses the theoretical and experimental proposals of the underlying defect structures that give rise to quantum emission; Section 2.4 focuses on the QEs having spin properties; and Section 2.5 discusses the applications of QEs in h-BN.

2.1. Solid-State Host Materials: Hexagonal Boron Nitride

A plethora of solid-state materials are host to quantum defects [4, 20, 226]. Some of the most well studied materials include diamond, silicon carbide and zinc oxide. However, new host materials [105] continue to be explored in search of the quantum defect that can be the basis of a perfect qubit [214]. More recently, two-dimensional materials have garnered interest as novel solid-state systems for quantum applications. H-BN is a wide-bandgap (~ 6 eV) [36] van der Waals material that hosts defect-based QEs in ultraviolet (UV) to infrared (IR) [83, 143, 193, 206]. The QEs arise from quantum defects that are located deep within the h-BN bandgap. The QEs in h-BN are bright and photostable with narrow emission linewidths and high single-photon purity, as required for quantum technologies [37, 55, 65, 111, 155]. Recent observations of room-temperature magnetic-field dependence and spin resonance of QEs in h-BN make them attractive for spin-based quantum sensing and computation [39, 56, 66, 82, 83, 147, 184]. The QEs in h-BN could be favorable for applications compared to other systems such as nitrogen vacancy center in diamond or divacancy in silicon carbide due to its high Debye-Waller factor which ensures maximum fraction of photons emitted into the zero-phonon line (ZPL), polarized absorption and emission, room-temperature operation, and more [226]. Compared to bulk host materials, h-BN's low dimensionality could enable unique applications from integration with other materials as well as the potential of a QE on or in close proximity to the surface enabling unprecedented sensing capabilities. With the advent of wafer scale synthesis of single crystal h-BN films, there is a potential of

deterministic creation of a two-dimensional network of QEs that could be realized into practical quantum devices.

2.2. Experimental Observations

First reports of experimental observation of quantum emission from defects in h-BN in 2016 [137, 193, 196] propelled h-BN into the list of promising host materials for scalable quantum technologies. Since then experiments have been geared toward identifying the nature of defects giving rise to quantum emission. Toward that purpose, experimental tools and techniques have involved electron microscopy, optical spectroscopy, photon emission correlation spectroscopy, and more to understand the optical, charge and spin properties of QEs in h-BN crucial to coherent control for quantum technological applications.

A few reports have used electron microscopy such as transmission and scanning transmission electron microscopy (TEM and STEM) [8, 28, 47, 68, 88, 90, 143, 157, 207], scanning tunneling microscopy (STM) [215] and scanning electron microscopy (SEM) [38, 227] to understand the defects at atomic resolution. The inherent challenge in materials preparation for electron microscopy experiments as well as availability of necessary resources has resulted into limited reports. Further, the similar atomic numbers of boron and nitrogen atoms make it difficult to differentiate between the two atoms in an electron micrograph due to low Z -contrast. Nevertheless, a few heroic experiments have provided fruitful understanding of the defects not available from optical microscopy. Before the discovery of QEs in h-BN, TEM and STM studies reported first observation of defects in h-BN such as boron monovacancy (V_B) [8] and manipulation of native defects [215]. This set the stage for understanding the structural attributes of defects beyond the diffraction limit by using electron microscopy to correlate photoluminescence (PL) or optical images with TEM, STEM or SEM images of h-BN and various boron nitride allotropes [38, 47, 68, 207, 227] or correlating PL to cathodoluminescence (CL) [28, 88, 90, 177]. Majority of electron microscopy work has reported boron monovacancy or complexes as the defects.

Based on optical spectroscopy, the heterogeneous emission is categorized into UV/blue

(~ 3 to 4 eV), visible (~ 1.7 to 2.5 eV) and near-IR/IR ($\lesssim 1.6$ eV) emission. While majority of observations have been of visible QEs, there are a few reports of UV/blue and near-IR/IR QEs. The UV/blue QEs have primarily been observed in high quality h-BN crystals or powder [22, 28, 117, 156, 175, 177, 205, 206]. The majority of UV/blue QEs undergo quenched emission with increase in temperature - sharp ZPLs observed at cryogenic or liquid nitrogen temperatures turning into a quenched, broadband emission at room temperature. Reports of near-IR/IR QEs with sharp ZPL [34, 114, 210] are fewer than that of UV/blue QEs, primarily observed at cryogenic temperatures. Several other reports of near-IR/IR emitters are of the proposed negatively-charged boron vacancy, V_B^- consisting of a broadband emission centered at 1.5 eV [83, 130, 146, 191, 225]. These observations have so far been on V_B^- ensemble and a recent report identifies ZPL at 1.6 eV when coupled with a cavity [162]. Majority of observations of QEs in h-BN have reported visible emission typically consisting of a distinct but inhomogeneously broadened ZPL at room temperature [27, 40, 65, 66, 88, 131, 137, 184, 193, 196, 219, 227], irrespective of the h-BN source material - powder, nanoflakes, crystal, etc. A few of the visible QEs have also shown magnetic-field-dependent PL [66] and spin-resonance signal [184] at room and cryogenic temperature [39]. Visible QEs have been commonly classified into two classes based on its ZPL at ~ 1.8 eV and ~ 2.1 eV, with the spectral shift around the two ZPLs attributed to strain, charge dynamics, interaction with nearby defects, Stark shift, etc.

In a bid to identify the defect structures giving rise to quantum emission and understand its optical, charge and spin dynamics, research efforts have focused on understanding QEs' photodynamics, photostability, spectral diffusion, response to temperature, strain and stress, vibronic coupling, polarization properties and more. Commonly observed features include photon lifetime of a few nanoseconds and longer dark state lifetime of micro- to milliseconds [40, 65, 181], polarized excitation and emission [65, 103, 223], phonon-assisted transitions characterized by absorption and emission phonon side bands [11, 65, 104, 206], spectral diffusion [103, 115, 178] and blinking [26, 127, 185]. The study of photodynamics show high quantum efficiency [26, 151, 171], controllable switching between bright and dark

states [108], laser irradiated change in photostability [67] and plasmonic structure enhanced emission [62]. Photon emission statistics have shown complex behavior in nonlinear scaling of various rates as a function of excitation power [40, 115, 155, 181] which is now understood to be the result of indirect emission due to higher-lying excited states [104, 155]. The photostability has been shown to depend on excitation energy and ZPL [178], leading to photoinduced blinking for large mismatch, making excitation selectivity an important factor [115]. Spectral diffusion and blinking has been commonly reported, attributed to trapped-carrier-induced Stark shifts, surface interactions and sample morphology [6, 127, 178, 182, 185]. Photostability can be improved and spectral diffusion and blinking could be eliminated via suspension of h-BN to eliminate surface interactions [65, 66, 155], surface passivation [127], ionic liquid devices [142] or using a conductive substrate having high local carrier density at the QE [6, 152]. The spectral diffusion has led to electrical control of emission via Stark effect [152, 153, 170, 217].

A red shift of ZPL as well as its broadening has been reported for heterogeneous QEs as a function of temperature [6, 11, 103, 115, 181]. Reversible static [85, 141] and dynamic strain [98, 121] and pressure [221] response of ZPL has also been observed. Based on the PL response to the direction of strain, possible defect structures can be considered or eliminated based on symmetry considerations [85, 141, 221]. Understanding vibronic coupling has focused on the role of low-energy acoustic and high-energy optical phonons, typically using Huang-Rhys model. QEs in h-BN are found to have low Huang-Rhys factor - low number of phonons involved in transitions and thus more emission in ZPL compared to several other solid-state defects such as nitrogen vacancy in diamond. Empirical evidence based on vibronic coupling and optical dipole alignment suggests multiple excitation mechanisms of ZPL [104]. The ZPL broadening has been attributed to acoustic phonons and the phonon side bands to optical phonons [11, 65, 158, 206, 212], with longitudinal phonon mediated transition attributed to enhanced absorption [84, 107] and decoupling from in-plane phonon modes attributed to observed Fourier transform limited linewidths [55, 93]. Techniques such as two-photon pumping [109, 173] and single molecule localization microscopy to temporally

isolate multiple defects within a diffraction limited spot [68] and determine ensemble spectral properties [46] have also been employed to understand the photodynamics of QEs in h-BN.

Photophysical properties have been studied for different sample treatments, namely irradiation, ion implantation, etching and annealing – to understand defect creation, emission properties and photostability [129]. While annealing is used as a standalone treatment for activation of defects, it is also typically the last treatment step post irradiation, implantation and etching. Irradiation has been done using electron beam [30, 44, 60, 71, 194, 202], focused ion beam [228], high energy laser [44, 77, 95] and neutrons [192]; typically resulting in visible, heterogeneous and polarized emission with phonon-broadened but distinguishable ZPL. Focused ion beam and neutron-irradiation has been used for creating V_B^- ensemble having near-IR broadband emission. Controlled parameters in laser irradiation has also been used to create V_B^- ensemble [77]. Indentation using atomic force microscopy followed by annealing has been used to create a periodic array of QEs in h-BN [218]. Instead of creating defects by irradiation which is likely to create vacancy defects, ion implantation has been used to implant oxygen, boron, boron nitride and silicon [44], carbon [140] and cerium [132] ions that are likely to create substitutional defects having emission in the range of 2 eV to 2.25 eV. Chemical [40] and plasma [41, 118, 124, 148, 201, 202, 219] etching has been employed to study the effect of etching on the creation of QEs. Etching has resulted in QEs having heterogeneous emission in the visible range, unlike ion implantation that has resulted in narrow emission range. Etching has been shown to create defects in close proximity to the surface unlike e-beam irradiation that is likely to create emitters throughout the h-BN layers [202], also likely tuning the h-BN bandgap [148]. Annealing is widely used as a defect activation step, though the mechanism remains unknown. The commonly followed protocol involves annealing at 850 °C for 30 minutes usually in an inert atmosphere [30, 44, 61, 95, 159, 186, 194, 219], with other temperatures in the range of 750 to 1000 °C explored as well [41, 124, 133, 201]. The consensus is annealing at 850 °C in an inert atmosphere like Ar works best. However, the annealing times have not been optimized to improve photostability.

2.3. Proposed Defect Structures

Proposed defect structures of QEs in h-BN (Fig. 1) can be broadly categorized as native point defects and impurity based defects [209]. Native point defects are B or N vacancies (V_N , V_B), antisites (B_N , N_B), interstitials (B_i , N_i), complexes ($V_B V_N$, $N_B V_N$) and dangling bonds [1, 188, 190, 197, 209]. Impurity based defects are substitutional defects and complexes, most likely involving C, O or H (C_B , C_N , C_i , O_N , $V_B O_N$, $V_B H$). There are numerous possible defect structures in h-BN considering the native B and N based defects and impurity based defects from C, O or H which are present in all growth precursors. There are many other atomic species such as Si that are likely to find its way into h-BN crystal. Thus, hundreds of possible defect structures in h-BN can give rise to quantum emission. Further, B, N and C isotopes have implications on photophysical properties, primarily spin dynamics from the nuclear bath of different isotopes. However, using density functional theory, group theory and thermodynamic considerations, several defect candidates can be eliminated based on formation energy, migration energy and thermal stability, especially in comparison with experimental treatment conditions such as high temperature annealing. Comparing calculations of charge-state transitions, luminescence lineshapes and spin properties with experimental observations, several defect structure candidates can be ruled out. Studies have found large differences in calculated electronic spectra of defect structures but less so in vibronic spectra [116], which explains the experimental observation of similar vibronic coupling in heterogeneous defects. Theoretical work suggests that vacancies and their complexes, along with substitutional carbon atoms and dangling bonds, are likely candidates, although consensus is still lacking [52, 116, 167, 190, 197, 209]. Specific candidates include $V_N N_B$, $V_N C_B$, $V_B C_N$, $C_B C_N$ and the boron dangling bond (Fig. 1).

2.3.1. Theoretical Proposals

Early defect proposals almost 50 years ago considered substitutional and vacancy defects, C_N and V_N , having UV and IR emission, respectively [230]. Vacancy and divacancy were considered based on migration of B and N atoms, and proposed the energetically favorable formation of $V_B \sim 600$ °C whereas unfavorable formation of V_N [229]. Similar conclusion has

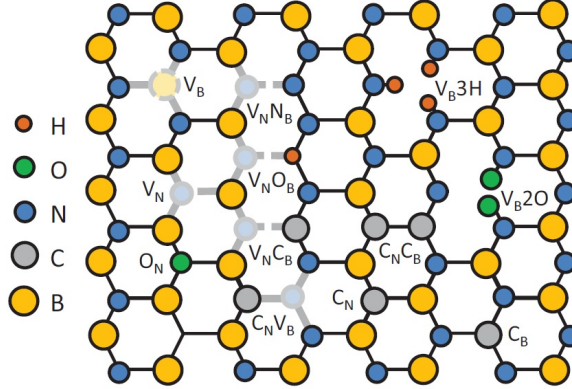


Figure 1: Geometry of Various Proposed Defects in Hexagonal Boron Nitride. Reprinted from Zhang *et al.*, Appl. Phys. Rev. 7, 031308 (2020); with the permission of AIP Publishing [226]).

been reached by other reports [209]. Since experimental observations of quantum emission, attention has been on likely defect structures based on sample treatment methods such as irradiation and annealing. These treatments are likely to create vacancies and complexes which has brought focus on defect candidates such as V_B , V_N , $V_N N_B$, $V_N C_B$, $V_B C_N$ and $C_B C_N$. Theoretical calculations have taken into consideration the optical, charge and spin properties to screen the defect candidates for their suitability to quantum technological applications [165, 167, 190, 216]. A few reports have focused on $V_N C_B$ and $V_B C_N$ [1, 42, 167, 169, 190, 216], with the latter proposed to have ground state spin polarization due to a triplet ground state. However, the calculated ZPL of $V_N C_B$ has a wide range from 1.33 to 1.95 eV because of the limitations and challenges of calculations using density functional theory, making large errors possible [165]. This makes one-to-one comparison with experimental observations contentious. Recent calculations have shown that $V_B C_N$ is dynamically unstable and reconfigures into $V_N C_B$ [7]. Both $V_N N_B$ and V_B^- are proposed to have ZPL ~ 2 eV and optical spin polarization [1, 75, 168]. Recent calculations have focused on the experimentally proposed V_B^- defect, estimated to have ZPL of 1.62 eV [83, 99, 128, 166]. Substitutional carbon defects - C_B and C_N are proposed to be paramagnetic and have ZPL in the visible range [7, 15, 134]. Recent proposals of carbon trimer, $C_2 C_N$ and $C_2 C_B$ have been proposed to have ZPL ~ 2 eV, and vibronic coupling and photoluminescence

lifetime comparable to experimental observations [100, 125, 134]. The boron dangling bond is proposed to have ZPL ~ 2 eV and Huang-Rhys factor of 2.3, with indirect emission through the conduction band for large excitation energies [197, 199, 200]. This defect agrees with the proposals and observations of indirect excitation [104, 155] as well as explains the ZPL heterogeneity based on out-of-plane distortions.

Properties of defects incorporating Si, Al, Ga, Sb, P, Ti and Mo have been calculated [23, 164, 180], though are unlikely to be present unless h-BN is intentionally doped with them. Several proposals have considered defect clusters, triangular and hexagonal defects - considering the stability of B, N and O termination [97, 157]. Several reports have addressed UV/blue emission - attributed to V_N [14] bound to C or O atom, $C_N O_N$ [205], Stone-Wales defects [87], C_B [139] and carbon dimer $C_B C_N$ [15, 116, 128, 134, 135, 213]. So far, carbon dimer has been consistently proposed to have ZPL ~ 4 eV and thus a likely defect giving rise to UV emission.

2.3.2. Experimental Proposals

Experimental proposals of defects giving rise to quantum emission in h-BN have focused on direct observation of defects using electron microscopy and comparison of experimental observations and theoretical proposals. Using TEM, boron vacancy, triangular and hexagonal defects have been commonly observed [8, 157]. The cathodoluminescence from electron microscopy having emission ~ 4 eV has been attributed to carbon based defects such as C_N and other carbon substitutional defects [28, 90]. The UV emission in carbon doped h-BN lends support to carbon dimer as probably defect structure giving rise to UV emission [156]. Silicon based substitutional defects have been observed in STEM studies [144].

Based on experimentally observed ZPL, $V_N N_B$ [85, 88, 90, 95, 153, 193, 223], $V_N C_B$ [70, 88, 90, 133, 153, 223] and V_B^- [69, 83] have been proposed as the likely defect candidates. Several reports of ZPL in the range of 1.7 to 2.2 eV, centered at 2 eV have proposed $V_N N_B$ as the underlying defect structure [90, 95, 193, 223], with the ZPL energy shift attributed to strain [85] and Stark shift [153]. The carbon based defect $V_N C_B$ has been proposed

to be the defect structure giving rise to ~ 2.15 eV emission [69, 88, 90, 133, 223]. Several reports of emission from h-BN annealed in carbon rich environment or implanted with carbon have proposed $V_N C_B$ in the neutral and negative charge states [133, 140]. However, one report with observed ZPL ~ 2.14 eV found mismatch between experimental and theoretical vibronic coupling for $V_N N_B$ and $V_N C_B$ [84]. In order to identify a theoretical proposal to be underlying defect for experimental observations, rigorous comparison should consider all photophysical properties.

Other proposals have considered nitrogen vacancy based defects for 3.26 eV [22], vacancy complexes in irradiated samples for ~ 2.1 eV from edges [44], V_i ($i = B, N$ and BN) for 1.3 eV to 2.5 eV [127] and $V_N O_B$ for ~ 2 eV emission [88, 153]. The nitrogen vacancy based defects such as V_N with interstitials such as B_i , C_i and O_i have been proposed [88] whereas $V_N X_B$ for $X = O, N$ and C has been proposed based on the PL response to the direction of strain such that the possible defect structures can be considered or eliminated based on symmetry considerations [85, 141, 207, 221]. The negatively charged vacancy defects such as $V_N N_B^-$ for ~ 1.2 eV [34], and V_B^- for ~ 2 eV [69] and ~ 1.55 eV [83] emission have been proposed. The ZPL for V_B^- has been reported to be 1.6 eV by cavity enhanced emission [162]. A lack of evidence for pure single-photon emission motivated a proposal that h-BN's QEs occur in pairs as "double defects" [27], which has been refuted by the recent observation of pure single-photon emission likely from boron dangling bond [155]. Recent observation at low temperature of ~ 1.65 eV ZPL showing ODMR with low zero-field splitting (ZFS) has been attributed to substitutional defect. Substitutional defect based on cerium, CeV_B is proposed to give rise to ~ 2 eV emission in cerium implanted h-BN [132]. Recent report has proposed donor-acceptor pairs giving rise to 1.4 to 2.4 eV emission [189].

2.4. Spin-Based Quantum Emitters

Since the first observation of magnetic-field-dependent PL [66], spin-dependent fluorescence has been confirmed at cryogenic as well as room temperature [39, 83, 184]. The observed spin-based QEs can be categorized as spin ensemble having IR emission [83] and single spins having visible emission [39, 184]. The spin ensemble has been proposed as the negatively

charged boron vacancy V_B^- having broadband PL emission centered at 1.5 eV, short excited-state PL lifetime of 1.2 ns and ZFS of ~ 3.48 GHz with negative polarity arising from the triplet ground state ($S = 1$). The ZPL has been reported to be 1.6 eV by cavity enhanced emission [162]. The ZFS spectra obtained by ODMR consists of two resonances separated by ~ 100 MHz with central resonance of ~ 3.48 GHz. The two resonances are assigned to ± 1 spin transitions. The V_B^- ensemble is created by neutron and electron irradiation [83, 147], ion implantation [74, 83, 86, 110] and femtosecond laser writing [77]. These techniques knock-out boron atoms in an uncontrolled manner and thus individual defect having single-photon emission is yet to be observed. Ion implantation has been done using He, Ar, Xe, H, C, N, Li, Ga [74, 83, 86, 110] – deep implantation depth for lighter elements resulting in more vacancies being created and thus higher PL intensity. Consistent spin resonance frequency in samples that have undergone different treatments is advantageous for device integration and low barrier to sample preparation. Interestingly, all reports on V_B^- have utilized tape exfoliated h-BN flakes from high quality h-BN crystals (typically purchased from HQ Graphene, Netherlands). The V_B^- coupled to metasurfaces [74] and plasmonic waveguides [76] enable integrated photonic devices. Such a coupling would be necessary to improve the otherwise low ODMR and spin contrast [76], achieve narrower ZPL emission and improved signal-to-noise ratio and coherence properties [74]. To probe the true ZPL of V_B^- , cavity quantum electrodynamics (QED) was used by coupling micro ensembles to the cavity mode of a proximal silicon nitride nanobeam cavity [162]. Room temperature coherent control of V_B^- ensemble has spin-relaxation times $T_1 \approx 18 \mu\text{s}$, $T_2 \approx 2 \mu\text{s}$ and $T_2^* \approx 100 \text{ ns}$ [82]. The limited electron spin coherence time, T_2^* due to nuclear spin environment [130] has been demonstrated to go up to 800 ns in a protected qubit basis achieved by continuous concatenated driving which uses strong continuous microwave drive to extend the Rabi oscillation damping time [163]. Recent reports of excited state spectroscopy measured the excited state ZFS to be ~ 2.1 GHz, observed ground and excited state level anticrossings and found similar ground and excited state g_e -factor ~ 2 [18, 138, 146, 225]. Further, coherent coupling of V_B^- electron spin with three nearest nitrogen nuclear spins has been demonstrated

at room temperature [78, 147]. It is important to understand the nuclear spin bath due to non-zero nuclear spin of ^{14}N , ^{10}B and ^{11}B isotopes present in h-BN. Nuclear spins have longer coherence times compared to electron spins, making optical polarization and coherent control of nuclear spins useful for applications such as quantum memories and network. This demonstrates the potential of spin defects in h-BN for quantum memories and network.

The discovery of V_{B}^- ensemble led to rapid progress in understanding its spin properties. However, its optical dynamics are not yet understood and thus its various photophysical properties remain unknown. Photon emission statistics could highlight the ensemble density from the antibunching dip as well as metastable states and its associated nonradiative rates, providing information about possible charge states. Understanding the optical dynamics is crucial to improving optical coherent control. Further, V_{B}^- ensemble is typically excited with 532 nm. Photoluminescence excitation spectroscopy would shed light on efficient absorption processes that might possibly happen at other excitation wavelengths and the optical dynamics at resonant excitation which might help improve spin contrast and coherence times. While an individual V_{B}^- has not been observed, spin-resonance of visible QEs having $g^{(2)}(0) \lesssim 0.5$ has been observed at cryogenic [39] and room temperature [184], discussed in detail in Section 3.3.

2.5. Applications

H-BN has multifaceted applications ranging from monolayer dielectric for two-dimensional transistors to host of QEs for quantum technologies [19]. Many of the quantum effects in h-BN can be observed at room temperature, making it promising material for room-temperature quantum technologies and integrated photonics. The low dimensionality opens up avenues of device integration and heterostructures, giving rise to properties otherwise not accessible in any one material.

2.5.1. Integrated Photonics

Owing to the availability of high quality h-BN and established fabrication techniques, various optomechanical and photonic applications can be realized from h-BN [33]. The refractive index, n of h-BN is ~ 1.8 in the visible range. This low n enables light to easily escape from

the h-BN structure. This would be a major drawback in using h-BN for photonic structures aimed at confining light within the h-BN structure. However, the index of refraction in h-BN is different in each direction owing to its anisotropy. Further, the permittivity ϵ ($\epsilon \sim n^2$) is opposite along orthogonal directions which make h-BN a natural hyperbolic material. The hyperbolic properties of h-BN support phonon polaritons which arise from coupling of infrared (IR) photons and optical phonons in h-BN's polar lattice [33, 48]. This enables use of h-BN for IR nanophotonics, sub-diffraction imaging and applications requiring negative refraction. The propagation of phonon polaritons enables strong light-matter interactions such as in cavity optomechanics [176]. Subwavelength diffractive optical elements such as metasurfaces can be realized from h-BN at the visible and near-infrared wavelengths using its high refractive index to couple to QEs [74]. Metasurfaces made from h-BN have a distinct advantage of integration with other two-dimensional and bulk materials, and flexible substrates. Such metasurfaces can be produced at scale using large-area single-crystal films and easily transferred on to the other surfaces. Photonic structures such as photonic crystal cavities [112], microcavity [161], tunable cavities, waveguides and grating couplers [73, 122] fabricated from h-BN have potential for integrated quantum photonic circuits and cavity QED experiments [208].

2.5.2. Coupling, Controlling and Tuning Quantum Emitters

As a host of QEs and a photonic material, h-BN is naturally suited as a platform for coupling QEs to photonic structures [35, 63]. Coupling QEs can enable on-chip integration of van der Waals materials, cavity QED or tunability of emission properties such as spectral linewidth or single-photon purity. Early efforts have focused on activation of QEs in h-BN via strain engineering and external electrostatic potentials [160] and creation of QEs in h-BN photonic crystal cavities [112]. The opposite approach of fabricating photonic structures from h-BN with pre-characterized QEs have also been explored [73]. In such devices, six-fold enhancement in PL has been demonstrated at room temperature, motivating the use of photonics to improve QE properties. Other demonstrations of coupling QEs to photonic structures include coupling to waveguides [111] and using micro-cavities [202] to

improve single-photon purity and for Purcell enhancement. Fiber coupling of h-BN QEs has been explored for room-temperature single-photon sources [172, 204]. Plasmonic coupling of QEs in h-BN has shown Purcell enhancement in the weak coupling regime using device architectures involving nanoparticle [195] and nanopillar [160], waveguides [102] and resonant nanoantenna [154]. However, the plasmonic enhancement achievable is weak due to the high brightness and high quantum efficiency of h-BN QEs in its pristine form. Further, the high refractive index of h-BN shields the QE from the plasmonic field which would necessitate very specific device geometries and material thickness to achieve purposeful enhancement. Using metallo-dielectric antennas, near-unity light collection efficiency has been achieved in h-BN QEs at room temperature [126]. The metallo-dielectric antennas support arbitrary dipole orientations unlike plasmonic devices which require rotational control of the in-plane dipole as well as spatial and spectral matching. Many different forms of energy: light, electricity, magnetism and sound could be used to control, tune or modulate h-BN QEs owing to h-BN's optical, electronic and mechanical properties. As a dielectric material, an electric field can be created through h-BN which enables Stark tuning of QEs embedded in h-BN [152, 153]. This allows for the control and tuning of a QE's properties such as its spectral diffusion. Strain engineering of h-BN film opens another avenue to tune QE properties [140]. Surface acoustic waves have also been investigated to control and tune emission of h-BN QEs via dynamic strain fields [98]. Van der Waals heterostructures comprising of h-BN, graphene and transition metal dichalcogenides offer distinctive material platform and device characteristics unique to these systems. While h-BN in heterostructures has been commonly employed as a dielectric and insulating encapsulation, it takes on a different role as a host of QEs. Excitons in transition metal dichalcogenides and QEs in h-BN have been shown to interact via resonant energy transfer [123], opening up avenues to study such interactions for applications such as sensing and light harvesting. Graphene/h-BN heterostructures can be used to tune emission properties of QEs in h-BN via the Stark effect [153, 170] by using graphene gates. Graphene could also be used to control charge and energy transfer of h-BN QEs [220]. Heterostructures and two-dimensional integration opens up possibilities such as

electrical control of QEs in h-BN, spin-to-charge conversion and energy harvesting.

2.5.3. Quantum Sensing, Imaging, Communication and Memories

The QEs in h-BN have immense potential for quantum technologies owing to its attributes such as high purity single-photon emission at room temperature, narrow linewidth, high brightness and high quantum efficiency. As a van der Waals material, h-BN surface does not have dangling bonds and monolayer can host QEs. Other QE hosts such as diamond typically suffer from surface impurities and dangling bonds which adversely affect QEs located close to the surface. Thus, QEs in h-BN are amongst the best candidates as quantum sensors of temperature, electromagnetic fields and pressure [81], or biological and chemical compounds. The QEs in h-BN have been implemented as nanoscale optical thermometers [43]. These sensors have been shown to operate in large temperature ranges from 0 K to 800 K, offer high signal-to-noise ratio owing to high brightness, are accurate due to h-BN's high thermal conductivity and can be easily integrated with other materials. Due to the Stark effect, QEs in h-BN can also serve as quantum sensors of the electric field [152]. Magnetic-field-dependence of QEs [66] and spin-dependent-fluorescence in QE ensemble [83, 110] make h-BN QEs promising candidates for magnetic field sensing. However, further developments in this direction are needed to conclusively establish the nature of the defect which could give rise to spin-dependent-fluorescence in a single QE. The conclusive identification of spin based single-photon emission in h-BN QEs would open up the possibility of using h-BN QEs for quantum computation. The QEs in monolayer h-BN have been used in super-resolution microscopy [46, 68] for imaging beyond the diffraction limit, heralding the use of h-BN QEs for quantum imaging. Using single molecule localization microscopy, h-BN QEs spatially separated by 10 nm are imaged using temporal isolation enabled by the QEs' blinking. A variety of applications including quantum communication require QEs having natural or Fourier transform limited linewidth, spectral stability and high purity single-photon emission. Fourier transform limited linewidth of QEs in h-BN [54, 55] combined with the control over spectral diffusion by electric fields and high purity single-photon emission [155] make QEs in h-BN promising for room-temperature quantum communication. Applications such

as quantum random number generator [211] and quantum key distribution [203] using QEs in h-BN is actively in research. Using V_B^- electron spins to optically polarize and coherently couple to nuclear spins which have longer coherence times enable spin-based QEs in h-BN for quantum memories and network [78, 147].

CHAPTER 3 : Current Understanding of Visible Quantum Emitters

Plethora of defects have shown visible quantum emission in h-BN. However, the outstanding question is identification and creation of visible QEs in h-BN. The QEs' electronic and chemical structure remains unknown. While theoretical predictions exist [165, 167, 209], conclusive experimental evidence of visible QEs' structure remain elusive. This chapter discusses the current understanding of visible QEs in h-BN and is organized as follows: Section 3.1 discusses the electronic level structure and vibronic and polarization properties; Section 3.2 discusses the optical dynamics; and Section 3.3 discusses the spin dynamics.

3.1. Electronic Level Structure, Vibronic and Polarization Properties

A three-level model consisting of an electronic ground state, an excited state and a metastable state is the simplest model that accounts for both the radiative transition involving photon emission and nonradiative transitions through a metastable state. The commonly proposed electronic level structure of visible QEs in h-BN is a three-level model based on photon correlations [137, 193]. However, multiple metastable states tend to exist due to charge and spin manifolds or nearby/extended defects reflected in complex optical dynamics [103, 155, 181, 196]. While the presumed transition mechanism is a direct excitation and emission between ground and excited states, careful analysis of optical dynamics has shown indirect excitation and emission involving different excited and radiative states [155]. The photoluminescence lineshapes show phonon-assisted absorption and emission - phonon sidebands (PSBs) within 200 meV of the ZPL involving acoustic and optical phonons [104, 137, 212]. The high energy optical phonons are typically ~ 150 meV energy whereas the low energy acoustic phonons tend to be unresolved. Using Frank-Condon principle and Huang-Rhys model, the vibronic coupling of visible QEs in h-BN is well quantified [65]. On an average, photon emission is estimated by Huang-Rhys factor to involve ~ 2 phonons [65, 155, 196]. Polarized absorption and emission has been observed in visible QEs, though having varied dipole mismatch indicating single or multiple absorption and emission dipole governed optical transitions [65, 90, 223].

3.2. Optical Dynamics

Interpreting the optical dynamics is key to understanding the electronic level structure. The internal dynamics of the electronic level structure arising from the radiative and nonradiative transitions are determined by the various levels involving metastable states. These dynamics can be probed using photon emission correlation spectroscopy (PECS) [70] - a powerful technique to understand the various transitions that give rise to the optical dynamics (see Sec. 4.5 for a detailed discussion). In the process, an electronic level structure can be built that is consistent with the observations. Combined with theoretical calculations, group theory and symmetry considerations, plausible defect structures could be proposed.

Photon correlations give rise to two features characteristic of the optical dynamics – antibunching and bunching in the second-order photon autocorrelation function (see Sec. 4.5). While only one antibunching feature is observed corresponding to quantum emission, several bunching features spanning timescales several orders of magnitude are commonly observed due to presence of dark or metastable states. The photon relaxation rate or antibunching rate corresponds to the time taken by the system to relax back to the ground state associated with the emission of a photon. For QEs in h-BN, this typically corresponds to a few nanoseconds [65, 66, 155, 181, 194]. The photon bunching rates are dependent on the internal nonradiative rates, the corresponding timescales in the range of hundreds of nanoseconds to several milliseconds [38, 65, 181]. The antibunching and bunching rates are sensitive to external stimuli such as excitation power [155], magnetic field [66] and wavelength [108, 210] due to charge and spin manifolds. The excitation power-dependent scaling of the rates [26, 38, 181] provide a picture of the excitation and emission mechanisms involved [155] – much complex than the commonly posited simple three-level electronic structure [193]. The proposal of double defects giving rise to quantum emission in h-BN relied on two independent electronic transitions each modeled using three-levels. The magnetic-field-dependent photon correlations have shown a change in optical dynamics of QEs in h-BN – a signature of presence of spin [66]. Excitation with detuned lasers has been used to modify the optical dynamics, possibly by altering the charge dynamics of the QEs [108, 210]. Resonantly driven

QEs in h-BN have shown Rabi oscillations in photon correlations [114].

The features arising from photon correlations set a lower limit on the number of levels in the electronic level structure and hence the interpretation of the levels present. This necessitates a careful analysis and capture of features that span timescales that vary over six orders of magnitude, using robust fitting routines and procedures to quantify the quality of the statistical models used to describe the data. While a few reports have calculated photon correlations to understand the underlying levels in the structure [26, 27, 38, 181], the analysis has lacked the rigor necessary for an accurate understanding of the electronic level structure. As a result, the origin of complex optical dynamics of QEs in h-BN has not been addressed. In this thesis (Chapter 5), we present a study of the optical dynamics of QEs in h-BN and use it to understand the electronic level structure of the underlying defect. We uncover the origin of excitation and emission mechanism of the QEs previously unknown and explain several past observations of complex optical dynamics. We present pure SPEs characterized by noise-limited $g^{(2)}(0) = 0$. To the best of our knowledge, this is a first observation of pure SPEs in h-BN.

3.3. Spin Dynamics

While rapid progress has been made in the understanding of V_B^- ensemble having IR emission since it was first proposed in 2020 [83], single spin remain elusive. A single-spin defect is an optical defect that is a SPE and has spin that can be confirmed using ODMR. Thus, a pure single spin is a spin-based QE that has a pure single-photon emission characterized by zero-delay second-order photon autocorrelation function, $g^{(2)}(0) = 0$. Quantized photon emission results in $g^{(2)}(0) < 1$ (see Section 5.3), for instance in the case of multiple emitters. A pure SPE is strictly characterized by $g^{(2)}(0) = 0$ within experimental uncertainty [70]. Spin-based QEs in h-BN have been reported at cryogenic (5 K) [39] and room temperature [184] having $g^{(2)}(0)$ as 0.22 and 0.34, respectively. Thus, a pure single spin is yet to be reported. Nevertheless, the recent spin results are important – they show spin resonance for 1.6 eV to 1.75 eV [39] and ~ 2.1 eV [184] ZPL emission. Strikingly, these QEs have similar spin properties – a weak ZFS ~ 10 MHz and g -factor ~ 2 , close to free electron g_e -

factor of 2.0023. They show both negative and positive polarity in continuous-wave ODMR contrast that goes up to 20% at cryogenic [39] and 6% at room temperature, though typically below 2% [184]. The spin resonance observed at cryogenic temperature was not observed at room temperature. As a function of an applied magnetic field, the resonance frequency varied linearly without any splitting observed. The resonance linewidths (full width at half maximum) were measured to be ~ 35 MHz, both at cryogenic and room temperature – indicating no role of temperature in the broadening. The room temperature observations show an additional bunching timescale in the photon correlations of QEs with spin, indicating different photodynamics for paramagnetic vs nonmagnetic QEs [184]. From the measured QEs, only a fraction ($\sim 5\%$) showed paramagnetic behavior [184], as observed previously for QEs having magnetic-field-dependent photoluminescence [66]. The proposed electronic level structure consisted of Zeeman-split ground (g_1, g_2), excited (e_1, e_2) and a metastable (m_1, m_2) state doublet, though suggested to be incomplete [39].

Much remains unknown regarding the single spins – the nature of underlying defect(s), spin states, spin dynamics and its coherence properties. The biggest puzzle is the origin of a low ZFS; such a low energy splitting is not expected to arise from electron spin-spin interaction. In this thesis (Chapter 6), we present a pure single spin at room temperature characterized by noise-limited $g^{(2)}(0) = 0$, having spin resonance frequency of 1316 MHz for an in-plane applied magnetic field of 470 G, g -factor ~ 2 and no ZFS, attributed to a doublet ($S = \frac{1}{2}$) spin state. To the best of our knowledge, this is a first observation of a pure single-photon emitter with spin in h-BN. We discuss the optical, time-domain and spin dynamics of single spin using optical and microwave pulse protocols crucial to developing methods to coherently control the QE’s spin.

CHAPTER 4 : Materials and Experimental Methods

The device preparation and developing robust experimental methods have been at the core of this thesis, enabling scaling and automation of data acquisition and analysis. This chapter details the materials and experimental methods and is organized as follows: Section 4.1 discusses materials, device fabrication and sample treatment; Section 4.2 discusses the experimental setup for probing optical and spin dynamics; Section 4.3 details the microwave chip for spin dynamics measurements; Section 4.4 discusses the photoluminescence characterization of the QEs; Section 4.5 discusses the methods and analysis for probing optical dynamics; and Section 4.6 discusses the electronic level structure simulations.

Parts of this chapter have been adapted with permission from Patel et al., 2022 [155]¹. The experimental methods of this chapter were completed in a close collaboration with Dr. David A. Hopper and Dr. Tzu-Yung Huang. This work was primarily supported by the National Science Foundation (NSF) award DMR-1922278 and partially supported by the use of facilities and instrumentation in the Singh Center for Nanotechnology at the University of Pennsylvania, supported by NSF through the National Nanotechnology Coordinated Infrastructure (NNCI; Grant ECCS-1542153) and the University of Pennsylvania Materials Research Science and Engineering Center (MRSEC; DMR-1720530).

4.1. Sample Preparation

Two wafer-scale substrate fabrication recipes were developed at the Singh Center for Nanotechnology. The first is referred to as non-microwave substrates which consisted of fabrication of circular trenches. The second is referred to as microwave substrates which consisted of fabrication of circular trenches and on-chip antenna for microwave transmission. Both recipes used starting wafer consisting of 90 nm thermal oxide on silicon, sourced from Rogue Valley Microdevices resulting in ~ 40 substrates on each wafer post fabrication. The top panel of Fig. 3 shows a scanning electron microscope image of a region of non-microwave (left) and microwave substrate (right). Each substrate consists of 50×50 such coordinates

¹This manuscript was accepted to appear at PRX Quantum at the time of writing of this thesis.

used to locate exfoliated h-BN flakes. The non-microwave substrate fabrication process consisted of spin coating a resist layer (SURPASS 4000 at 3000 RPM for 60 s, 15 s IPA rinse, SPR220-3 at 3000 RPM for 60 s) followed by soft bake (115 °C for 90 s), resulting in 2512 nm thick resist (measured using Filmetrics F50). Next, photolithography (using SUSS MicroTec MA-6 Mask Aligner) exposes the resist layer to UV light passing through a custom photomask. Upon waiting for 15 minutes, a post exposure bake (115 °C for 60 s) is performed followed by a 15 minute wait before developing the resist (two 60 s baths in MF-26A). Next, reactive ion etch (using Oxford Instruments Plasma Lab 80+ RIE) is performed to etch the oxide layer (using CF_4) with the etch recipe optimized to ensure a complete and an anisotropic etch of the 90 nm oxide resulting in circular trenches. Next, a deep reaction ion etch (using SPTS Rapier Si DRIE) is performed to etch a few μm of Si with the etch recipe optimized for an anisotropic etch. Post etching, the resist is liftoff (Acetone bath for 5 minutes) followed by a soft O_2 plasma clean (using Anatech SCE 108 Barrel Asher) to clean off any polymer residues. In the final step, a thick resist layer (S1818 at 500 RPM for 60 s followed by a bake) is spin coated and the wafer diced (using ADT 7100 Dicing Saw) into individual substrates.

The microwave substrate fabrication process is depicted in Fig. 2. The primary goal of developing and fabricating microwave substrates was to enable microwave transmission for generating on-chip AC magnetic field for spin control measurements. The fabrication process consisted of spin coating a resist layer (SURPASS 4000 at 500 RPM for 5 s followed by 3000 RPM for 45 s, 15 s IPA rinse, SPR220-3 at 3000 RPM for 60 s) followed by soft bake (115 °C for 90 s), resulting in 2512 nm thick resist (measured using Filmetrics F50). Next, photolithography (using SUSS MicroTec MA-6 Mask Aligner) exposes the resist layer to UV light passing through a custom photomask. Upon waiting for 15 minutes, a post exposure bake (115 °C for 60 s) is performed followed by a 15 minute wait before developing the resist (90 s bath in MF-26A). Next, reactive ion etch (using Oxford Instruments Plasma Lab 80+ RIE) is performed to etch the oxide layer (using CF_4) with the etch recipe optimized to ensure a complete and an anisotropic etch of the 90 nm oxide resulting in trenches. Next,

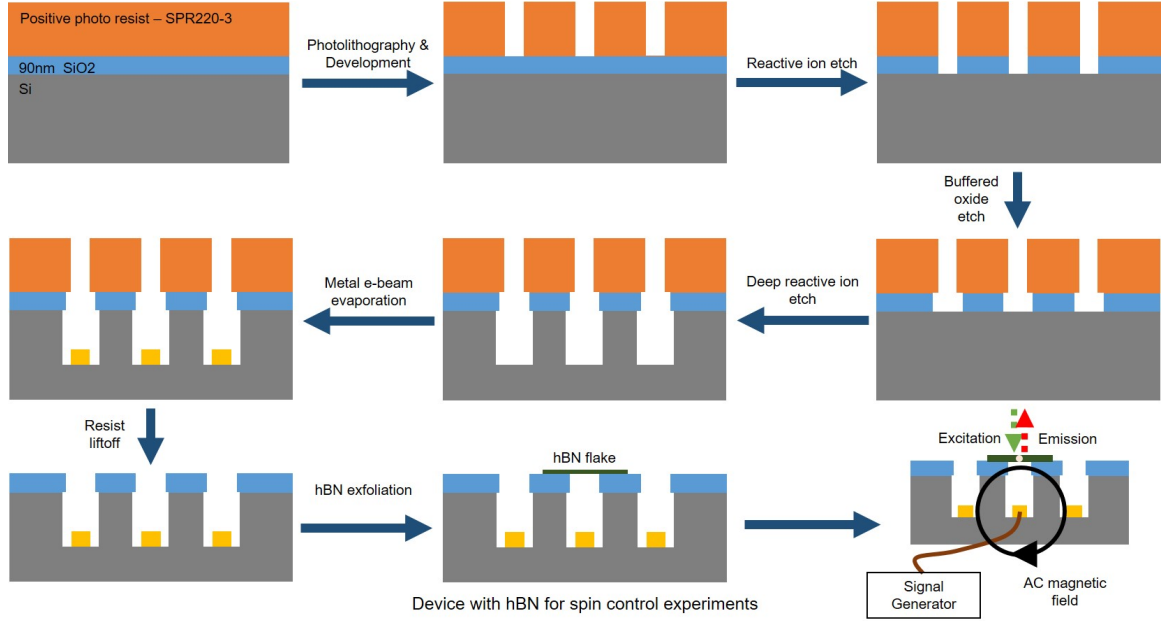


Figure 2: Fabrication Recipe for Microwave Substrates.

the wafer is cleaned with DI water followed by nitrogen blow dry. A buffered oxide etch (60 s bath in hydrofluoric acid diluted by 19 volumes of DI water) is performed to slightly undercut the oxide below the resist layer followed by DI water cleaning and nitrogen blow dry. Next, the Bosch process or a deep reaction ion etch (using SPTS Rapier Si DRIE) is performed to etch 10 μm of Si with the etch recipe optimized for an anisotropic etch. Next, the wafer is cleaned with DI water followed by nitrogen blow dry. In the etched trenches, metal is deposited (25 nm Ti/75 nm Au using Kurt J. Lesker PVD 75 PRO-Line E-Beam Evaporator) to be used for microwave transmission. Post etching, the resist is liftoff (Acetone sonication bath for 10 minutes) followed by a soft O_2 plasma clean (using Anatech SCE 108 Barrel Asher) to clean off any polymer residues. In the final step, a thick resist layer (S1818 at 500 RPM for 60 s followed by a bake) is spin coated and the wafer diced (using ADT 7100 Dicing Saw) into individual substrates.

The h-BN samples consisted of bulk, undoped, single crystals purchased from HQ Graphene. The bulk crystals were mechanically exfoliated using a dry transfer process [96] resulting in thin (≤ 100 nm) and large area (~ 50 μm) flakes of h-BN. Prior to h-BN

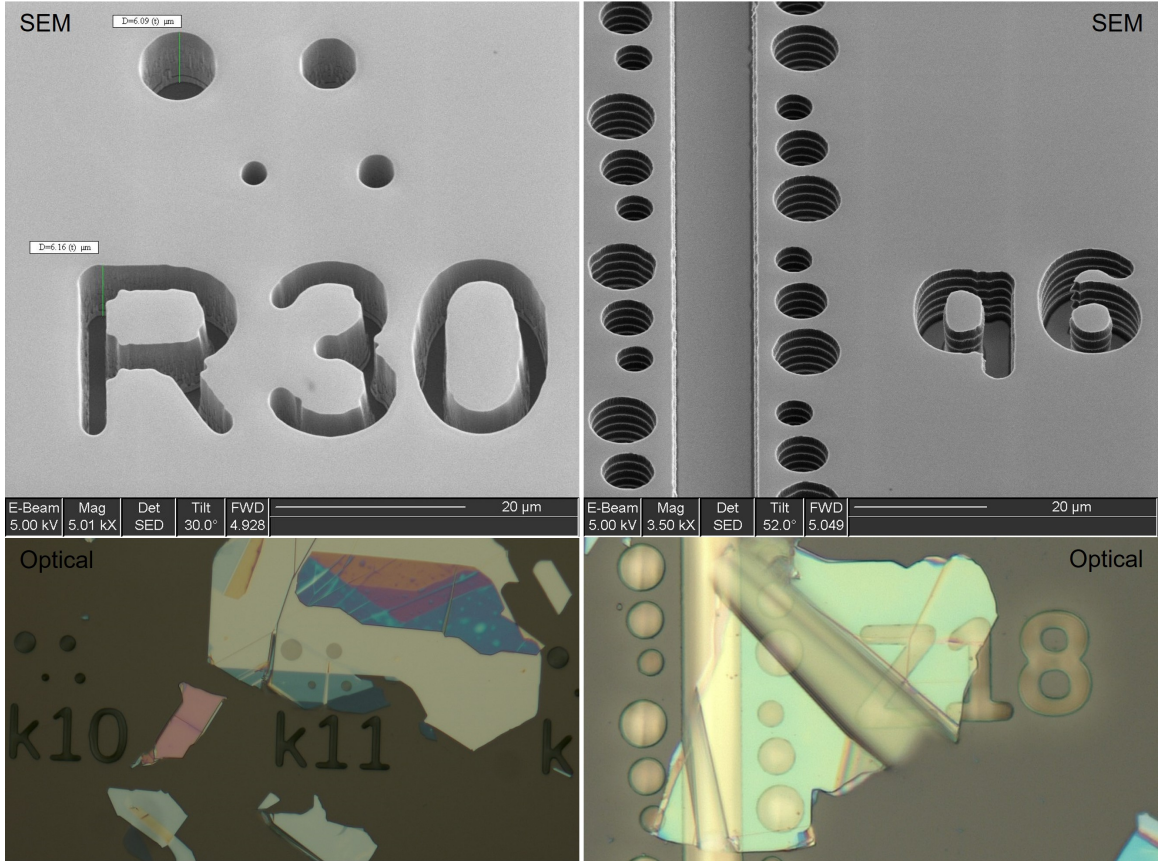


Figure 3: Scanning Electron Microscope and Optical Images. (Top) Scanning electron microscope images of non-microwave (left) and microwave (right) substrates. (Bottom) Optical images of substrates post h-BN exfoliation.

exfoliation, the protective resist layer on the substrate is cleaned off with Acetone followed by a soft O_2 plasma. The exfoliated flakes were transferred on to SiO_2/Si substrate with micro-fabricated circular trenches $4\mu m$ to $8\mu m$ in diameter and $5\mu m$ deep. Prior to the optical studies, the exfoliated h-BN samples were cleaned with a soft O_2 plasma (Anatech SCE 106 Barrel Asher, 50 W of power, 50 sccm O_2 flow rate) for 5 minutes to remove polymer residues resulting from the transfer process. The samples were then annealed in a tube furnace at $850^\circ C$ in low flow Ar atmosphere between 30 minutes to 2 hours. Annealing h-BN has been found to brighten the emitters [30]. Annealing for longer time (2 hours vs commonly used 30 minutes) significantly improves emitter stability. Figure 3 shows optical images of exfoliated h-BN flakes on the substrates.

4.2. Experimental Setup

Figure 4 depicts a simplified schematic of the room-temperature confocal microscope used to measure the emitters. There are two available excitation sources: a 532 nm (green) cw laser (Coherent, Compass 315M-150) and a 592 nm (orange) cw laser (MPB Communications, VF-P-200-592). The power and polarization of each excitation path can be independently selected. Excitation power values are measured just prior to the objective. In addition, a shutter completely blanks the excitation source when imaging is not in use to mitigate unnecessary light exposure. The excitation paths are combined with the collection path using a long pass (LP) dichroic mirror (Semrock, BrightLine FF560-FDi01 for green and Semrock, BrightLine FF640-FDi01 for orange). The LP dichroic cut-off is 560 nm for green excitation and 640 nm for orange excitation. A fixed half-wave plate in each of the excitation paths corrects for the birefringence induced by the dichroic mirrors. The co-aligned excitation and collection paths are sent through a $4f$ lens system with a fast steering mirror (Optics in Motion, OIM101) and a 0.9 NA 100x objective (Olympus, MPI Plan Fluor) at the image planes. This allows for the collection of wide-field, rastered, micro-photoluminescence (μ -PL) images. The objective is mounted on a stage system for changing the field of view. Pictures of the actual setup are shown in Appendix A.

The collection path consists of a linear polarizer (Thorlabs, WP25M-VIS) for measuring the emission polarization as well as a wide-band variable retarder (Meadowlark, LRC-100) which compensates for the birefringence induced by the dichroic. A LP filter specific to the excitation color fully extinguishes any scattered excitation light and the Raman signal. The cut-on wavelengths are 578 nm (Semrock, BLP01-568R-25) and 650 nm (Semrock, BLP01-635R-25) for green and orange, respectively. The filtered light is focused onto the core of a 50 μ m core multi-mode fiber (Thorlabs, M42L01) acting as a pinhole. The output of the fiber is connected to a fiber switch (DiCon, MEMS 1x2 Switch Module) which can switch the collected emission to either a 50:50 visible fiber splitter (Thorlabs, FCMM50-50A-FC) or a spectrometer (Princeton Instruments, IsoPlane160 and Pixis 100 CCD). The outputs of the fiber splitter are sent to two identical single-photon counting modules (SPCM, Laser

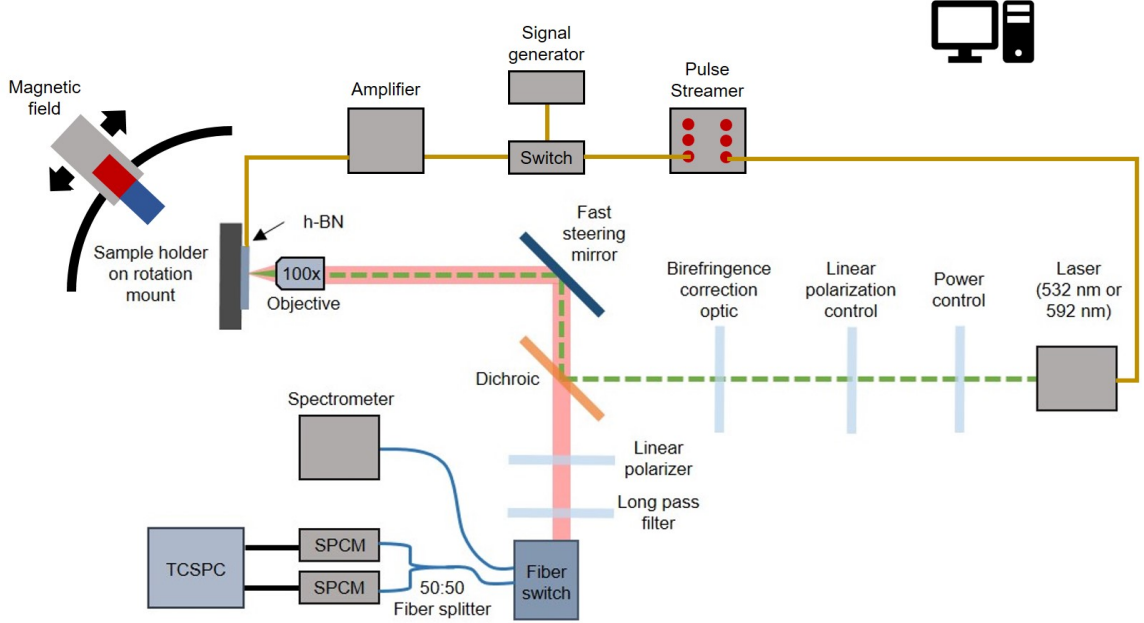


Figure 4: Experimental Setup. A simplified version of the room temperature optical setup showing the essential optical and electronic components used to probe the QEs in h-BN. The green dashed line represents the 532 nm (green) excitation path which can be switched to 592 nm (orange) excitation.

Components, Count T-100) resulting in a Hanbury Brown and Twiss interferometer. The outputs of the SPCMs are either measured by a data acquisition card (National Instruments, DAQ6323) for general-purpose counting or a time-correlated single-photon counting (TCSPC) module (PicoQuant, PicoHarp 300) for recording the photon time-of-arrival information with a full system resolution of ~ 350 ps.

The magnetic field is applied using a neodymium magnet mounted (K&J Magnetics DY0Y0-N52) on to a linear stage (Zaber Technologies T-LSR160D) that enables magnetic field strength variation. The stage is mounted on a home-build goniometer that allows variation in magnetic field orientation from 0° to 90° , where 0° corresponds to an in-plane applied magnetic field with respect to the sample plane. The magnetic field strength as a function of stage position and orientation on the goniometer is calibrated at the sample using a hall probe (LakeShore 425 Gaussmeter). The available magnetic field strength is 0 G to 470 G. Magnetic field calibration was performed at each dipole orientation presented

in Fig. 18(d)-(e) to account for the shift in the distance of the SPE from the magnet on rotating the sample. This shift is up to 2 mm in X and Y direction, enough to alter the effective magnetic field by several gauss. With the sample removed, the gaussmeter is carefully placed at the same position aided by the laser beam coming out of the objective. The objective position corresponds to that of each orientation. Multiple calibrations are performed to determine the systematic error in positioning the gaussmeter. The magnetic field calibration error is taken into account in the data presented in Fig. 18(d)-(e).

Figure 5 depicts a schematic of the radio frequency (RF) instrumentation used for spin dynamics measurements. An arbitrary waveform generator (Swabian Pulse Streamer 8/2) is used for optical and microwave pulse protocols by syncing timings and outputs of various electronics. A signal generator (DS Instruments SG6000LD) is used as a source of microwaves. The arbitrary waveform generator is used to modulate the microwaves via a high isolation switch (Minicircuits ZASSWA-2-50DRA+). The microwave signal is further amplified using a power amplifier (Minicircuits ZHL-20W-13+ or ZHL-15W-422-S+). A directional coupler (L3-Narda 4216-20) at the output of the power amplifier allows for monitoring the input microwave pulses on an oscilloscope (Tektronix TDS 2024). A custom-made microwave chip is connected to the output of the directional coupler at one end and to a 50 ohm terminator at another end. The patterned substrate consisting of the h-BN flakes is glued to the microwave chip using rubber cement (Fig. 6). Using a wire bonder (Kulicke and Soffa 4523), two bonding pads on the microwave chip are connected with a thin aluminum

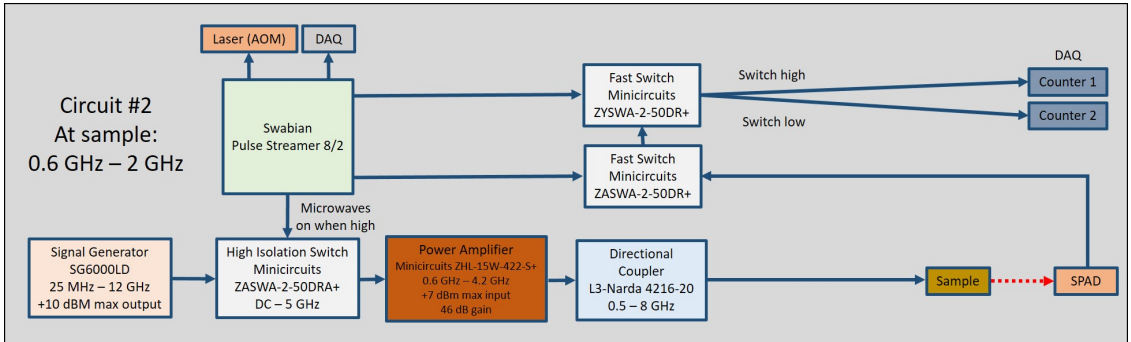


Figure 5: Microwave Circuit for Time-Domain and Spin Dynamics Measurements.

wire that allows for the transmission of the microwaves. The aluminum wire passes over the h-BN flake and is ~ 50 μm away from the single spin discussed in Chapter 6. The SPCM used for the optical readout is connected to two fast switches (Minicircuits ZYSSWA-2-50DR+) connected in series. The two switches are controlled by the function generator. The first switch referred to as the counting switch is used to send the signal coming from SPCM to next switch for recording or to a 50 ohm terminator if discarding. The second switch referred to as the routing switch takes the signal from the counting switch and routes it to one of the two counters on the data acquisition card. The two counters are devoted to collecting either the signal PL or the reference PL in the measurements. The optical pulse is modulated via an acousto-optic modulator (Isomet AOM 1250C) connected to the function generator. An output of the arbitrary waveform generator connected to the data acquisition card is used as a clock reference.

Custom software control (Appendix B) was developed in MATLAB that enabled automated data acquisition via hardware and software integration of free-space optics, optomechanical components, control electronics, RF instrumentation, etc. A custom-designed general purpose user-interface simplified and speed up various measurements.

4.3. Microwave Chip

Microwave substrates were designed and fabricated for performing spin dynamics measurements by transmitting microwaves through the metal which generate the required AC magnetic field for spin manipulation. However, the microwave substrates were incompatible with the annealing process due to the diffusion of metal in to the substrate (see Appendix C). Instead, non-microwave substrates were used and an aluminum wire passing over the substrate used for microwave transmission. The sample consisted of a non-microwave substrate glued to a custom-designed microwave chip with SMA connectors as shown in Fig. 6. Prior to that, the non-microwave substrate consisting of h-BN flakes was annealed. The bonding pads labeled 4 and 5 on the microwave chip are connected by a thin aluminum wire using a wire bonder (Kulicke and Soffa 4523). The wire bonding is done carefully such that the aluminum wire is as close as possible to the h-BN flake of interest (consisting of spin-based QEs

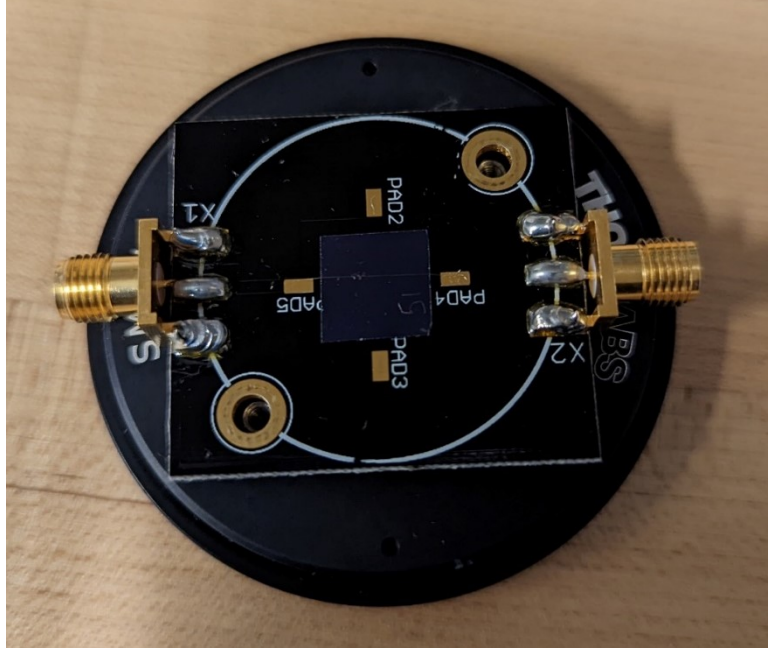


Figure 6: Microwave Chip

of interest pre-characterized using PECS as discussed in Section 6.2). The chip is secured to a threaded adapter which is mounted in the setup on a rotation stage. The chip is connected to the microwave circuit shown in Fig. 5, with one SMA connector $50\ \Omega$ terminated.

4.4. Photoluminescence Characterization

We raster the fast steering mirror to acquire μ -PL images of the h-BN flake and isolated SPEs by recording the counts at each pixel. The signal and background of a SPE is determined from a two-dimensional Gaussian fit to its μ -PL image. For PL saturation curves, the steady-state PL signal is acquired as a function of excitation power and fit using an empirical saturation model,

$$C(P) = \frac{C_{\text{sat}}P}{P + P_{\text{sat}}} \quad (4.1)$$

where C is the background-subtracted, steady-state PL count rate, P is the optical excitation power, C_{sat} is the saturation count rate, and P_{sat} is the corresponding saturation power. The polarization scans are acquired to measure the linear excitation and emission polarization properties. The measurements are acquired by varying the linear polarization

of the excitation laser or by passing the PL through a linear polarizer placed in the collection path. The polarization dependent PL signal is determined by recording the steady-state PL of the SPE at each polarization angle and subtracting the background PL measured at a spatial location offset $\sim 1 \mu\text{m}$ from the SPE. A randomized order of the polarization angles minimizes effects of drift and hysteresis. For excitation polarization measurements, the linear polarizer in the collection path is removed. For emission polarization measurement, the excitation polarization is set to maximize the PL. The data are fit using the model function

$$I_s(\theta) = A_s \cos^2(\theta - \theta_s) + B_s \quad (4.2)$$

where s indicates excitation (ex) or emission (em), A_s is the amplitude, θ_s is the polarization angle of maximum intensity, and B_s is the offset. From the fit results, the visibility is calculated as

$$V_s = \frac{I_s^{\max} - I_s^{\min}}{I_s^{\max} + I_s^{\min}} = \frac{A_s}{A_s + 2B_s} \quad (4.3)$$

where I_s^{\max} and I_s^{\min} are the maximum and minimum PL signal, respectively. The misalignment between the excitation and emission polarization angles is

$$\Delta\theta = \theta_{\text{ex}} - \theta_{\text{em}}. \quad (4.4)$$

The PL spectra are collected as multiple exposures and averaged after correcting for dark counts, cosmic rays and wavelength-dependent photon collection efficiency. The PL spectra are measured as a function of wavelength, λ and binned to determine spectral distribution function, $S(\lambda)$. To analyze the vibronic coupling, the measured spectra must be converted to a form suitable for analysis with the general theory of electron-phonon coupling in three dimensional crystals [49, 136]. To do this, the spectral probability distribution function is obtained through

$$S(E) = S(\lambda) \frac{hc}{E^2} \quad (4.5)$$

where h is Planck's constant, c is the speed of light, and E is the photon energy. The

emission lineshape, $L(E)$ is derived from $S(E)$ as

$$L(E) = \frac{S(E)}{E^3} \quad (4.6)$$

which accounts for the photon-energy dependence of spontaneous emission. The emission lineshape is then fit following the method described in [65]. From the fit, the following free parameters are determined: the ZPL energy, E_{ZPL} , the ZPL Lorentzian linewidth, Γ_{ZPL} , the Huang-Rhys factor, S_{HR} , and the one-phonon vibronic coupling lineshape, approximated as an interpolated vector of values spanning the phonon spectrum in h-BN. The Debye-Waller factor, w_{DW} , can be calculated from $w_{\text{DW}} = e^{-S_{\text{HR}}}$.

4.5. Photon Emission Correlation Spectroscopy

Temporal correlations between fluorescence photons reveal information about a QE's excitation and emission dynamics. In this thesis, PECS was used for two purposes: to verify the single-photon purity of the QEs and to probe their optical dynamics as a function of optical excitation rate. We calculate $g^{(2)}(\tau)$ from the photon arrival times acquired from two detectors in a Hanbury Brown and Twiss interferometer using a time-correlated single-photon counting module. For QEs in h-BN, the timescales over which antibunching and bunching occur can vary over at least 6 orders of magnitude [65, 66, 194]. For this reason, we initially calculate and analyze $g^{(2)}(\tau)$ over a logarithmic scale spanning from 100 ps to 1 s as shown in Fig. 7 for five QEs (discussed in detail in Chapter 5). We fit the background-corrected [31] data using a general empirical model for a QE's optical dynamics with a varying number of levels:

$$g^{(2)}(\tau) = 1 - C_1 e^{-\gamma_1 |\tau|} + \sum_{i=2}^n C_i e^{-\gamma_i |\tau|} \quad (4.7)$$

Here, γ_1 is the antibunching rate, C_1 is the antibunching amplitude, γ_i for $i \geq 2$ are bunching rates, and C_i for $i \geq 2$ are the corresponding bunching amplitudes. The data are fit by multiple instances of Eq. 4.7 with $n = [2, 5]$. We determine the number of resolvable timescales, n , by calculating and comparing the Akaike Information Criterion (AIC) and the reduced chi-squared statistic for each best-fit model. The right column of Fig. 7 shows

standardized residuals for each QE for the best-fit empirical model (red curve in the plots in left column).

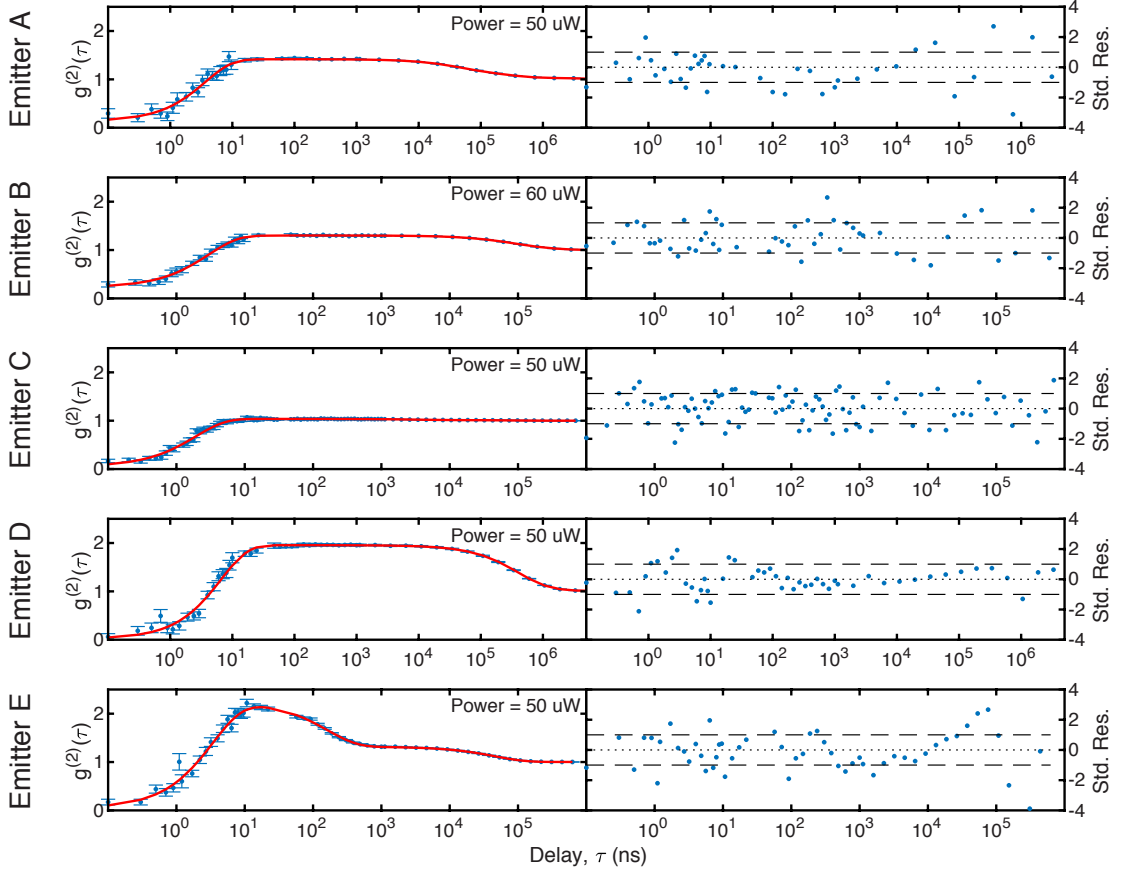


Figure 7: Second-Order Photon Autocorrelation Function. (Column 1) Experimental autocorrelation data, $(g_{\text{exp}}^{(2)}(\tau))$; blue data points), binned on a logarithmic delay axis and fit using an empirical model discussed in the text $(g_{\text{fit}}^{(2)}(\tau))$; red curve). Error bars represent Poissonian uncertainties, $\sigma_g(\tau)$ based on the photon counts in each bin. (Column 2) Standardized residuals, $[g_{\text{exp}}^{(2)}(\tau) - g_{\text{fit}}^{(2)}(\tau)]/\sigma_g(\tau)$.

In optical dynamics models, an N -level system is characterized by $N - 1$ rates, corresponding to the non-zero eigenvalues of the generator matrix (see, *e.g.*, Eq. 4.16). Therefore, the inferred value of n places a lower limit on the number of electronic levels required to describe the observations, $N \geq n + 1$. We extract the rates, amplitudes, and their corresponding uncertainty from these fits for comparisons with theoretical simulations. The resultant fit parameters of the best-fit empirical model determined for each QE in Fig. 7 are

Table 1: Long-Timescale Autocorrelation Function Fit Parameters.

Quantum Emitter	A	B	C	D	E
Excitation wavelength	592 nm	592 nm	532 nm	592 nm	532 nm
χ_{red}^2	1.801	1.202	1.085	1.031	2.872
n	4	3	3	3	3
C₁	1.285 ± 0.052	1.076 ± 0.029	0.988 ± 0.020	1.938 ± 0.039	2.204 ± 0.041
τ₁(ns)	3.66 ± 0.31	2.97 ± 0.16	1.91 ± 0.08	6.56 ± 0.34	3.50 ± 0.16
C₂	0.208 ± 0.002	0.193 ± 0.001	0.023 ± 0.001	0.725 ± 0.028	0.928 ± 0.022
τ₂(μs)	41.200 ± 0.617	75.088 ± 0.600	3.429 ± 0.218	354.67 ± 13.62	0.163 ± 0.005
C₃	0.172 ± 0.002	0.108 ± 0.002	0.013 ± 0.000	0.219 ± 0.029	0.315 ± 0.002
τ₃(μs)	252.49 ± 2.64	264.32 ± 2.21	90.66 ± 2.27	972.30 ± 48.39	46.64 ± 0.31
C₄	0.035 ± 0.001	-	-	-	-
τ₄(ms)	5.622 ± 0.317	-	-	-	-

summarized in Table 1. In order to assess the single-photon purity associated with the value of $g^{(2)}(0)$, we perform a subsequent analysis of $g^{(2)}(\tau)$ calculated over a linear scale of delay times, $\tau \in [-20, 20]$ ns. Examples of such data are shown in Fig. 8, along with constrained fits in which only the antibunching parameters γ_1 and C_1 are allowed to vary, and which account for the instrument response function (IRF) associated with detector timing jitter. To account for the timing jitter in the single photon counting modules, the IRF is found by measuring the autocorrelation signal of an attenuated picosecond pulsed laser sent through the Hanbury Brown and Twiss interferometer and binned over the same linear scale as the emitter. A convolution of the IRF with a modified Eq. 4.7 is fit to the background-corrected

data, given by

$$\tilde{g}^{(2)}(\tau) = \text{IRF} * (1 - C_1 e^{-\gamma_1 |\tau|} + C_B(\tau)) \quad (4.8)$$

where $C_B(\tau)$ is the total bunching contribution found from the logarithmic scale analysis (first step) and only C_1 and γ_1 are allowed to vary. The autocorrelation at zero-delay is then given by

$$\tilde{g}^{(2)}(0) = 1 - C_1 + \sum_{i=2}^n C_i \quad (4.9)$$

which is used to determine the purity of single-photon emission from the emitter.

For a given emitter, all autocorrelation measurements are performed with the excitation polarization set at the angle of maximum excitation and the collection path has the polarizer removed. Due to the varying emitter brightness, which affects the signal-to-noise ratio of the antibunching signal, measurements are integrated for 10 s to 140 min with repositioning occurring every 2 min.

4.5.1. Background Correction

Background correction is done to account for the background and incoherent light detected along with the signal which can affect the autocorrelation function. The following two background correction techniques are used:

1. Recording background from an offset spot: The autocorrelation data was acquired from a background spot, same as the emitter. The background spot is an offset spot, $\sim 1 \mu\text{m}$ from the emitter which seems to emulate the true background. The background data was acquired for the equivalent time as the emitter, with all other experimental conditions such as excitation power kept same. From the background data, the average background count rate was determined. This technique was applied to emitters A and B.
2. Recording background from a two-dimensional scan: Instead of recording background data of an offset spot, X and Y line ($\mu\text{-PL}$) scan of the emitter were acquired. Since the emitter is tracked during the acquisitions, the $\mu\text{-PL}$ line scans along X and Y pass

through the center of the emitter. A two-dimensional Gaussian fit to the line scans provides the background and signal of the spatially isolated emitter. This technique speeds up the data acquisition by a factor of 2 since the data from an offset spot is no longer needed to be acquired. This technique better approximates the background since the estimation is done right around the emitter, instead of an offset spot. This technique was applied to emitters C, D and E, and adopted as future autocorrelation background correction technique.

Using the background and signal acquired, following background correction equations from Ref. [31] are used to determine background-corrected autocorrelation function:

$$\rho = \frac{Signal}{Signal + Background} \quad (4.10)$$

$$g_{bkgd}^{(2)}(\tau) = \frac{g^{(2)}(\tau) - (1 - \rho^2)}{\rho^2} \quad (4.11)$$

where $g^{(2)}(\tau)$ is determined from the emitter and $g_{bkgd}^{(2)}(\tau)$ is the background-corrected autocorrelation function.

4.5.2. Akaike Information Criterion

For a given set of data, the Akaike information criterion (AIC) is a quantitative method to determine the relative quality of a collection of statistical models. Using the AIC, the relative quality of each of the models compared can be estimated. It can be applied to any data and fitting routines. Thus, it can be used to determine which model best fits to a given data set. However, it does not determine absolute quality. Using the AIC, the relative quality of Eq. 4.7 for different n is determined. The *likelihood* of a model ($n = [2, 5]$) explaining the actual data is determined by comparing the AIC of each model. The AIC is defined as:

$$AIC = 2p - 2 \ln(\mathcal{L}) \quad (4.12)$$

where p is the number of fit parameters in the model, and $\ln(\mathcal{L})$ is the log-likelihood function. Assuming Gaussian uncertainties, the second term becomes

$$2 \ln(\mathcal{L}_G) = - \sum_{i=1}^N \left[\frac{(c_i - m_a(x_i))^2}{\sigma_i^2} + \ln(\sigma_i^2) \right] - N \ln(2\pi) \quad (4.13)$$

where N is the number of data points, c_i is the measured value of the i^{th} data point, m_a is the model function, $m_a(x_i)$ is the model predicted value of the i^{th} data point, x_i is the independent i^{th} data point and σ_i is the standard deviation of the i^{th} data point. The likelihood of a model to explain the actual data from a collection of models is determined by calculating the weight of the model, defined as:

$$w_a = \exp((\text{AIC}_{\min} - \text{AIC}_a)/2) \quad (4.14)$$

where w_a is the weight of the a^{th} model, AIC_{\min} is the minimum AIC value among all models and AIC_a is the AIC value of the a^{th} model. The model with highest w best explains the actual data, amongst the collection of models. However, for relatively close values of two w_a , a simpler model could be selected. Thus, the AIC is used to determine relative quality of n for $n = [2, 5]$.

4.6. Electronic Level Structure Simulations

A four-level optical rate equation is used to model aspects of the observed autocorrelation data. The model is defined as

$$\dot{\mathbf{P}} = \mathbf{G}\mathbf{P} \quad (4.15)$$

where \mathbf{P} is a vector of state populations, P_i , and \mathbf{G} is a generator matrix describing the transition rates. For the model shown in Fig. 13(a),

$$\mathbf{G} = \begin{pmatrix} -\Gamma_{13} & \Gamma_{21} & 0 & \kappa_{41} \\ 0 & -\Gamma_{21} - \kappa_{24} & \kappa_{32} & 0 \\ \Gamma_{13} & 0 & -\kappa_{32} & 0 \\ 0 & \kappa_{24} & 0 & -\kappa_{41} \end{pmatrix} \quad (4.16)$$

where Γ_{13} is the excitation rate, Γ_{21} is the radiative emission rate, and κ_{ij} are nonradiative rates that are either fixed or proportional to the excitation rate. The autocorrelation function is proportional to the probability that the system is found in the radiative state, P_2 , given the system started in state P_1 following the detection of a photon, and normalizing by the steady state population of P_2 . This is given by

$$g^{(2)}(\tau) = \frac{P_2(t_2|P(t_1) = (1, 0, 0, 0))}{P_2(\infty)} \quad (4.17)$$

where $\tau = t_2 - t_1$. The differential equation (Eq. 4.15) given the initial state is solved in MATLAB using the function `ode15s`. Timing resolution limitations and shot noise are added to the simulated autocorrelation function to best recreate the measurements. To model timing resolution, the simulated data are only analyzed for $t_0 \geq 0.5$ ns. To include shot noise, a standard deviation, σ_0 , is set for the first delay time. Assuming shot noise, this standard deviation is converted to mean number of photons as

$$\langle N_0 \rangle = \sigma_0^{-2} \quad (4.18)$$

The logarithmic-scale processing results in the average number of photon correlations detected in each bin increasing linearly with the delay time,

$$\langle N(\tau) \rangle = \langle N_0 \rangle \frac{\tau}{\tau_0} \quad (4.19)$$

From this, a simulated, noisy $g^{(2)}(\tau)$ is calculated as

$$g^{(2)}(\tau)_{\text{Noisy}} = \frac{\text{Pois}(g^{(2)}(\tau) \langle N(\tau) \rangle)}{\langle N(\tau) \rangle} \quad (4.20)$$

where `Pois` is a Poission distribution. The simulated autocorrelation data are analyzed with the same fitting framework as the measured data. The general model parameters are as follows: $\Gamma_{21} = 300$ MHz, $\Gamma_{13} = a\Gamma_{21}$ where $a = [.01, 10]$, $\Gamma_{12} = x\Gamma_{13}$ where $x = [0, 2]$, $\kappa_{32} = 600$ MHz. For the spontaneous bunching, $\kappa_{24} = 60$ kHz and $\kappa_{41} = 30$ kHz. For the

pumped bunching, $\kappa_{24} = 6 \text{ kHz/MHz} \times \Gamma_{13}$ and $\kappa_{41} = 3 \text{ kHz/MHz} \times \Gamma_{13}$. See Section 5.5 for detailed discussion.

CHAPTER 5 : Optical Dynamics of Quantum Emitters

This chapter discusses probing the optical dynamics of quantum emitters in h-BN to understand the internal dynamics arising due to the electronic level structure of the underlying defect. Using PECS – radiative and nonradiative transition rates are probed and compared to numerical simulations of electronic level structure models. This chapter details the results and discussion and is organized as follows: Section 5.1 discusses the motivation of the work; Section 5.2 details the optical characteristics of five well-isolated QEs across three samples; Section 5.3 discusses single-photon purity of QEs in h-BN; Section 5.4 details investigating the QEs’ optical dynamics using PECS as a function of excitation power and wavelength; Section 5.5 discusses models for the electronic level structure and simulating the corresponding optical dynamics; Section 5.6 discusses the interpretation of the QEs’ PL, spectra and polarization; Section 5.7 discusses the interpretation of the QEs’ optical dynamics; Section 5.8 discusses theoretical defect proposals and Section 5.9 concludes the chapter.

This chapter and Appendix E have been adapted with permission from Patel et al., 2022 [155]². The sample preparation was done in close collaboration with Benjamin Porat. The experimental methods of this chapter were completed in a close collaboration with Dr. David A. Hopper, Dr. Tzu-Yung Huang, Dr. Mark Turiansky, Jordan Gusdorff, Rebecca E.K. Fishman and Prof. Chris G. Van de Walle. This work was primarily supported by the National Science Foundation (NSF) award DMR-1922278. The use of facilities and instrumentation in the Singh Center for Nanotechnology at the University of Pennsylvania was supported by NSF through the National Nanotechnology Coordinated Infrastructure (NNCI; Grant ECCS-1542153) and the University of Pennsylvania Materials Research Science and Engineering Center (MRSEC; DMR-1720530).

²This manuscript was accepted to appear at PRX Quantum at the time of writing of this thesis.

5.1. Introduction

Despite intense interest in h-BN’s QEs, their chemical and electronic structures remain uncertain, as do key details regarding their optical, spin, and charge dynamics. The pronounced heterogeneity of observations suggests that QEs originate from multiple distinct defect structures [28, 65, 185, 194, 227]. Ultraviolet emission around 4.1 eV has been attributed to the carbon dimer $C_B C_N$ [135], whereas near-infrared emission around 1.7 eV and an associated ODMR signal is attributed to the negatively-charged boron vacancy, V_B^- [83]. For QEs in the visible spectrum, experiments utilizing various forms of electron and optical microscopy, spectroscopy, and materials growth and treatments have generated a detailed, yet complicated, empirical understanding of the QEs’ creation, stabilization, and principal optical signatures [26, 30, 40, 46, 47, 60, 61, 68, 71, 80, 84, 88, 90, 95, 103, 104, 140, 186, 191, 218]. Theoretical work suggests that vacancies and their complexes, along with substitutional carbon atoms and dangling bonds, are likely candidates, although consensus is still lacking [52, 116, 167, 190, 197, 209]. Specific candidates include $V_N N_B$, $V_N C_B$, $V_B C_N$, and the boron dangling bond.

Even less is known about the visible QEs’ optical dynamics. Optical dynamics arise from a QE’s electronic structure together with radiative and nonradiative transitions between electronic states. State transitions can involve multiple processes including electron-phonon interactions, intersystem crossings between different spin manifolds, and ionization or recombination events. For QEs in h-BN, previous studies have reported photon bunching associated with metastable dark states [40, 65, 66], and yet the nature of these states and the transitions between them remains unclear. Some QEs exhibit magnetic-field-dependent modulation of their photoluminescence (PL) signal, consistent with a spin-dependent intersystem crossing, whereas others do not [66, 184]. An ODMR signal was observed for a particular QE under excitation at 633 nm but not at 532 nm [39]. Such observations present a complicated picture of the visible QEs, likely involving multiple defect classes (*e.g.*, different chemical structures or charge states), strong local perturbations, and complex excitation and relaxation pathways. Improved understanding of the QEs’ optical dynamics can resolve

these mysteries. Such understanding is also a prerequisite to designing quantum control protocols that would facilitate their use in quantum technologies. Here, we use quantitative spectral, spatial, and temporal PL spectroscopy to investigate the optical dynamics of h-BN’s QEs.

Photons emitted by a QE carry a wealth of information about its electronic structure and optical dynamics. For vibronic optical transitions, the photon energy and polarization distributions reflect the details of electron-phonon coupling and optical dipole selection rules, respectively. The QEs in h-BN generally exhibit linearly-polarized PL and strong electron-phonon coupling associated with a single vibronic transition [65], and yet other experimental and theoretical evidence points to the involvement of multiple excited states in the optical dynamics [55, 104, 169, 197]. Time-dependent measurements provide complementary information. The second-order photon autocorrelation function, $g^{(2)}(\tau)$, is widely used to identify SPEs. As a more general analytical tool, PECS yields quantitative information about a QE’s optical dynamics [70]. Qualitatively, we distinguish between photon antibunching ($g^{(2)}(\tau) < 1$) as a signature of non-classical light, with single-photon emission as a special case when $g^{(2)}(0) = 0$, and photon bunching ($g^{(2)}(\tau) > 1$ for $\tau \neq 0$) as a signature of dark, metastable states accessed via nonradiative transitions. Quantitative measurements of $g^{(2)}(\tau)$ as a function of optical excitation power or wavelength can elucidate a QE’s excitation and emission pathways as well as bunching mechanisms.

Prior observations of h-BN’s visible QEs feature both bunching and antibunching signatures, although with some unusual, conflicting patterns. Some QEs respond to applied dc and ac magnetic fields in a manner consistent with spin-mediated intersystem crossing transitions, whereas others do not [39, 66, 184]. A lack of evidence for pure single-photon emission motivated a proposal that h-BN’s QEs occur in pairs as “double defects” [27]. Here, we compare quantitative PL spectroscopy and PECS measurements of h-BN’s QEs with theoretical simulations. We show that QEs in room-temperature h-BN can exhibit pure single-photon emission, with $g^{(2)}(0) = 0$ within experimental uncertainty. Furthermore, we

find evidence for multiple electronic states connected by radiative and nonradiative transitions, with associated timescales spanning over five orders of magnitude. Comparing the experiments to theoretical proposals, we find that the boron dangling bond model provides a consistent, quantitative understanding of the observations for individual QEs as well as their heterogeneity.

5.2. Photoluminescence, Spectral and Polarization Properties

Table 2: The Samples, Quantum Emitters and Sample Treatments.

Sample ¹	I	II	III
h-BN crystal used for exfoliation²	1	1	2
Quantum emitters	A	B	C, D & E
Pre-annealing treatment	Plasma cleaned at 50 W in 50 sccm O ₂ for 5 minutes	Plasma cleaned at 50 W in 50 sccm O ₂ for 5 minutes	Plasma cleaned at 50 W in 50 sccm O ₂ for 5 minutes
Annealing treatment	850 °C for 2 hours in low pressure Ar atmosphere	1. 850 °C for 1 hour in low pressure Ar atmosphere 2. Sample was in scanning electron microscope chamber but not directly exposed to e-beam ³ 3. 850 °C for 2 hours in low pressure Ar atmosphere	850 °C for 2 hours in low pressure Ar atmosphere

¹ Sample represents different substrates.

² Crystal 1 and 2 represent crystals in different orders purchased from HQ Graphene, ~2 years apart.

³ The QE was not found post treatment 1 and 2. It was only found post treatment 3.

We used a custom-built confocal microscope to study individual QEs in h-BN under ambient conditions (Sec. 4.2). Table 2 highlights the crystal from which the h-BN flake under study came and the treatments it underwent. Appendix C presents empirical observations of effect of annealing conditions on the creation and photophysical properties of

QEs. The QEs are illuminated with either of two continuous-wave lasers operating at 532 nm and 592 nm wavelengths, where excitation power and polarization are controlled. To differentiate between excitation wavelengths in this work, data recorded under 532 nm (592 nm) excitation are plotted in deep jungle green (light brown) in the relevant figures. Some QEs disappeared during experiments, hence the set of measurements is not identical for each QE.

Figure 8 summarizes the PL characterization measurements and Table 3 summarizes photoluminescence properties of the QEs - data presented in Fig. 8 and 9. In Fig. 8 each row corresponds to a particular QE (labeled A-E), and each column corresponds to a different experiment. The first column includes μ -PL images of each QE, acquired by scanning a fast steering mirror and recording the accumulated counts at each pixel. A two-dimensional Gaussian fit to each μ -PL image yields the background and signal levels for subsequent studies. The second column displays $g^{(2)}(\tau)$ measurements over short delay times, showing characteristic antibunching dips fit by an empirical model for a multi-level system (Sec. 4.5). The third column displays the steady-state PL signal as a function of excitation power. The fourth column of Fig. 8 presents PL emission spectra and polarization measurements. In each PL spectrum, the long pass filter cut-on wavelength is indicated as a vertical dotted line, and the excitation wavelength is a solid line. The inset to each PL spectra panel presents measurements of the QE's excitation and emission polarization properties. These data are acquired by varying the linear polarization of the excitation laser (colored circles) or by passing the PL through a linear polarizer placed in the collection path (black squares). For excitation polarization measurements, the linear polarizer in the collection path is removed. For emission polarization measurement, the excitation polarization is set to maximize the PL. At each polarization setting, we record the steady-state PL intensity as well as a background intensity from a spatial location offset $\sim 1 \mu\text{m}$ from the QE, which is subtracted to yield the PL signal. The order of the polarization angles is set randomly to minimize effects of drift and hysteresis. Solid curves are fits to the data.

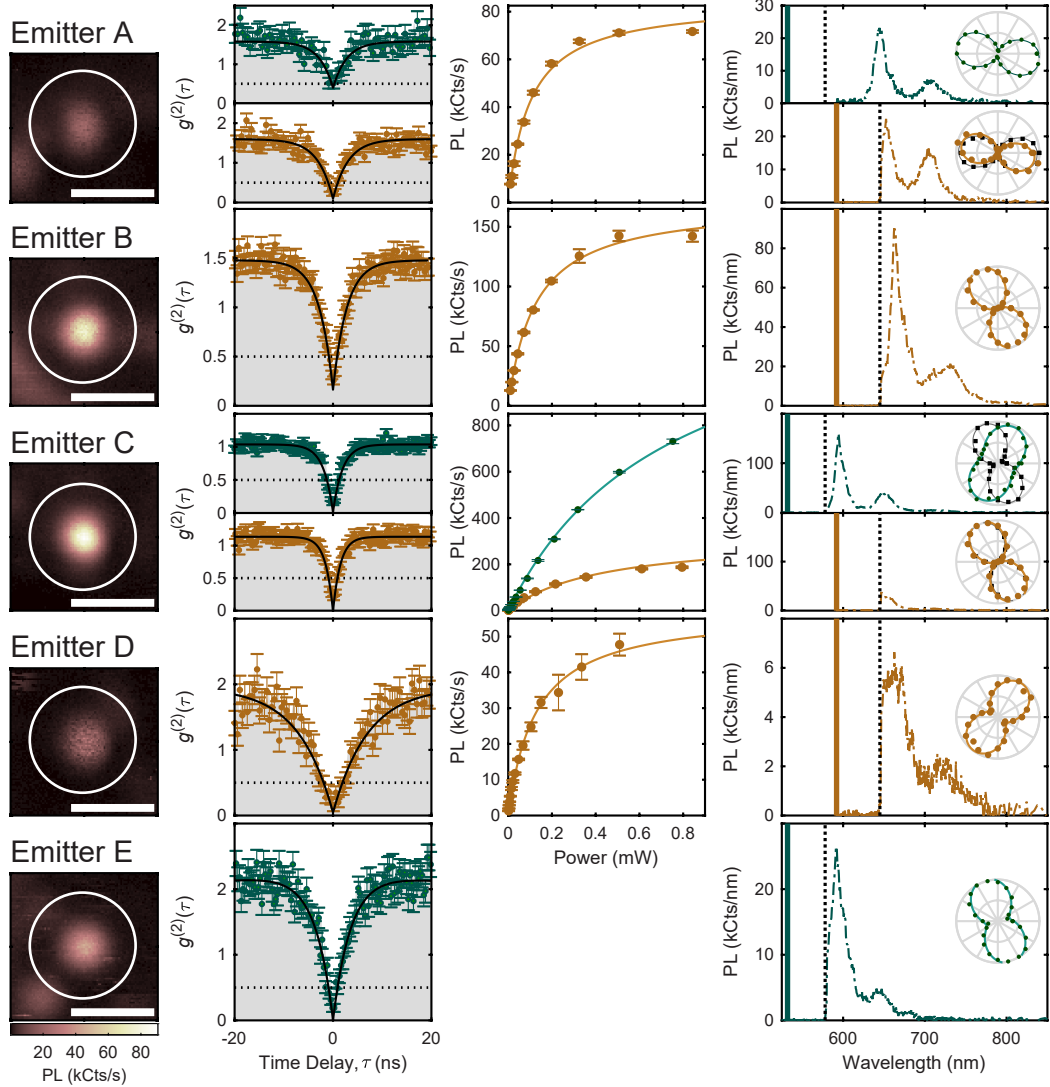


Figure 8: Photoluminescence Characterization. (Column 1) μ -PL images of the QEs (circled), acquired under 592 nm (QEs A-D) or 532 nm (QE E) excitation. Scale bars denote 1 μm . (Column 2) Second-order photon autocorrelation function (colored points), fit using an empirical model discussed in the text (black curve). Error bars represent Poissonian uncertainties based on the photon counts in each bin. (Column 3) Steady-state, background-subtracted PL intensity as a function of excitation power (points), fit using an empirical saturation model discussed in the text (solid curves). Saturation data for QE E are missing since the QE disappeared before the measurement could be performed. Error bars represent one standard deviation based on three measurement repeats. (Column 4) PL spectra and polarization data. Vertical colored lines represent the excitation laser wavelengths, and black dotted lines indicate cut-on wavelengths for long-pass optical filters in the collection path. Insets: PL intensity as a function of linear excitation polarization angle (colored circles) or filtered by linear polarization angle in emission (black squares). Solid curves are fits to the data using an empirical model discussed in the text.

Table 3: Steady-State PL as a Function of Power, PL Spectra Analysis and Optical Polarization Properties.

Quantum Emitter	A	B	C ¹	D ²	E
C_{sat}^{592} (kCts/s)	84.4 ± 5.1	170.1 ± 8.4	323.0 ± 38.3	57.2 ± 4.1	N/A
P_{sat}^{592} (μ W)	100.1 ± 18.7	124.2 ± 18.0	424.6 ± 124.3	126.2 ± 22.54	N/A
E_{ZPL} (eV)	1.927	1.871	2.086	N/A	2.1
S_{HR}	2.79	2.35	2.48	N/A	2.12
w_{DW}	0.06	0.095	0.084	N/A	0.12
Γ_{ZPL} (meV)	4.9	4.7	4.2	N/A	9.2
θ_{ex}^{532} (deg) ³	168.17 ± 0.97	N/A	64.54 ± 1.34	N/A	108.77 ± 1.26
V_{ex}^{532} (%) ³	83.6 ± 1.4	N/A	38.7 ± 1.2	N/A	56.1 ± 1.4
θ_{ex}^{592} (deg) ³	169.71 ± 2.76	77.66 ± 0.81	118.29 ± 1.18	53.23 ± 2.02	N/A
V_{ex}^{592} (%) ³	100.0 ± 5.7	80.88 ± 1.7	83.0 ± 2.9	57.6 ± 2.3	N/A
θ_{em}^{592} (deg) ³	173.83 ± 1.47	N/A	118.29 ± 0.66	N/A	N/A
V_{em}^{592} (%) ³	88.9 ± 2.4	N/A	90.5 ± 1.9	N/A	N/A

¹ $C_{\text{sat}}^{532} = 1457.7 \pm 98.1$ kCts/s, $P_{\text{sat}}^{532} = 752.7 \pm 81.9$ μ W, $\theta_{\text{em}}^{532} = 111.09 \pm 0.81^\circ$, $V_{\text{em}}^{532} = 82.9 \pm 1.9\%$.

² PL spectral information is incomplete. ZPL cutoff by the filter.

³ Excitation (θ_{ex}) and emission (θ_{em}) dipole orientation, excitation (V_{ex}) and emission (V_{em}) visibility.

5.2.1. Spectral Emission Lineshapes

For spectra that are not cut off by the excitation filter (namely, the 532 nm excitation spectra for QEs A, C, and E, and the 592 nm spectrum for QE B), we find that the lineshapes are consistent with a Huang-Rhys model for a vibronic transition associated with a single zero-phonon line (ZPL). We use the analysis method described by Ref. [65] to fit the observed PL spectra using an empirical model in which the ZPL energy, ZPL width, Huang-Rhys factor, and vibronic coupling lineshape are free parameters; see Sec. 4.4 for additional details. The results are shown in Fig. 9. In the left column, we plot the normalized observed emission

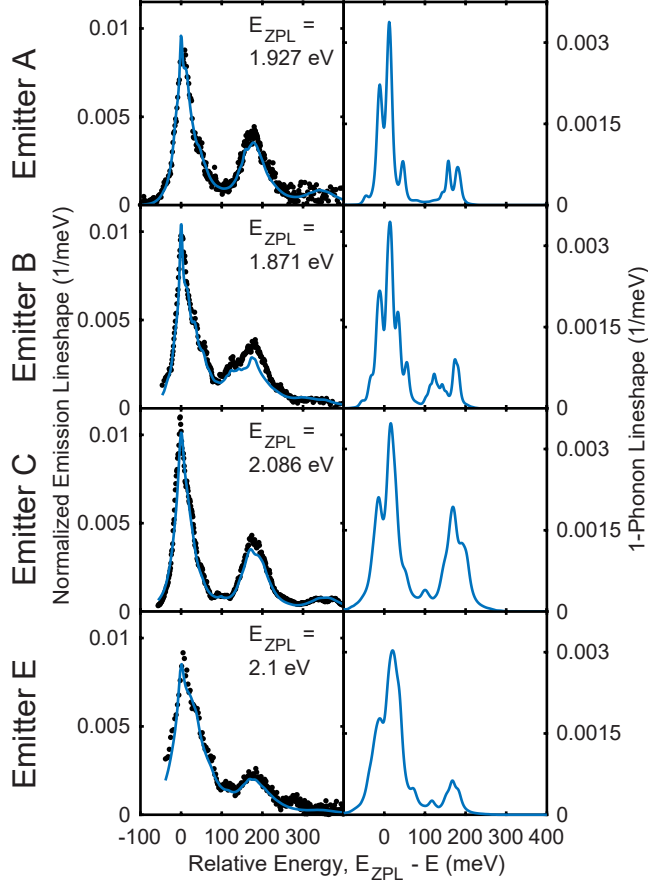


Figure 9: Photoluminescence Emission Lineshapes. (Left Column) Observed spectral emission lineshapes (black points) and fits according to Huang-Rhys theory (blue curve). Experimental uncertainties are comparable to the size of the data points. (Right Column) One-phonon vibronic coupling lineshape corresponding to the fits at left.

lineshape, $L(\Delta E) \propto S(\Delta E)/E^3$, where $S(\Delta E)$ is the spectral intensity distribution as a function of the relative energy $\Delta E = E_{ZPL} - E$, with E denoting the photon emission energy and E_{ZPL} denoting the ZPL energy. The factor $1/E^3$ accounts for the photon energy dependence in spontaneous emission. Each solid curve is the result of a weighted least-squares fit of the model to the experimental lineshapes. The right column of Fig. 9 shows the corresponding 1-phonon vibronic coupling lineshape for each fit. Best-fit parameters are reported in Table 3.

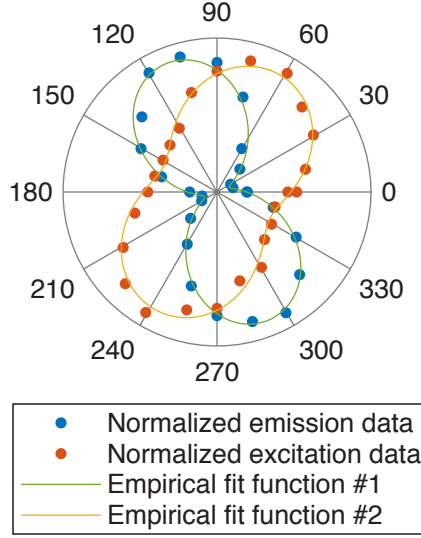


Figure 10: Quantum Emitter C: Emission and Excitation Polarization with Green Excitation. The normalized emission polarization is shown with blue circles and normalized excitation polarization is shown with orange circles. The green and yellow curves are simultaneous fits to the normalized emission and excitation polarization, respectively.

5.2.2. Simultaneous Fit of Emission and Excitation Polarization of QE C for 532 nm Excitation

The emission and excitation polarization of QE C is independently modeled using Eq. 4.2 and 4.3 to estimate its optical dipole orientation and visibility. Further, the misalignment of the emission and excitation dipole is estimated from the independent fit results using Eq. 4.4. However, the low visibility of excitation polarization for 532 nm excitation suggests superposition of multiple excitation dipoles which means the excitation pathways could be via multiple dipoles, one of them oriented along the emission dipole. To check this hypothesis, the following empirical equations are simultaneously fit to the emission and excitation polarization data:

$$I_1 = A_1 \cos^2(\theta - \theta_1) + B_1 \quad (5.1)$$

$$I_2 = A_2 \cos^2(\theta - \theta_1) + (1 - A_2) \cos^2(\theta - \theta_2) + B_2 \quad (5.2)$$

where A is the normalized amplitude, B is the normalized offset, θ_1 is the emission dipole orientation and orientation of one of the two excitation dipoles and θ_2 is the second excitation dipole. Figure 10 shows the normalized emission and excitation polarization data and the resultant simultaneous fits. Table 4 presents the fit result. The emission and first excitation dipole is oriented 111.22° . This agrees with the independent fit to the emission polarization using Eq. 4.2 which gives dipole orientation of 111.09° (Table 3). This proves the hypothesis that the excitation polarization is a superposition of two excitation dipoles, one aligned with the emission dipole and the other misaligned by $\sim 60^\circ$. Collectively, the two excitation dipoles result in an effective dipole with low visibility.

Table 4: Result of Simultaneous Fit of QE C’s Emission and Excitation Polarization.

Emission (I_1)	$0.89 \cos^2(\theta - 111.2) + 0.09$
Excitation (I_2)	$0.34 \cos^2(\theta - 111.2) + 0.66 \cos^2(\theta - 47.8) + 0.19$
Dipole 1 (θ_1)	$111.22 \pm 0.63^\circ$
Dipole 2 (θ_2)	$47.77 \pm 0.95^\circ$
Emission amplitude (A_1)	0.89 ± 0.02
Emission background (B_1)	0.09 ± 0.01
Proportion along 111.22° (A_2)	0.34 ± 0.01
Proportion along 47.77° ($1 - A_2$)	0.66 ± 0.01
Excitation background (B_2)	0.19 ± 0.01

5.3. Verifying Single-Photon Emission

Any observation of sub-Poissonian statistics, $g^{(2)}(0) < 1$, indicates the presence of quantized photon emission. The threshold $g^{(2)}(0) < 0.5$ is often used to indicate single-photon emission; however, a more precise interpretation is that a PL signal is dominated by a SPE when $g^{(2)}(0) < 0.5$ [70]. An observation of $g^{(2)}(0) > 0$ implies a non-zero probability of observing two detection events simultaneously, either due to background fluorescence, detection timing jitter, or the presence of multiple QEs. Studies of h-BN’s QEs routinely report $g^{(2)}(0) < 0.5$, however we are unaware of any prior room-temperature observations of pure single-photon emission with $g^{(2)}(0) = 0$. Partially on the basis of such observations, Ref. [27] proposed

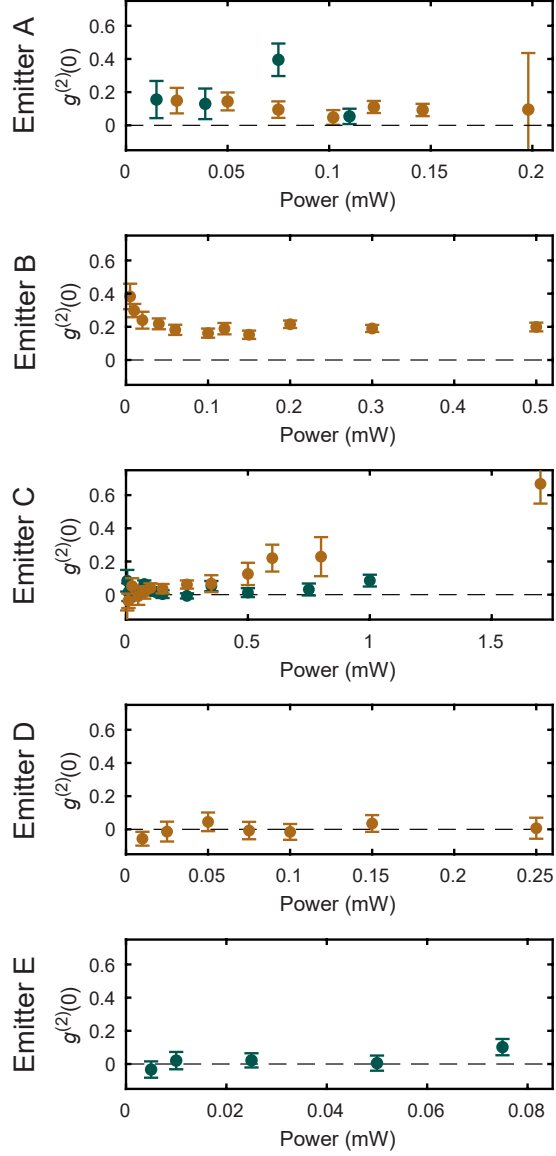


Figure 11: Single-Photon Emission Characteristics. Zero-delay photon autocorrelation function as a function of optical excitation power. Orange (green) data correspond to excitation at 592 nm (532 nm). Error bars represent one standard deviation derived from fits as described in the text.

that h-BN's QEs actually occur in pairs as double defects with parallel emission pathways.

We find that QEs in h-BN can indeed exhibit pure single-photon emission at room temperature. Figure 11 shows $g^{(2)}(0)$ for each QE as a function of excitation power. These data are corrected for background fluorescence and detector timing jitter, as described in

Appendix. For QEs C, D and E, we observe $g^{(2)}(0) = 0$ within the experimental uncertainty, particularly at low excitation powers. For QEs A and B, we observe $g^{(2)}(0) \sim 0.1 - 0.2$. The offset from zero could reflect a contribution from additional dim emitters, however we believe it is more likely to result from incomplete estimation of the background. For instance, QE B sits on an extended background feature whose contribution is not captured by our standard analysis method. For QE C, we attribute the increase in $g^{(2)}(0)$ as a function of excitation power to limitations in the instrument-response-function correction as the antibunching rate exceeds the detector timing resolution.

5.4. Probing the Optical Dynamics

Figure 12 summarizes the results of fitting the empirical model of Eq. 4.7 to PECS measurements as a function of optical excitation power. The figure includes the best-fit antibunching rate (top row) as well as the first two bunching rates and amplitudes (lower rows). The PECS data for QEs B, D, and E are best described by a three-timescale model ($n = 3$), whereas QE A exhibits four resolvable timescales ($n = 4$). For QE C, we resolve two or three timescales depending on the excitation power and wavelength. The best-fit results for QE A's third bunching component (γ_4 and C_4), as well as the antibunching amplitude (C_1) for all emitters are shown in the Appendix Figures 36 and 35, respectively. The PL decay rate of QE A was directly measured to be 355 MHz using a picosecond pulsed laser (Appendix Figure 37); this measurement is shown in the upper-leftmost plot of Fig. 12 as a dashed black line. The PL lifetime measurement was only performed for QE A given the susceptibility of h-BN's QEs to disappear under pulsed excitation.

To fit these metadata, we consider the following empirical models:

Model I (Linear) :

$$R(P) = R_0 + m_0P \quad (5.3a)$$

Model II (First-Order Saturation) :

$$R(P) = R_0 + \frac{R_{sat}P}{P + P_{sat}} \quad (5.3b)$$

Model III (Second-Order Saturation) :

$$R(P) = R_0 + \frac{(m_0P_{sat}P + m_1P^2)}{P + P_{sat}} \quad (5.3c)$$

Model IV (Quadratic) :

$$R(P) = R_0 + m_0P + m_1P^2 \quad (5.3d)$$

where P is the excitation power and the other variables are free parameters representing zero-power offset, R_0 , low-power slope, m_0 , high power slope, m_1 , saturation value, R_{sat} , and saturation power, P_{sat} . Dotted curves in Fig. 12 show the best-fit results for the model listed in each panel; in each case, we select the model with the fewest free parameters that qualitatively fits the data. Best-fit parameters and uncertainties for each fit are reported in Appendix Tables 6 and 7.

The antibunching rate, γ_1 , exhibits a markedly nonlinear power dependence for QEs A, B, and C whereas the dependence appears to be linear for QEs D and E. However, we note that the power range in the data for QEs D and E might not be large enough for nonlinearities to emerge. For comparison, QEs B and C are excited with up to $\sim 4P_{sat}^\lambda$ whereas QE D is excited with up to $\sim 2P_{sat}^\lambda$ (see Table 3). The zero-power antibunching-rate offset (R_0) for QEs B-E is clearly non-zero, whereas the fits using Model II for QE A are poorly constrained, yielding $R_0 = 0 \pm 261$ MHz and $R_0 = 0 \pm 167$ MHz for green and orange excitation, respectively. The antibunching amplitudes (see Appendix Figure 35) for all QEs show a nonlinear saturation dependence on excitation power with an expected convergence to $C_1 \sim 1$ at zero excitation power.

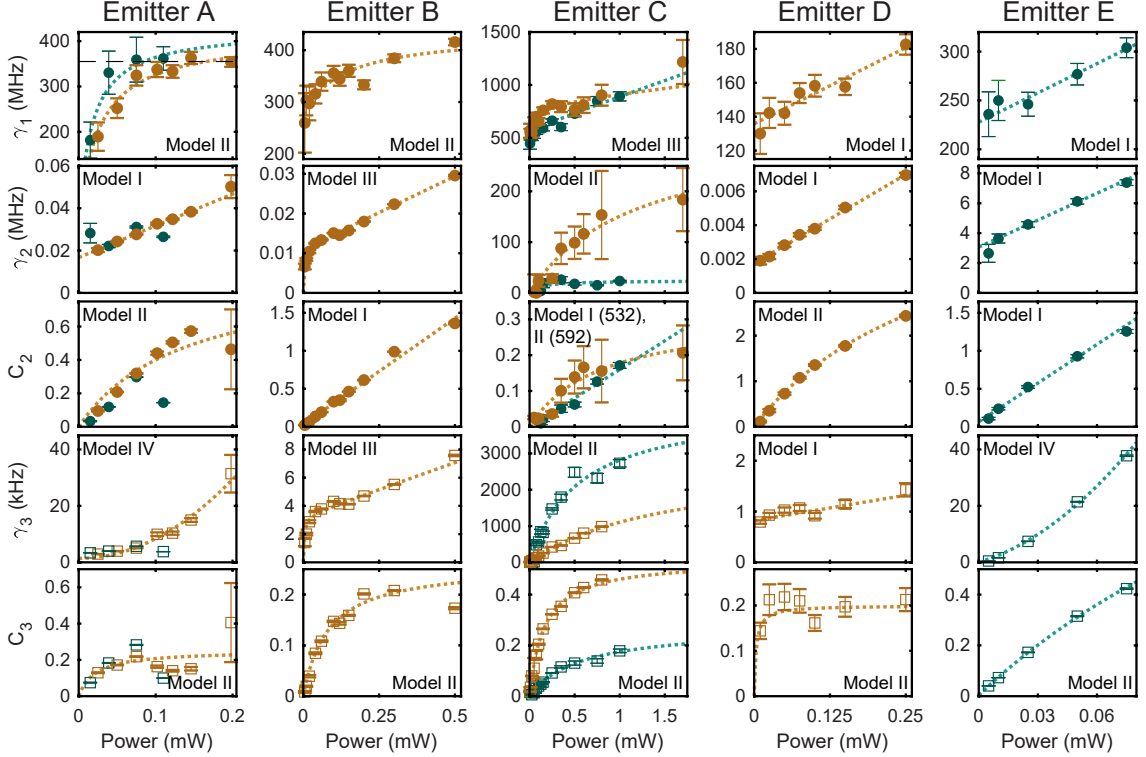


Figure 12: Photon Emission Correlation Spectroscopy. Excitation power and wavelength dependence of (Row 1) the antibunching rate (γ_1) denoted as circles, (Row 2) the bunching rate (γ_2) denoted as circles, (Row 3) the bunching amplitude (C_2) denoted as circles, (Row 4) the bunching rate (γ_3) denoted as squares and (Row 5) the bunching amplitude (C_3) denoted as squares, of the five QEs presented in each column. The black dashed line in the upper-leftmost plot (QE A) represents the lifetime. Orange (green) data correspond to excitation at 592 nm (532 nm). The error bars represent one standard deviation. The dotted lines are fits to the metadata as discussed in the text.

The bunching dynamics exhibit significant quantitative and qualitative variations across emitters. The fastest bunching rate, γ_2 , scales linearly with excitation power and has a non-zero offset for QEs A, D and E, whereas it exhibits saturation behavior and zero offset for QEs B and C. The magnitudes of γ_2 range from several kilohertz (QEs A, B, and D) up to several megahertz or faster (QEs C and E). The slower bunching rate, γ_3 , exhibits the largest qualitative variation across emitters, including linear (QE D), quadratic (QEs A and E), and saturation models (QEs B and C). Only QE D exhibits clear evidence for a non-zero offset for γ_3 . The magnitudes of γ_3 are typically in the kilohertz range, with the exception of QE C, whose γ_3 increases beyond 1 MHz at high powers. The bunching amplitudes primarily

depend nonlinearly on excitation power, except for C_2 of QEs B, C (green excitation) and E, which scale linearly with excitation power. All of the bunching-amplitude fits are consistent with zero offset, except for QE E, where small residual offsets ($R_0 < 0.1$) likely reflect minor systematic errors in the analysis or inaccuracies of the empirical models. For QE A, we restrict the meta-analysis of bunching parameters to the orange-excitation data, which extend to higher excitation power. However, we note that the green-excitation bunching parameters generally track the data for orange excitation.

5.5. Electronic Model and Optical Dynamics Simulations

We find that the key features observed in Fig. 12 can be understood using the four-level electronic model shown in Fig. 13(a). Figure 13 summarizes the results of optical dynamics simulations for this model. Given a set of transition rates for the model, we simulate $g^{(2)}(\tau)$ including the effects of timing resolution and shot noise (e.g., Fig. 13(b)), and we subsequently fit the simulated data using the empirical model of Eq. 4.7 with $n = 2$ to extract the antibunching and bunching parameters, as shown in Figs. 13(c)-(e). For reasons explained later in this section, the simulated data were best described by an $n = 2$ model despite having three eigenvalues.

The four-level model consists of a ground state (level 1), an excited radiative state (level 2), a higher-lying excited state (level 3) and a nonradiative metastable state (level 4). We consider two optical excitation pathways from the ground state to excited states 2 or 3, represented by the rates Γ_{12} and Γ_{13} , respectively. The magnitudes of these two rates depend on the corresponding optical cross-sections for absorption at the excitation wavelength. A difference in cross section can result from the difference in electric dipole matrix elements between the different electronic states, the atomic configuration coordinate overlap for vibronic transitions, or both of these factors. For the simulations in Fig. 13, we set $\Gamma_{12} = 0$, since we are particularly interested in the situation where $\Gamma_{12}/\Gamma_{13} \ll 1$, such that the dynamics feature indirect excitation of the radiative state 2 *via* nonradiative relaxation from excited state 3, at a rate κ_{32} . This was informed by the nonlinear power-scaling of γ_1 for QEs A, B and C. In the Appendix, we report simulations over a range of

settings where $\Gamma_{12}/\Gamma_{13} \in [0, 2]$, with qualitatively similar results (see Appendix Figure 39). In addition to the indirect excitation pathway formed by states 1, 2, and 3, optical excitation results in population and relaxation of metastable state 4 *via* nonradiative transitions with rates κ_{24} and κ_{41} . We consider two types of nonradiative transition mechanism for the metastable state: spontaneous and optically pumped. Spontaneous transition rates are independent of the optical excitation rate (in this case, Γ_{13}), whereas optically pumped transition rates scale linearly with Γ_{13} . In this model, the optically pumped transition rates κ_{24} and κ_{41} can approximate more complicated processes; for example, they could involve re-pumping from levels $2 \rightarrow 3$ or from levels $4 \rightarrow 3$ with subsequent nonradiative relaxation (see Appendix Figure 40), or they could involve transient population of additional levels. Their approximation as individual pumped transitions remains accurate as long as optical pumping remains the rate-limiting step. The key observable difference between spontaneous and optically pumped transitions manifests in the excitation power dependence of the corresponding bunching rate (Fig. 13(d)); the bunching rate for spontaneous transitions features a non-zero zero-power offset and saturates at high power, whereas the bunching rate for optically pumped transitions has zero offset and scales nearly linearly with power, even as the corresponding bunching amplitude (Fig. 13(e)) saturates.

For both bunching mechanisms, the simulated data were best described by only a single bunching level ($n = 2$ in Eq. 4.7) despite the fact that there should be 3 eigenvalues that describe this system. The reason for this is that the indirect excitation and emission process through levels 1, 2, and 3 can lead to two of the eigenvalues being complex. These eigenvalues have the largest real values and are responsible for the antibunching dynamics. When we include practical limitations on timing resolution and signal-to-noise ratio at short delay times, the fit cannot distinguish these two values, and the goodness-of-fit analysis prefers a single real rate that approximates the true model. The result is an effective antibunching rate that scales nonlinearly with increasing excitation rate. This effect persists even when a direct transition from state $1 \rightarrow 2$ is included. We performed simulations varying the ratio Γ_{12}/Γ_{13} , and observed qualitatively similar results (see Appendix Figure 39).

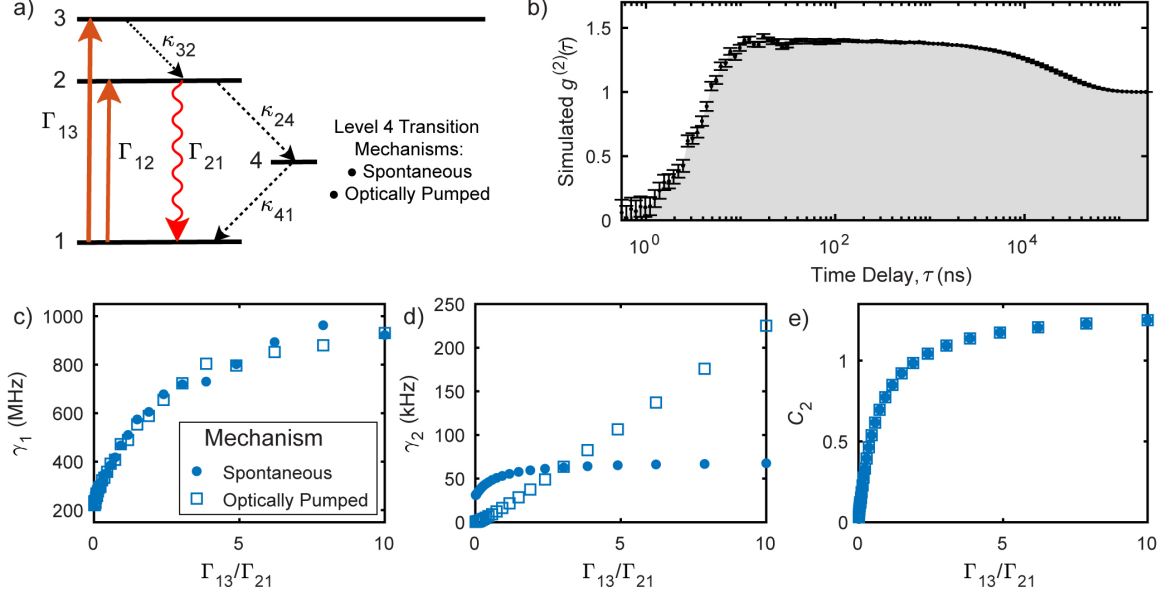


Figure 13: Electronic Level Structure and Optical Dynamics Simulations. (a) An investigative four-level electronic model consisting of the ground state (level 1), radiative state (level 2), excited state (level 3), and metastable state (level 4). Orange arrows represent excitation pathways (with rates Γ_{12} and Γ_{13}), the wavy red arrow represents radiative emission (with rate Γ_{21}), and dotted black arrows represent nonradiative transitions (with rates κ_{32} , κ_{24} and κ_{41}). (b) Simulated $g^{(2)}(\tau)$ for $\Gamma_{12} = 0$, $\Gamma_{13} = 84$ MHz, $\Gamma_{21} = 300$ MHz, $\kappa_{32} = 600$ MHz, $\kappa_{24} = 60$ kHz, and $\kappa_{41} = 30$ kHz. Error bars represent simulated photon shot noise. (c-e) Best-fit parameters γ_1 , γ_2 , and C_2 determined by fitting simulated $g^{(2)}(\tau)$ data using Eq. 4.7 with $n = 2$. The results are plotted as a function of Γ_{13}/Γ_{21} , where $\Gamma_{21} = 300$ MHz is a fixed parameter.

5.6. Interpreting the Photoluminescence, Spectral and Polarization Properties

Our experiments provide clear evidence that visible QEs in h-BN occur as isolated point defects with emission originating from a single, dominant optical transition. The QEs are spatially resolved in high signal-to-background μ -PL images. They exhibit PL saturation, high polarization visibility in emission, and emission spectra consistent with individual vibronic transitions. Most convincingly, several emitters exhibit pure single-photon emission, with $g^{(2)}(0) = 0$ within small experimental uncertainty, as shown in Fig. 11. This finding contrasts with previous suggestions that h-BN's QEs occur in pairs [27]. We do not contend, however, that such pairing cannot occur. On the contrary, in the course of our experiments we observed multiple instances of spatially isolated emitters with high polarization visibility,

and yet $g^{(2)}(0)$ is substantially larger than zero. We have focused here on emitters showing the highest likelihood of being single defects.

Qualitatively, the QEs' room-temperature PL spectra are similar to those reported elsewhere in the literature [65, 103, 104, 185]. The analysis shown in Fig. 9 indicates that the PL spectra are consistent with individual vibronic transitions between two optical-dipole-coupled electronic states. The one-phonon lineshapes for QEs A, B, C, and E are all qualitatively similar despite the fact that QEs A and B feature ZPL energies near 1.9 eV, compared to 2.1 eV for QEs C and E. All four emitters exhibit strong coupling to low-energy phonons ($\lesssim 50$ meV) as well as to higher-energy phonons (150-200 meV) that are typically associated with longitudinal optical modes in bulk h-BN [137]. Coupling to low-energy phonons is a key feature in determining the asymmetric shape of the dominant emission peak [103, 212]. The ZPL corresponds to the transition from the lowest vibrational level of the initial (excited) state to the lowest vibrational level of the final (ground) state. When low-energy phonons are involved, transitions can occur from the lowest vibrational level of the initial state to the first vibrational level of the final state, showing up on the low-energy side of the ZPL and leading to the asymmetric shape. Failure to account for low-energy phonons in interpreting experimental spectra leads to an underestimation of the Huang-Rhys factor, S_{HR} , which quantifies the strength of the vibronic coupling and is a crucial parameter for comparing with theoretical calculations. Our model captures the asymmetric spectral shape. However, the precise details of the low-energy phonon-coupling lineshape become correlated with the ZPL width (assumed to be Lorentzian) and S_{HR} when fitting the model to experimental data. We account for these correlations by performing the fits using varied constraints on the low-energy phonon coupling motivated by scaling considerations. We follow the method described in Ref. [65], in order to estimate uncertainties on S_{HR} and the ZPL linewidth. Overall, we find that the best-fit ZPL linewidths are narrower or comparable to those reported in the literature for off-resonant excitation of h-BN's QEs at room temperature [6, 54, 55], and the values of S_{HR} are somewhat higher. We consider comparisons to theoretical proposals in detail later; we note here that the ZPL energies and S_{HR} values

closely match the calculated properties of boron dangling bonds [197, 200].

The QE's polarization-resolved PL excitation and emission characteristics (Fig. 8) begin to reveal more complicated features of their optical dynamics. Both QEs A and C exhibit linearly polarized emission with nearly complete visibility, again consistent with emission through a single optical dipole transition. For QE A, the PL intensity varies as a function of excitation polarization angle in a manner consistent with excitation through a single optical dipole, with high visibility and an angle aligned with the emission dipole, independent of excitation wavelength (532 nm or 592 nm). In the case of QE C, the emission polarization visibility and dipole angle is similarly independent of the excitation wavelength. However, QE C's excitation polarization dependence varies dramatically as a function of excitation wavelength; the excitation dipole is aligned with the emission under 592 nm excitation, but misaligned under 532 nm excitation with substantially reduced visibility. Emission polarization data are not available for QEs B, D, and E, but the excitation polarization measurements are qualitatively similar to those for QEs A and C. All three QEs show polarized absorption with varying degrees of visibility.

The heterogeneous polarization responses are consistent with previous observations for QEs in h-BN [65, 103, 104, 227]. In particular, Ref. [104] studied the variation of polarization visibility and alignment between excitation and emission as a function of the energy difference between the excitation photon energy and the ZPL photon energy, ΔE . They observed that the excitation and emission dipoles are aligned ($\Delta\theta = 0$) when $\Delta E \lesssim 200$ meV, whereas if $\Delta E \gtrsim 200$ meV, $\Delta\theta$ can take any value. Our observations are consistent with this empirical finding. For QE A, the excitation and emission angles are aligned despite relatively large energy differences, $\Delta E^{592} = 169$ meV and $\Delta E^{532} = 405$ meV, for 592 nm and 532 nm excitation, respectively. For QE C, the dipoles are aligned for excitation at 592 nm ($\Delta E^{592} = 10$ meV; $\Delta\theta^{592} = 0.0 \pm 1.4^\circ$) but misaligned at 532 nm ($\Delta E^{532} = 247$ meV; $\Delta\theta^{532} = 46.5 \pm 1.6^\circ$).

Misalignment between absorption and emission dipoles is expected if the optical dynam-

ics involve multiple excited states. Whereas the invariance of the PL polarization, visibility, and spectral shape to excitation energy implies that PL emission occurs through a single optical transition, off-resonant optical pumping can involve transient excitation of higher-lying excited states through transitions with different optical dipole orientations, which subsequently relax to the radiative state as shown in Fig. 13(a). Depending on energy level arrangement and the vibronic coupling strengths, a single excitation laser can drive both transitions between states $1 \rightarrow 2$ and $1 \rightarrow 3$. The excitation polarization dependence will then reflect a superposition of two optical dipole transitions, with an orientation and visibility determined by the underlying dipole transition orientations and their relative optical cross section. To test this hypothesis, we performed a simultaneous fit of QE C's emission and excitation polarization data under 532 nm excitation assuming a single shared dipole for excitation and emission *via* states $1 \leftrightarrow 2$ together with a second dipole for excitation *via* $1 \rightarrow 3$ (Fig. 10). We find that the data are consistent with such a model, in which the dipole projection for transition $1 \rightarrow 3$ is misaligned from that of transition $1 \leftrightarrow 2$ by $63 \pm 1^\circ$, and the ratio of excitation cross sections is $\Gamma_{12}/\Gamma_{13} \sim 0.5$.

In interpreting these results, we note that the observation of highly polarized emission implies the presence of at least one symmetry axis for the underlying electronic states. For most defect models under consideration, symmetry allows for optical dipole transitions aligned perpendicular to the h-BN plane (along z) or within the plane either parallel or perpendicular to the defect's symmetry axis (along x or y). Hence, the observation of dipoles misaligned by $\sim 60^\circ$ seems surprising. However, since our polarization-resolved experiments are primarily sensitive to the projection of the dipole perpendicular to the microscope's optical axis, it is possible that sample misalignment or local distortions of the defect that tend to tilt the z axis could explain the observations. Alternatively, our model of two superposed excitation dipoles might not capture all salient features of the excitation process; more than two transitions might be involved, and yet the superposition of any number of dipole absorption patterns will ultimately yield a polarization dependence consistent with Eq. 4.2.

5.7. Interpreting the Optical Dynamics

PECS experiments reveal key details regarding the nature of the QEs' excited states and optical dynamics. The PECS results summarized in Fig. 12 resolve individual dynamical processes, their associated timescales, and their dependence on optical excitation power. All QEs feature three or more timescales in their autocorrelation spectra, which implies that the optical dynamics involve at least four electronic levels. In addition to antibunching on nanosecond timescales, all QEs exhibit bunching with two or more resolvable timescales that are orders of magnitude longer (typically microseconds to milliseconds). These bunching timescales are broadly consistent with past observations [26, 40, 65, 137, 181, 184], and they indicate the role of metastable dark states in the optical dynamics. Here, we emphasize and discuss two key features of the PECS measurements in Fig. 12: the nonlinear power dependence of the antibunching rate, γ_1 , that is clearly observed for QEs A, B, and C; and the heterogeneous behavior of the bunching rates and amplitudes, which feature qualitatively diverse power-dependent variations.

For a QE featuring a direct optical transition between a ground state and a radiative excited state, the antibunching rate scales linearly as a function of optical excitation power, with a zero-power offset corresponding to the QE's spontaneous emission rate. This is the case even for QEs that also feature metastable charge and spin states, such as the nitrogen-vacancy (NV) center in diamond [57]. In Appendix Figure 34, we present measurements of the antibunching rate of single NV centers in nanodiamonds as a function of excitation power; the results show clear linear scaling and a zero-power offset for γ_1 consistent with the expected optical lifetime. The PECS observations of h-BN's QEs in Fig. 12 defy this expectation. The power-scaling of γ_1 for QEs A, B, and C is clearly sublinear, with a saturation behavior (Model II or Model III) characterized by a steep slope at low power tapering off to a shallow slope at high power. Moreover, the γ_1 measurements for QE A are all less or equal to the measured spontaneous decay rate (dashed line in the upper-left panel of Fig. 12), whereas γ_1 always exceeds the spontaneous rate for a direct optical transition. The zero-power offset for γ_1 in QEs A and B is consistent with zero but poorly constrained

due to the steep low-power slope; the offset is non-zero for QEs C, D, and E. QEs D and E exhibit linear power-scaling of γ_1 , however the range of available powers is smaller than for the other emitters, and we cannot rule out a saturation behavior at higher power. Previous studies of QEs in h-BN have revealed hints of power-independent antibunching rates [181] and nonlinear power scaling [26, 40], however these observations were never satisfactorily explained.

The antibunching rate's nonlinear power dependence can be understood in the context of an indirect excitation mechanism, as illustrated in Fig. 13(a), where optical excitation leads to the population of multiple states: levels 2 and 3, with competing rates Γ_{12} and Γ_{13} . Indirect population of the radiative state (level 2) through such a mechanism creates a rate-limiting step ($3 \rightarrow 2$) to the optical emission pathway ($2 \rightarrow 1$) that leads to nonlinear scaling of the observed antibunching rate, as shown in Fig. 13(c). The rate-limiting nature of this process is intuitively obvious in the limit where $\Gamma_{12}/\Gamma_{13} \ll 1$. However, we find that the nonlinear saturation behavior remains qualitatively consistent independent of the pumping-rate ratio across a wide range of simulation settings where $\Gamma_{12}/\Gamma_{13} \in [0, 2]$ (see Appendix Figure 39). In the regime $\Gamma_{12}/\Gamma_{13} \ll 1$, the population of level 2 is still mostly determined by the indirect excitation pathway through level 3, with rate κ_{32} , and the dominant antibunching rate saturates to a value close to $\kappa_{32} + \Gamma_{21}$. In the regime where $\Gamma_{12}/\Gamma_{13} > 1$, two underlying rates in the dynamical system are associated with the antibunching dip. As discussed previously, the eigenvalues associated with these rates can be real or complex depending on the relative magnitudes of transitions in the system. However, the fast rate associated with the direct population of level 2 and the subtle signatures of complex eigenvalues on the shape of the antibunching dip turn out not to be detectable when we include realistic assumptions for the experimental limits on timing resolution and shot noise. Instead, we observe a single effective antibunching rate γ_1 that exhibits nonlinear saturation similar to the slow rate.

The bunching dynamics observed in Fig. 12 can also be understood within our optical

dynamics models by including metastable shelving states. In Fig. 13, the key qualitative difference between spontaneous population of the metastable state(s) (*e.g.*, spin-dependent intersystem crossings) and optically pumped transitions (*e.g.*, ionization/recombination) appears in the power-scaling and zero-power offset of the associated bunching rate. Spontaneous transitions are characterized by a rate with a non-zero offset that tends to saturate with increasing pumping power, whereas optically pumped transitions have zero offset and increase quasi-linearly. Previous studies considering the power-scaling of bunching rates for QEs in h-BN nano-flakes and exfoliated flakes have proposed similar optically-pumped models [26, 40]. Similar behavior has also been observed in color centers such as the silicon-vacancy center in diamond, attributed to power-dependent de-shelving from higher lying states to the metastable state [150]. However, the heterogeneity and complexity of these processes for QEs in h-BN, both regarding the number of levels and the type of transitions, have not been considered before.

We observe both qualitative bunching behaviors in the data of Fig. 12, with several QEs exhibiting multiple bunching levels that apparently have different transition mechanisms. In some cases, individual bunching rates exhibit power scalings with features of both phenomena; for example, γ_2 for QEs A, B, D, and E appears to have a non-zero offset and yet increase linearly with power. This could indicate that the associated state can be populated both spontaneously and through an optically pumped pathway. Our simulations support this intuitive reasoning. For example, Appendix Figure 38 shows the results of simulations of the same four-level system as in Fig. 13(a), but with rates chosen to reproduce the observations for QE A from Fig. 12. We indeed find that a combination of spontaneous and optically pumped transitions to the metastable state (κ_{24} and κ_{41}) yields a bunching rate γ_2 with a non-zero offset that scales linearly with pumping power. Moreover, setting $\kappa_{32} < \Gamma_{21}$ creates a situation where the spontaneous emission rate exceeds the observed antibunching rate, $\Gamma_{21} > \gamma_1$, over a wide range of pumping power, in agreement with our observations. The quantitative magnitudes of γ_1 , γ_2 , and the bunching amplitude, C_2 , are also reproduced by the simulations. This highlights the versatility of optical dynamics simulations as

a valuable tool to recreate or predict optical dynamics based on complex combinations of radiative and nonradiative processes. To fully capture the observed dynamics of any particular QE, including the additional bunching rates γ_3 and γ_4 (where applicable), more metastable states are required in the simulations. We further note that the number of observed bunching timescales represents a lower limit on the number of metastable states, and hence some states could actually represent multiplets associated with different spin manifolds. Even with those caveats, these observations present the opportunity for quantitative comparisons with theoretical predictions.

5.8. Consistency with Theoretical Defect Proposals

Several defect structures have been proposed as the origin of visible-wavelength single-photon emission in h-BN, including the boron dangling bond (DB) [197], $V_N N_B$ [193], $V_N C_B$ [169], and $V_B C_N$ [140]. The negatively-charged boron vacancy, V_B^- , has been suggested to give rise to an ODMR signal observed for emitter ensembles [83], however V_B^- has a ZPL of ~ 1.7 eV and couples more strongly to phonons ($S_{HR} \sim 3.5$) [99], producing a PL band between 800-900 nm that does not overlap with the emitters considered here. Early studies highlighted $V_N N_B$ as the potential origin of visible QEs [193], but recent calculations show that the coupling to phonons is substantially larger than observations [169]. More recently, $V_B C_N$ has been proposed based on the observation that carbon is correlated with the emission signal, but the calculated PL spectrum [140] does not match our observations. The $V_B C_N$ calculations also predict a single, linearly-polarized absorption dipole, which is inconsistent with our measurements. The calculated PL spectrum and strain dependence of $V_N C_B$ [169] are in reasonable agreement with the our observations. However, the optical transition for $V_N C_B$ occurs in the triplet channel, while the calculated ground state is a singlet; the authors did not propose a mechanism through which the triplet channel is populated quickly enough to give rise to the optical emission they considered.

The boron DB is predicted to possess an optical transition at 2.06 eV with a Huang-Rhys factor of 2.3 [197], which is in close agreement with the values observed in this study. In addition, the variations in ZPL and S_{HR} for the observed emitters can be explained by

out-of-plane distortions [200]. There are various ways in which an out-of-plane distortion could occur: extended defects, the natural asymmetry from a flake edge being unsupported on one side, interlayer bonding, local lattice relaxations in voids, etc. Such microscopic features are difficult to distinguish optically, however we note that QEs often occur near extended defects (this is the case, e.g., for QE B). The ground state of the boron DB is a singlet, and the predicted existence of a triplet excited state can explain the presence of level 4 in Fig. 13(a). Another important feature of the boron DB model is the proximity of the states to h-BN’s conduction band [197]; this allows electrons to be optically excited directly into the conduction band, depending on the excitation energy, explaining the misalignment of the absorptive and emissive dipole when the excitation energy is increased. Other proposed models do not provide an explanation for the misalignment. For instance, in the case of $V_N C_B$ the optical transition occurs in the neutral charge state, and for the excitation energies considered here, photoionization will not occur [216].

Within the boron DB model, we would interpret level 3 in Fig. 13(a) as the conduction band and κ_{32} as the nonradiative capture rate. To support this interpretation, we have estimated the relevant capture rate κ_{32} of a photoionized electron from the conduction-band minimum into the DB excited state [level 2 in Fig. 13(a)]. This capture rate is a product of a capture coefficient and the density of electrons in the conduction band. A first-principles calculation yields a capture coefficient of $4 \times 10^{-7} \text{ cm}^3 \text{ s}^{-1}$ (see Appendix E). The density of electrons is estimated based on the thermal velocity of the photoionized electron ($\sim 10^5 \text{ m s}^{-1}$) and a typical electron energy relaxation time of $\sim 1 \text{ ps}$ [222]. In the time it takes the electron to relax to the conduction-band minimum, it can thus travel $\sim 100 \text{ nm}$; this distance corresponds to an effective electron density of $2.4 \times 10^{14} \text{ cm}^{-3}$. Multiplying this value with the calculated capture coefficient gives a rate of $\kappa_{32} \sim 100 \text{ MHz}$, in compelling agreement with the observed saturation antibunching rates of $\gamma_1 \sim 300\text{-}800 \text{ MHz}$ for QEs A, B, and C. Nonradiative transition rates can vary by more than 10 orders of magnitude for reasonable defect parameters [187]. Our calculations also show that capture into the excited state is favored over capture into the ground state by more than 5 orders of magnitude,

justifying the neglect of κ_{31} in the general model of Fig. 13(a).

The inclusion of photoionization allows us to further rationalize the heterogeneity in bunching behavior of the observed emitters: the photoionized electron is not necessarily re-captured at the same QE, but may instead be captured by a neighboring defect, leaving the QE in a nonfluorescent, ionized configuration that likely requires optical excitation of additional free electrons to restore emission *via* subsequent electron capture. This process would be represented in Fig. 13(a) by an optically pumped transition, where level 4 represents an ionized state of the QE. The emitters may therefore be highly sensitive to the local defect environment. Unlike other proposed defect models, we conclude that the boron DB model is thus capable of explaining numerous aspects of the experimental observations, lending support to this proposed microscopic structure.

5.9. Conclusion

The observations discussed in this chapter reveal that h-BN's QEs have intricate electronic level structures and complex optical dynamics including multiple charge or spin manifolds. Our proposed electronic-structure models complement previous reports [26, 40, 181] and explain the quantitative features of our observations. In particular, the models explain the observation of nonlinear power-scaling of the antibunching rate as well as heterogeneous magnitudes and power-scaling behavior of multiple bunching rates. Whereas past reports have lacked consensus on mechanisms to explain the observed optical dynamics of h-BN's QEs, and many posited chemical and electronic structure models have failed to adequately explain the heterogeneous observations, we show that the boron dangling bond model is remarkably consistent with experiments, especially accounting for the role of local distortions, photoionization, electron capture, and the QEs' heterogeneous local defect environment. Future experiments should be designed to investigate these details, for example time-domain studies of transients associated with charge and spin dynamics, and temperature- and excitation-energy-dependent variations of the PL lineshape, vibronic spectrum, and polarization-dependent excitation cross section. Combined with theoretical models, such experiments can resolve the underlying transition rates and resolve the dis-

parate influences of the QEs' intrinsic properties with those of their local environments. The observation of pure single-photon emission with $g^{(2)}(0) = 0$ resolves earlier questions about h-BN's QEs [27], affirming their potential for use in photonic quantum technologies. More generally, we hope that the approach and techniques presented in this work—especially the quantitative use of PECS—present a model to formulate optical dynamics models for QEs in any material platform [20, 70]. Our models can be adapted to account for recent observations of magnetic-field-dependent optical dynamics [66] and ODMR [39, 184] in h-BN. Subsequently, they can be used to design protocols for initialization, control, and readout of quantum-coherent spin states for quantum information processing and quantum sensing.

CHAPTER 6 : Spin Dynamics of Quantum Emitters

This chapter discusses searching and probing single spins in h-BN. It details the results and discussion and is organized as follows: Section 6.1 introduces the current understanding of spins in h-BN and this work; Section 6.2 discusses searching for single spins using magnetic-field-dependent PECS; Section 6.3 details verifying the single spin using ODMR and discusses probing the single spin's ZFS and g-factor anisotropy; Section 6.4 discusses the time-domain and spin dynamics of the single spin probed using optical and microwave pulse protocols; and Section 6.5 concludes the chapter.

This chapter has been adapted with permission from a manuscript in preparation by Patel et al.³ The sample preparation was done in close collaboration with Benjamin Porat. The experimental methods of this chapter were completed in a close collaboration with Dr. Tzu-Yung Huang, Dr. David A. Hopper, Rebecca E. K. Fishman, Jordan A. Gusdorff and S. Alex Breitweiser. This work was primarily supported by the National Science Foundation (NSF) award DMR-1922278. The use of facilities and instrumentation in the Singh Center for Nanotechnology at the University of Pennsylvania was supported by NSF through the National Nanotechnology Coordinated Infrastructure (NNCI; Grant ECCS-1542153) and the University of Pennsylvania Materials Research Science and Engineering Center (MRSEC; DMR-1720530). We gratefully acknowledge fruitful discussions with M. Turiansky, C. G. Van de Walle and M. Flatté.

6.1. Introduction

Optically interfaced solid-state spins have been demonstrated for a variety of quantum technologies [4, 17]. They enable quantum technologies with unprecedented capabilities such as sensing [3, 12, 25, 51], communication or memories [29] and enable studying light-matter interaction and spin-photon entanglement [89]. A variety of solid-state spin host materials are available [4, 17, 20, 105, 214] and new ones continue to be explored in search of the perfect host material. Hexagonal boron nitride (h-BN), a wide bandgap material home

³This manuscript was in preparation at the time of writing this thesis.

to numerous optical defects is a promising host material for its room temperature stability and low dimensionality that promises unique capabilities compared to bulk materials. The optical defects in h-BN have shown single-photon emission with noise-limited photon antibunching, $g^{(2)}(0) = 0$ [155]. The recent observations of magnetic-field-dependent photoluminescence and optically detected magnetic resonance (ODMR) make the optical defects in h-BN prospective candidates for optically addressable solid-state spins [39, 66, 83, 184].

ODMR has been recently observed across heterogeneous emitters in h-BN at cryogenic and room temperatures having weak but finite zero-field splitting (ZFS) and isotropic g -factor [39, 184]. However, ODMR of a pure single-photon emitter (SPE) in h-BN is yet to be observed. Further, the origin of weak ZFS across heterogeneous emitters and an isotropic g -factor remains unanswered and the nature of spin defects remain unknown. In this work, we confirm spin resonance of a pure SPE at room temperature. We probe the steady-state magnetic field dependence of the SPE using photon emission correlation spectroscopy (PECS) to confirm the presence of magnetic-field-dependent transitions [70]. We study single-spin resonance using continuous-wave (cw) and pulsed ODMR. We observe an inhomogeneously broadened resonance spectrum without a resolvable hyperfine structure using pulsed ODMR. Within the experimental uncertainty, we find that the single spin has no ZFS. It has an isotropic g -factor of ~ 2 , consistent with the free electron g_e -factor of 2.0023 and with recent observations [39, 184]. Based on the absence of ZFS and g -factor ~ 2 , we postulate a doublet ($S = \frac{1}{2}$) spin state. We achieve an improved contrast of up to $\sim 8\%$ using cw ODMR and over $\sim 20\%$ using pulsed ODMR. We probe time-domain and spin dynamics using optical and microwave pulse protocols to improve the resonance contrast, optimize optical spin contrast by maximizing signal-to-noise ratio and understand pulse protocols crucial to developing methods to coherently control the single spin. We find the single spin to be extremely stable in ambient conditions with optical pumping up to 500 μW and microwave pulses with RF power up to 4 W for over hundreds of hours. A stable single spin in h-BN makes it attractive for room temperature spin-based quantum technologies.

6.2. Searching for Single Spin

We first perform photoluminescence (PL) spectroscopy and PECS to search for single spins and characterize its steady-state optical and magnetic-field-dependent temporal dynamics [70, 155]. In this letter, we discuss one single-spin found in an area of $25 \times 25 \mu\text{m}^2$ amongst over 20 nonmagnetic emitters, suggesting $\sim 5\%$ yield of paramagnetic emitters consistent with a recent report [184]. We used a custom-built confocal microscope to study the single spin in h-BN under ambient conditions. The sample consisted of mechanically exfoliated thin h-BN flakes suspended on patterned SiO_2/Si substrate [65, 155]. The substrate is mounted on a microwave chip connected to a signal generator to generate on-chip AC magnetic field by sending microwaves through a aluminum wire passing over the h-BN flake under study (Fig. 6).

The emitters are illuminated with either of two cw lasers operating at 532 nm and 592 nm wavelengths, where excitation power and polarization are controlled. The data recorded under 592 nm (532 nm) excitation are plotted in orange (green) in the relevant figures. All PECS, ODMR, time-domain and spin dynamics measurements were performed under 592 nm illumination. We acquire large area μ -PL images of the h-BN flake to locate spatially isolated emitters. We first characterize the optical excitation and emission properties. We acquire PL emission spectra and find zero-phonon line (ZPL) ~ 600 nm for all SPEs – para- and nonmagnetic. Figure 14(a) shows PL emission spectra of the single spin. We acquire the excitation and emission polarization to determine the degree of polarization and optical dipole alignment. We find the optical dipoles to be highly polarized (visibility reaching 100%) and aligned for both 532 nm and 592 nm excitation (Fig. 14(b)) in both the excitation and emission polarization. These observations are distinct from the heterogeneous polarization responses in previous observations of h-BN emitters [65, 103, 104, 155, 227]. Aligned excitation and emission dipoles are expected for optical transitions involving same excited states for varying excitation energies. We control full 360° rotation of the optical excitation dipole (referred hereafter as dipole) by controlling orientation of the sample mounted on a rotation stage. We next confirm the single-photon emission by calculating the second-order

photon autocorrelation function, $g^{(2)}(\tau)$ at zero-delay ($\tau = 0$) using an empirical function

$$g^{(2)}(\tau) = 1 - C_1 e^{-\gamma_1|\tau|} + C_2 e^{-\gamma_2|\tau|} + C_3 e^{-\gamma_3|\tau|} \quad (6.1)$$

where τ is the delay time, γ_1 is the antibunching rate and C_1 is the associated antibunching amplitude, γ_2 and γ_3 are the bunching rates and C_2 and C_3 are the associated bunching amplitudes. We determined the best-fit empirical function to be a three-timescale $g^{(2)}(\tau)$ consisting of an antibunching rate and two bunching rates using Akaike information criterion and reduced chi-squared statistic [155]. We find single-photon emission with noise-limited photon antibunching, $g^{(2)}(0) = 0$ at various optical powers and in-plane applied magnetic fields (Fig. 14(c)).

We next characterize the temporal dynamics to verify magnetic-field-dependent transitions – a signature of presence of spin. The internal dynamics of a SPE are dependent on the electronic level structure that is sensitive to external fields such as magnetic or electric fields. In the presence of a spin, an applied magnetic field would affect the optical dynamics due to the spin-selective transition rates [57, 66, 70]. The magnetic-field-dependent optical dynamics can be probed via a change in the temporal dynamics of photon correlations ($g^{(2)}(\tau)$) due to an applied magnetic field. The presence of spin would result in the change in bunching rates and associated amplitudes that result from the inter-system crossing involving the spin-selective transitions. We determine the temporal dynamics by calculating $g^{(2)}(\tau)$ using the empirical function in Eq. 6.1 at various magnetic fields. We apply a magnetic field parallel to the sample and thus to the h-BN with an assumption of it lying flat on the substrate. We perform the measurement at various dipole orientations. Figure 14(d)-(h) shows the change in steady-state PL and $g^{(2)}(\tau)$ parameters due to an in-plane magnetic field for dipole orientation of 0° (resulting in parallel applied field) and 15° at 250 μW optical power.

We find a significant change in steady-state PL of over 16% on increasing the magnetic field strength from 0 G to 470 G (Fig. 14(d)). The modulation of steady-state PL has

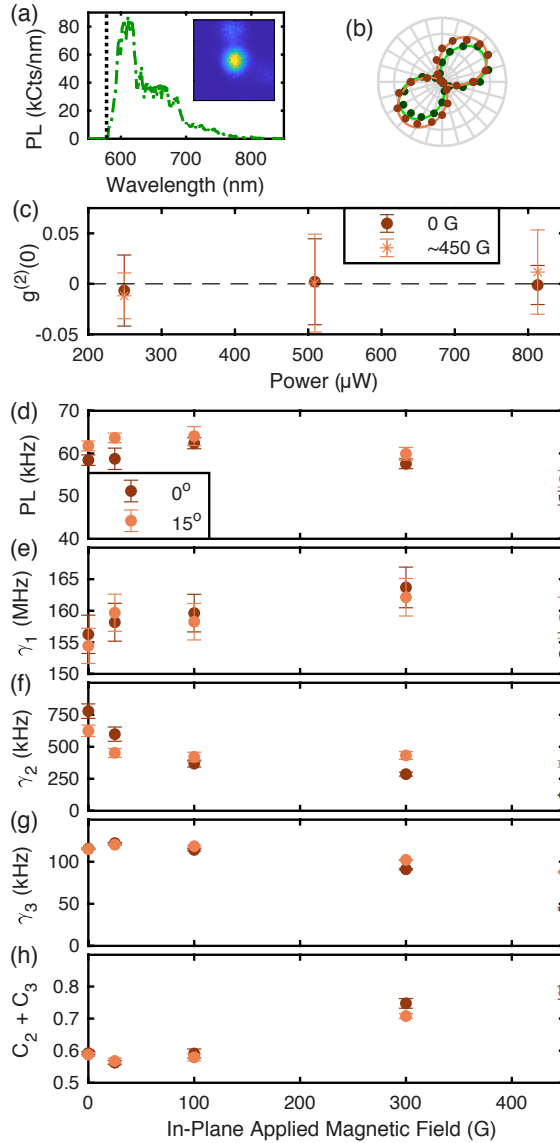


Figure 14: Optical and Temporal Characterization. In all panels, data plotted in orange (green) were acquired under 592 nm (532 nm) excitation. All error bars represent one standard deviation. (a) PL emission spectra with black dotted line representing cut-on wavelength of long-pass optical filter in the collection path. Inset: μ -PL image ($2 \times 2 \mu\text{m}^2$) of the single spin. (b) PL intensity as a function of linear excitation polarization angle for 532 nm (green circles) and 592 nm (orange circles) excitation. Solid curves are fits to the data. (c) Photon autocorrelation function at zero-delay as a function of optical power for two different in-plane magnetic fields for 0° dipole orientation. (d)-(h) Result of PECS measurements as a function of an in-plane magnetic field for 0° and 15° dipole orientation. (d) The time-average PL emission rate, (e) antibunching rate γ_1 , (f) bunching rate γ_2 , (g) bunching rate γ_3 and (h) total bunching amplitude $C_2 + C_3$.

been reported in past for h-BN emitters [66] and well understood for the nitrogen-vacancy center in diamond [64]. The antibunching rate, γ_1 stays similar on varying the magnetic field strength, with the average $\gamma_1 = 158$ MHz for both orientations (Fig. 14(e)). This is expected since γ_1 results from the photon emission on relaxation from the excited to the ground state unlike the nonradiative transitions involving inter-system crossing which are typically spin-selective. The bunching rates, γ_2 and γ_3 vary by more than $5\times$ with the magnetic field strength, albeit to different extents for different dipole orientations (Fig. 14(f)-(g)). The total bunching amplitude, $C_2 + C_3$ increases by over 30% on increasing the magnetic field strength from 0 G to 470 G. These observations confirm the magnetic-field-dependent transitions indicating presence of spin in the SPE at room temperature. Further, this framework can be used to confirm presence of single spins in any solid-state host material before performing spin resonance measurements that involve several tunable parameters that can mask the spin signal outside the optimum parameter space.

Figures 15-17 presents the data acquired at various optical powers and dipole orientations for an applied magnetic field relative to no magnetic field. At different dipole orientations for no magnetic field and an in-plane magnetic field, we perform PECS as a function of optical power. For 0° and 90° dipole orientation, ~ 450 G magnetic field is applied whereas for rest of the dipole orientations 300 G magnetic field is applied. From the optical-power-dependent PECS, % change in PL, antibunching rate and total bunching is calculated between an applied vs no magnetic field as presented in Fig. 15. Applying a magnetic field reduces the PL and increases the total bunching while keeping the antibunching rate mostly constant as expected. Albeit the % change reduces with increasing optical power likely from the saturation of state populations due increased optical pumping rate. While there is dipole dependent change, the trend is unclear. It should be noted that at each dipole orientation the magnetic field is either 300 G (for 40° , 70° , 100° and 130°) or ~ 450 G (for 0° and 90°), the effective magnetic field varies due to rotation of the sample that moves the SPE toward or away from the magnet. For the data presented in Fig. 15-17, this variation isn't accounted for. Figure 16-17 presents absolute PL and total bunching as

a function of optical power, at dipole orientation and magnetic fields corresponding to data in Fig. 15.

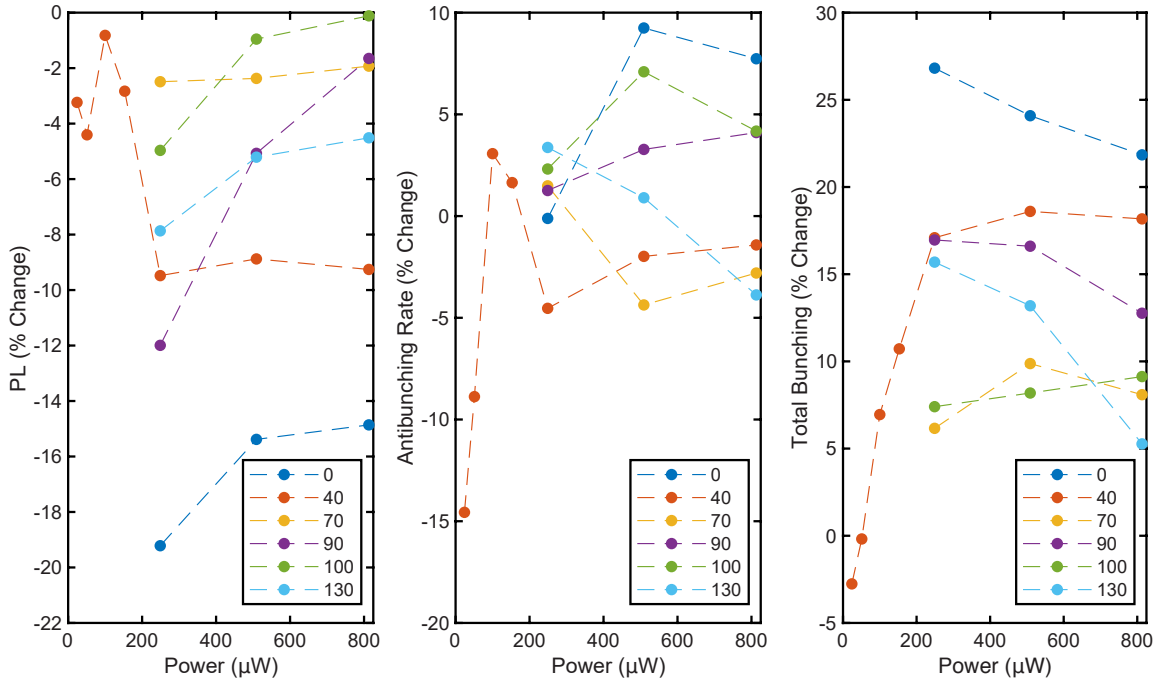


Figure 15: Magnetic-Field-Dependent PECS at various Dipole Orientations. Change in photoluminescence (PL), antibunching rate and total bunching as a function of optical power on applying a magnetic field relative to zero magnetic field.

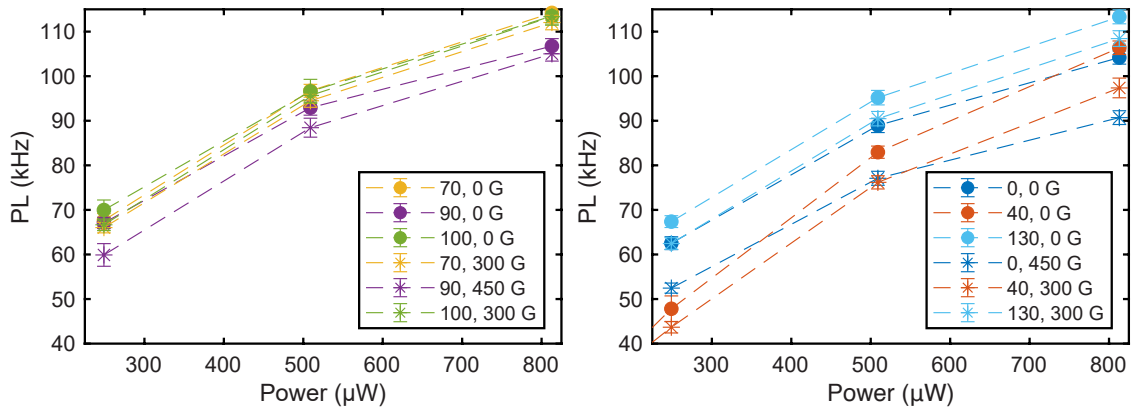


Figure 16: Photoluminescence at various Dipole Orientations. PL as a function of optical power obtained from PECS measurements. All error bars represent one standard deviation.

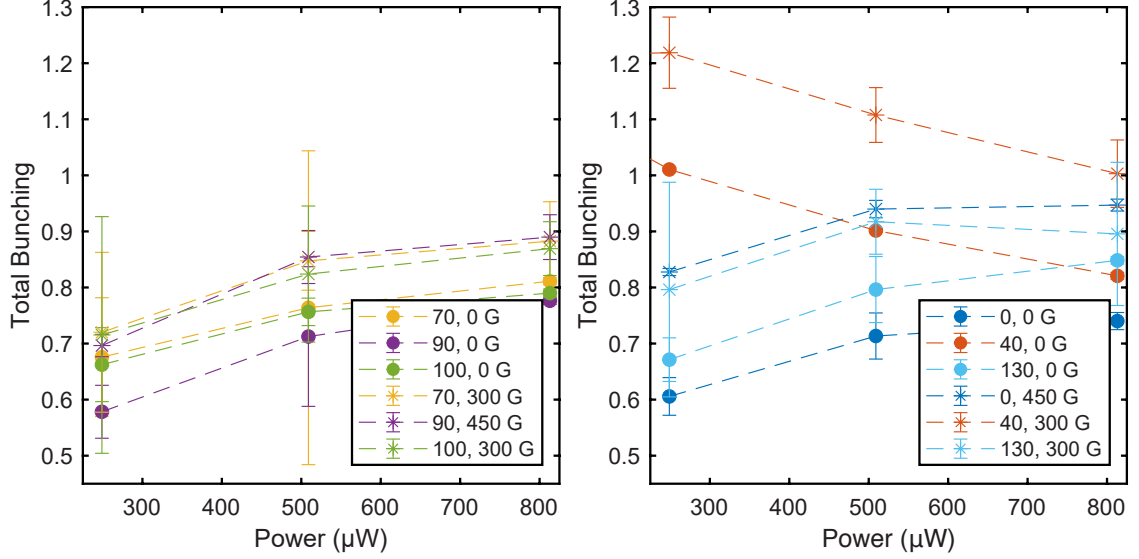


Figure 17: Total Bunching at various Dipole Orientations. Total bunching as a function of optical power obtained from PECS measurements. All error bars represent one standard deviation.

6.3. Single-Spin Resonance, Zero-Field Splitting and g-factor Anisotropy

We next embark on confirming single spin by performing a cw ODMR measurement (Fig. 18(a)).

At an in-plane applied magnetic field, we sweep amplified microwave frequencies using a signal generator. An arbitrary waveform generator controls optical and microwave pulses.

Figure 18(b) shows an inhomogeneously broadened cw ODMR spectrum acquired under 200 μW optical power, 0.5 W input microwave power and a magnetic field of 470 G applied parallel to the optical dipole (0° orientation). At 50% duty cycle, the microwave pulse duration is 40 μs . We measure the resonance frequency of 1315.9 ± 1.6 MHz with 6.3% contrast on fitting a Lorentzian function to the data acquired by normalizing the signal PL by reference PL recorded in the measurement. The Lorentzian function used is

$$C(f) = A + \frac{B}{(f - f_o)^2 + \Gamma^2} \quad (6.2)$$

where f is the microwave frequency, A and B are constants, f_o is the central or resonance frequency and Γ is the full width at half maximum (FWHM) or linewidth. Our measurements

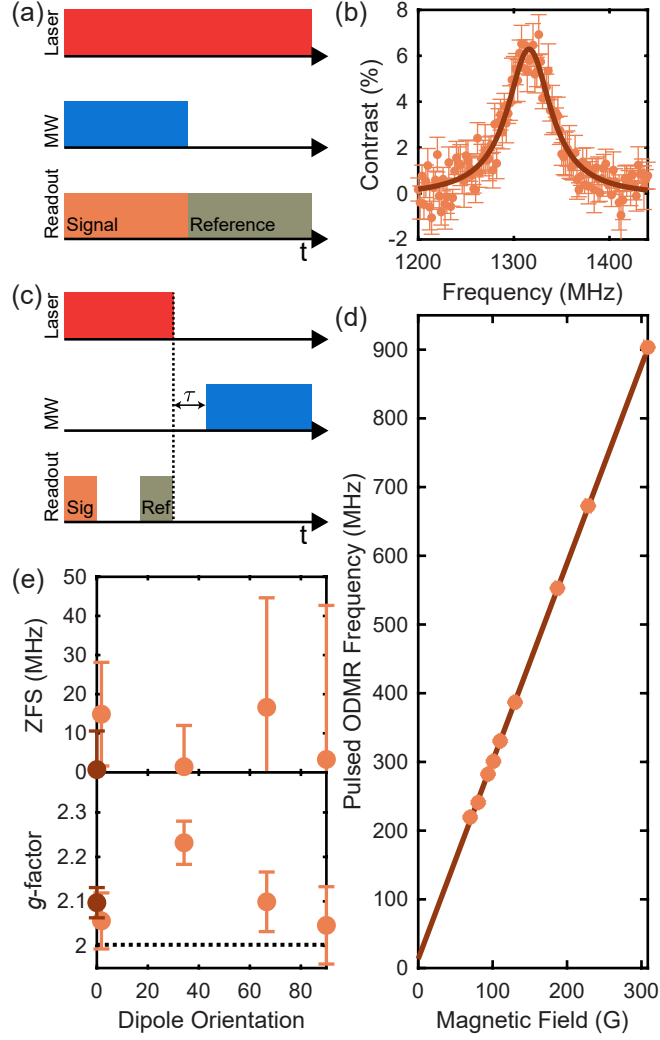


Figure 18: Optically Detected Magnetic Resonance (a) Pulse protocol for continuous-wave (cw) ODMR. (b) CW ODMR spectrum (circles) at 200 μ W optical power, 470 G in-plane applied magnetic field and 0° dipole orientation. The solid line is a Lorentzian fit to the data as discussed in the text. The best-fit result resonance frequency is 1315.9 MHz and full-width half maximum (linewidth) is 27.6 MHz. (c) Pulse protocol for pulsed ODMR. (d) The resonance frequency measured using pulsed ODMR as a function of an in-plane magnetic field. The solid line is a linear fit to the data as discussed in the text. The x- and y-axis error bars are the same size as the data points. (e) The zero-field splitting (ZFS) and g -factor as a function of dipole orientation. The light (dark) orange data are obtained from pulsed (cw) ODMR. All error bars represent one standard deviation.

show a strong dependence of the resonance contrast and linewidth on microwave pulse duration, microwave power and optical power (Fig. 19). The microwave pulse duration has a strong effect on the contrast, increasing it by $3\times$ on increasing the pulse duration from 10 μ s

to 50 μs , keeping the linewidth ~ 30 MHz. Below 10 μs pulse duration, the contrast is almost zero. The bunching timescales τ_2 ($= \gamma_2^{-1}$) and τ_3 ($= \gamma_3^{-1}$) corresponds to 8.2 μs and 22.7 μs respectively at 470 G and 0° dipole orientation (Fig. 8(f)-(g)). These timescales are related to the spin-dependent relaxation rates to the ground state and can explain the low contrast at lower pulse duration. If the microwave pulse polarizes the spin before it had time to completely relax to the ground state before the next pulse, that would reduce the contrast. With microwave power, we see an expected saturation of contrast and linewidth. Using microwave-power-dependent contrast and linewidth, we estimate spin relaxation time T_1 to be 42.13 ± 19.06 μs and spin coherence time T_2^* to be 0.045 ± 0.02 ns (Fig. 21). With optical power, we see a non-monotonic change in contrast and linewidth and find the optimum power to be in the range 150 μW to 300 μW for maximum contrast. These optimization measurements help improve contrast and reduce the linewidth as well as understand the relation of microwave pulse duration and optical power to the spin-dependent excitation and relaxation timescales. Such optimization could help improve the low spin-resonance contrast observed in h-BN emitters and ensembles [39, 83, 184].

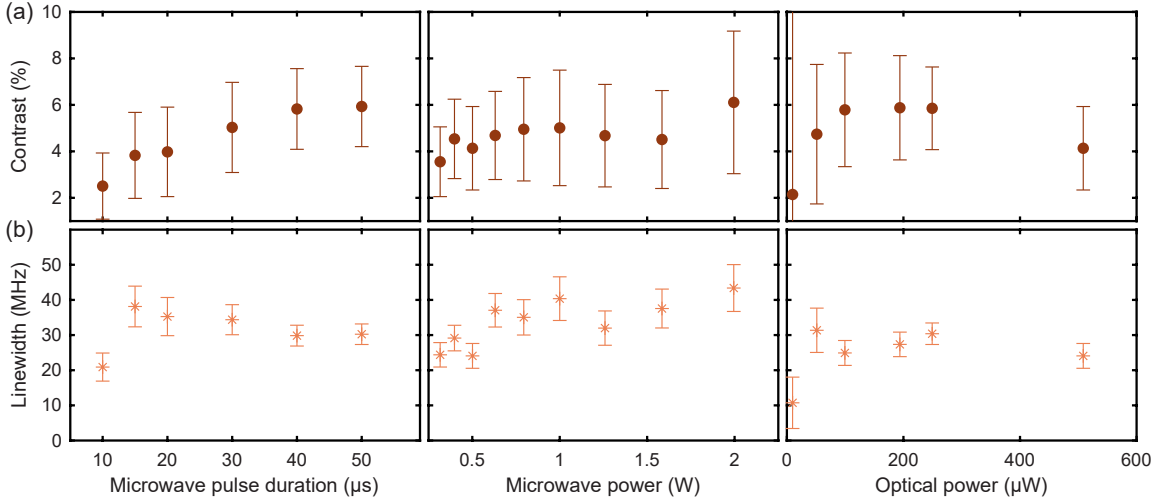


Figure 19: Optically Detected Magnetic Resonance Contrast and Linewidth. (a) The cw ODMR contrast and (b) the linewidth as a function of microwave duty cycle, microwave power and optical power for 470 G in-plane magnetic field and 0° dipole orientation. All error bars represent one standard deviation.

Upon optimizing the parameters of cw ODMR, we use pulsed ODMR to probe ZFS,

g -factor and hyperfine interactions. Figure 18(c) presents the pulse protocol for pulsed ODMR measurement where a 40 μs laser pulse is followed by a 20 μs wait (τ) and 40 μs microwave pulse. During the laser pulse, the readout consists of signal during first 5 μs and reference during last 5 μs . The pulse durations and optical power used were obtained from measurements to maximize the SNR discussed later. The pulsed ODMR contrast is obtained by normalizing signal with reference. At 1.8° dipole orientation, 350 μW optical power and 0.63 W microwave power, we find the resonance frequency in pulsed ODMR to vary linearly with in-plane magnetic field (Fig. 18(d)). Figure 20 presents data for 34.2° , 66.6° and 90° dipole orientation. A linear function accounting for uncertainty in frequency and magnetic field is fit to the data,

$$R(M) = R_0 + s \times M \quad (6.3)$$

where M is the magnetic field, s is the slope and R_0 is the y-intercept. The y-intercept corresponds to the ZFS and s divided by Bohr magneton gives the g -factor. We find the

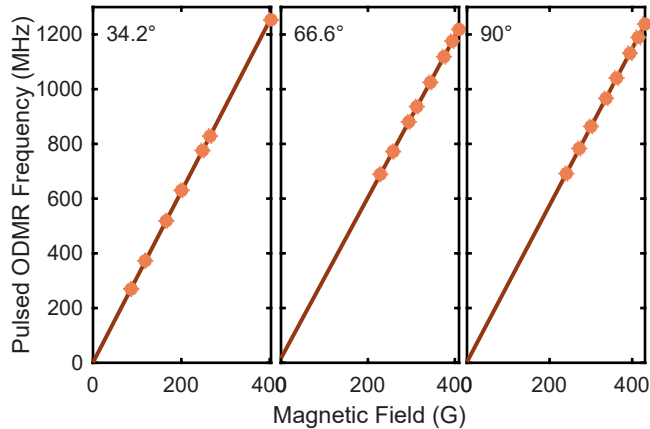


Figure 20: Resonance Frequency at various Dipole Orientations. The circles represent resonance frequency for a given dipole orientation at an in-plane magnetic field, determined using the Lorentzian function (Eq. 6.2) discussed in the text. The data were acquired at 350 μW optical power and 0.63 W microwave power for 34.2° orientation and 1 W for 66° and 90° orientation. The solid line is a fit to the data using the linear function (Eq. 6.3) discussed in the text. The error bars are same as the size of the data points and represent one standard deviation.

ZFS to be zero within the experimental uncertainty. We estimate the g -factor to be ~ 2 , close to the free electron g_e -factor of 2.0023 though slightly larger. The observation of no ZFS is in contrast with recent reports of low ZFS from ODMR of h-BN emitters at cryogenic and room temperature, though the g -factor of ~ 2 is consistent [39, 184]. However, low or no ZFS and similar g -factor but heterogeneous distribution of ZPL from ~ 550 nm to 800 nm is very striking. Most previous reports on h-BN emitters have treated such a wide range of ZPL to most likely originate from distinct underlying defect structures [2, 116, 167, 169, 190, 197, 209]. Further, for various dipole orientations, we find no ZFS and an isotropic g -factor ~ 2 (Fig. 18(e)). Based on these observations, we postulate a doublet ($S = \frac{1}{2}$) spin state.

The spin relaxation time T_1 and spin coherence time T_2^* can be estimated from the ODMR linewidth's and contrast's microwave power dependence using the following equa-

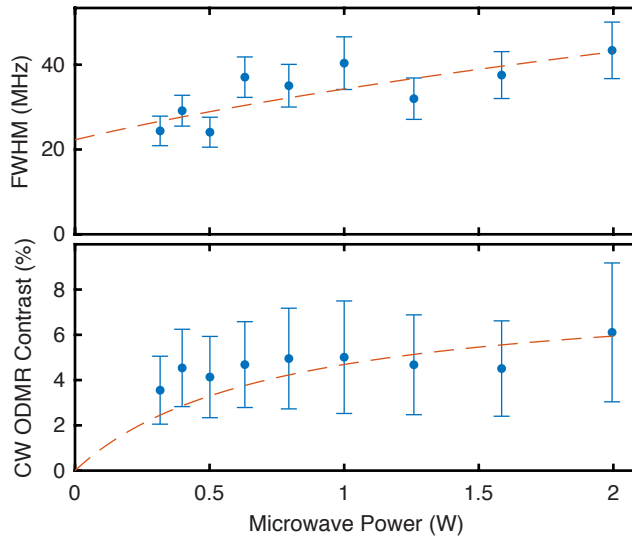


Figure 21: Estimating Spin Relaxation and Coherence Times. (Top panel) Linewidth (FWHM) and (Bottom panel) contrast from cw ODMR as a function of microwave power for 0° dipole orientation, 200 μ W optical power and 470 G in-plane applied magnetic field. The red dashed lines represents solution to Eq. 6.4-6.6. The estimated $T_1 = 42.13 \pm 19.06$ μ s and $T_2^* = 0.045 \pm 0.02$ ns. All errors represent one standard deviation.

tions:

$$\sigma^L = \frac{\sqrt{1 + \beta T_1 T_2^* P_{\text{MW}}}}{T_2^*} \quad (6.4)$$

$$\text{Contrast} = \frac{A\beta T_1 T_2^* P_{\text{MW}}}{1 + \beta T_1 T_2^* P_{\text{MW}}} \quad (6.5)$$

$$[(\sigma^L)^2 \times \text{Contrast}] = \frac{A\beta T_1 P_{\text{MW}}}{T_2^*} \quad (6.6)$$

In these equations, σ^L is the Lorentzian linewidth, A is a constant, β is a constant that determines microwave photon absorption efficiency and P_{MW} is the microwave power. With σ^L , Contrast and P_{MW} as known variables from microwave-power-dependent ODMR measurements, the above set of equations are solved simultaneously to approximate T_1 , T_2^* , A and β . Figure 21 shows the resultant solution as red dashed lines. From the simultaneous fits, T_1 is approximated to be $42.13 \pm 19.06 \mu\text{s}$ and T_2^* is approximated to be $0.045 \pm 0.02 \text{ ns}$. This T_2^* is extremely short and thus not observable in a Rabi measurement. For a longer T_2^* that can be observed in a Rabi measurement, stronger AC magnetic field strength generated by the microwaves would be required that can drive the spin oscillations resonantly between the two levels of the proposed doublet spin state. In this work, the effective AC magnetic field strength at the single spin is limited due to the device configuration that uses an antenna (aluminum wire) located relatively far from the single spin.

6.4. Time-Domain and Spin Dynamics

We next probe time-domain and spin dynamics to understand the optical and spin timescales crucial to designing optical and microwave pulse protocols for coherent control of the spin. We first probe the time-domain PL emission to understand the dark-state recovery rate (Fig. 22(a)-(c)). The pulse protocol involves laser modulation and recording the time-domain PL emission (Fig. 22(a)). The measurement is performed on changing the laser modulation - the time τ between the laser pulses. For each τ , the measurement is repeated 50,000 times. Figure 22(b) shows the time-domain PL for 50 μs laser pulse with counts recorded at 1 μs time bin (corresponding to 1 MHz clock-rate) for τ varying from 0 μs to 600 μs . As a visualization guide, each time-domain PL is shifted on x-axis by its respective τ . On

increasing τ , we find an increase in the PL recovery of up to 70%, with the recovery time of 72.7 μs determined by fitting an exponential function to the PL recovery, shown as the dashed line in Fig. 22(b) and the dotted line shows the eventual decay to the steady-state PL. To better understand the rise and decay timescales and the amplitude of PL recovery as a function of τ , we repeat the measurement for 250 ns time bin (4 MHz clock-rate) and determine the rise time, the decay time and the amplitude of time-domain PL for each τ . Top panel of Fig. 22(c) shows the amplitude and the bottom panel shows the decay time as a function of τ . We estimate the recovery rate from the amplitude variation to be 32.9 μs that saturates after 100 μs wait time. We estimate the minimum decay time to be ~ 5 μs for wait time of 100 μs or more. These dark-state recovery timescales agree with the bunching timescales observed in photon autocorrelation measurements. These timescales indicate that tens of μs long laser pulse would be required to initialize the spin into the ground state for coherent spin control measurements, which would be an order of magnitude higher than that required for defects such as the nitrogen-vacancy center in diamond [94]. To better understand the effect of optical power on spin dynamics, we measure the microwave modulated time-domain PL at various optical powers (Fig. 22(d)). At resonance frequency of 1308.5 MHz, $\sim 0^\circ$ dipole orientation and input microwave power of 0.63 W, microwaves are modulated with 40 μs pulse duration and time-domain PL recorded using 1 μs time bin under continuous laser excitation. The measurement consists of 100,000 repeats, with each repeat 80 μs long. Figure 22(e) presents time-domain PL for microwaves on (dark orange circles) and off (light orange circles) under 150 μW (top panel) and 510 μW (bottom panel) optical power. The dotted lines represent the steady-state PL, estimated from the time-domain PL after the rise (microwaves on) or decay (microwaves off) to a steady-state. We find a non-monotonic optical power dependence of the PL contrast for microwaves on and off, estimated from the steady-state. The contrast is $\sim 7\%$ under 150 μW optical power whereas it is $\sim 2\%$ under 510 μW optical power. We estimate the decay time of PL for microwaves off as a function of the optical power and find it to vary linearly (Fig. 22(f)). This indicates a slow pumping of the spin into the ground state at lower optical powers.

Optimizing the optical power for optimum contrast and decay time is essential to designing pulse protocols for coherent control, keeping a check on the duration of each sequence and thus total measurement time accounting for several thousand repeats.

We thus turn to optimizing the optical power, the signal readout time and the wait time between optical and microwave pulses by maximizing the SNR as a function of microwave pulse duration. We record optical spin contrast using the pulse protocol shown in Fig. 22(g) at resonance frequency of 1308.5 MHz and $\sim 0^\circ$ dipole orientation. Informed by the dark-state recovery rate and bunching timescales, we set the initialization optical pulse to be 40 μs to ensure maximal initialization of the spin into the ground state, setting wait time τ to be 10 μs or 20 μs . The optical pulse for signal readout is set to 40 μs as well, whereas the microwave pulse duration is varied from 0 μs to 40 μs . Wait time T following the signal readout is same as τ plus microwave pulse duration to ensure equal wait between each optical pulse. The SNR is determined using the equation

$$\text{SNR} = \sqrt{\alpha} \times \frac{C}{\sqrt{2 - C}} \quad (6.7)$$

where α is the single-shot readout and C is the contrast [94]. Figure 22(h) shows optical spin contrast in time-domain PL after microwaves on and off under 350 μW optical power, 20 μs wait time and 40 μs microwave pulse, corresponding to signal and reference in Fig. 22(g). For a readout time, α is determined by summing time-domain PL within the readout window after microwaves on and off, and $C = (\text{PL}_{\text{on}} - \text{PL}_{\text{off}})/\text{PL}_{\text{off}}$ (Fig. 23). Figure 23 is a highlighted version of Fig. 22(h) showing a readout window. The green highlighted region corresponds to readout window from which α and C are determined. The gray highlighted region corresponds to signal and reference counts having no contrast. From each optical spin contrast curve, we calculate SNR for readout times in the range of 2 μs to 20 μs . We record optical spin contrast curves on varying the optical power, the wait time and the microwave pulse duration. We find the best SNR for a 5 μs readout time (Fig. 22(i)). We find the best SNR as a function of microwave pulse duration under 350 μW optical power (left panel) and

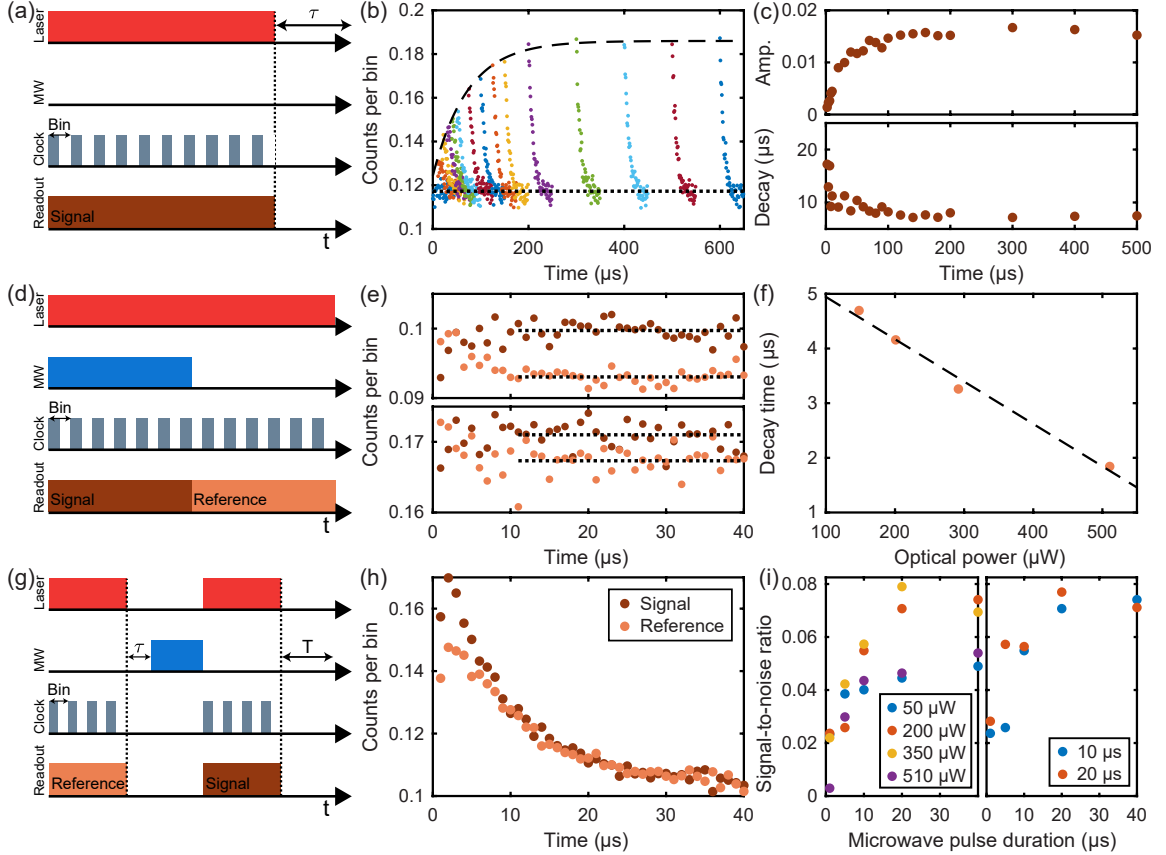


Figure 22: Time-Domain and Spin Dynamics. (a) Pulse protocol for time-domain photoluminescence (PL) measurement. (b) Time-domain PL as a function of wait time acquired at 350 μW optical power, ~ 91 G in-plane magnetic field and 34.2° dipole orientation. PL counts acquired using 1 μs time bins. (c) PL amplitude and decay rate as a function of wait time obtained from each time-domain PL acquired using 250 ns time bins at 350 μW optical power, ~ 73 G in-plane magnetic field and 90° dipole orientation. (d) Pulse protocol for microwave modulated time-domain PL measurement. (e) PL counts per 1 μs time bin during 40 μs microwave on (dark orange circles) and off (light orange circle) pulse, at an optical power of 150 μW (top panel) and 510 μW (bottom panel), 1308.5 MHz resonance frequency, $\sim 0^\circ$ dipole orientation and 0.63 W input microwave power. (f) Decay time as a function of optical power for microwave modulated time-domain PL during microwave off pulse. (g) Pulse protocol for optical spin contrast measurement. (h) PL counts for 1 μs time bin corresponding to signal (dark orange circles) and reference (light orange circles) readout, at 350 μW optical power, 20 μs wait time and 40 μs microwave pulse. (i) Signal-to-noise ratio as a function of microwave pulse duration for 5 μs readout time, as a function of optical power (left panel) and wait time (right panel), calculated using equation discussed in the text.

for 20 μs wait time (right panel). Figure 24 presents the SNR for various readout times and all the optical powers, microwave pulse durations and wait times probed. These results show

the importance of optimizing the various initialization, control and readout parameters.

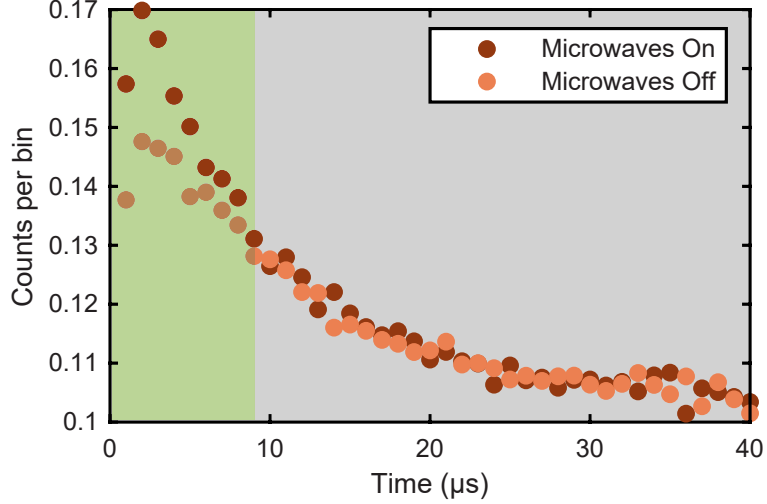


Figure 23: Optical Spin Contrast. Time-domain PL after microwaves on (dark orange circles) and off (light orange circles), corresponding to signal and reference in pulse protocol in Fig. 22(g). The green highlighted region is the readout window of optical spin contrast whereas the gray highlighted region corresponds to no contrast.

6.5. Conclusion

To conclude, we present a pure single spin in h-BN at room temperature characterized by noise-limited $g^{(2)}(0) = 0$. Using PECS, we characterize its magnetic-field-dependent temporal dynamics showing signature of presence of spin. Using cw and pulsed ODMR, we confirm a single spin. We find absence of ZFS and an isotropic g -factor ~ 2 , close to that of a free electron, at various dipole orientations. Based on these observations, we postulate a doublet ($S = \frac{1}{2}$) spin state. Using optical and microwave pulse protocols, we probe time-domain and spin dynamics. We determine the dark-state recovery rate that sets a lower limit on the optical pulse initialization time. We find a non-monotonic dependence of optical spin contrast on optical power, essential to maximizing the spin contrast. We optimize the optical power and wait time in pulse protocols crucial to spin initialization and readout using SNR. Our results show the importance of understanding optical and spin dynamics of single spins in h-BN, crucial to developing methods to coherently control the single spin. Further, we find the single spin to be extremely stable in ambient conditions having survived optical and microwave excitations of over hundreds of hours. This is significant improvement in the

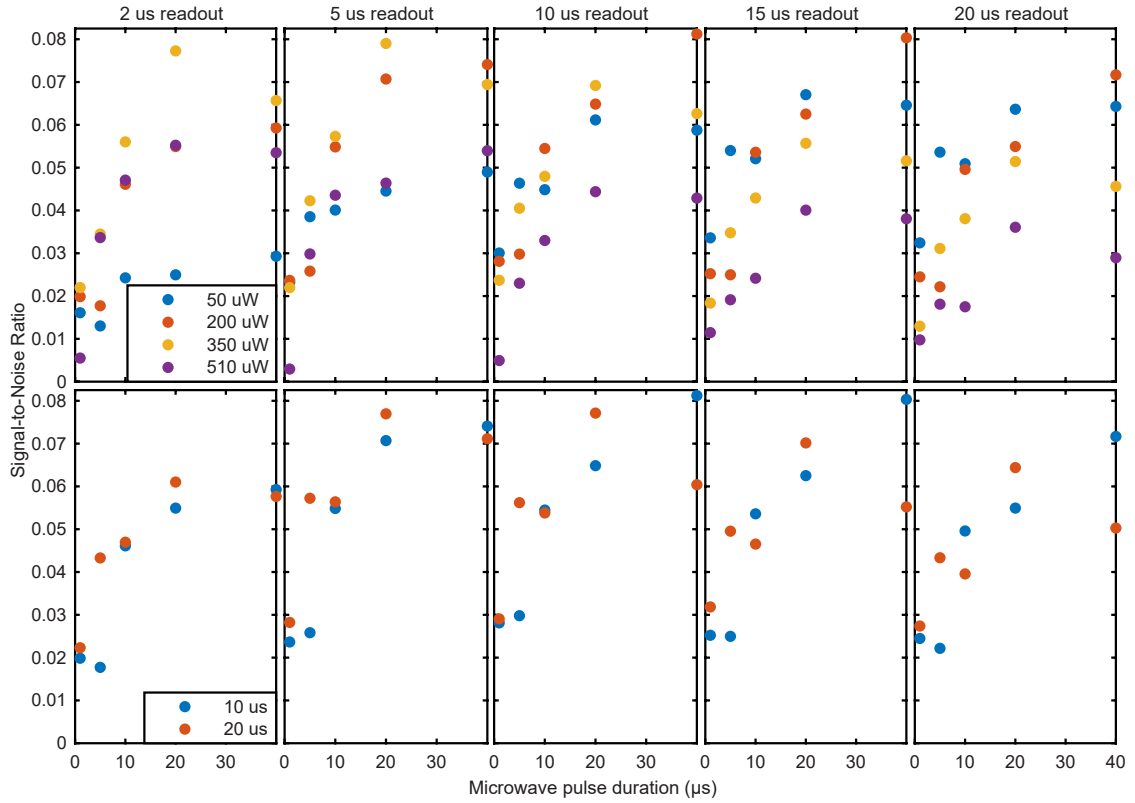


Figure 24: Signal-to-Noise Ratio. SNR as a function of microwave pulse duration for different readout times for (top row) varying optical power and (bottom row) varying wait time determined from optical spin contrast measurements.

h-BN SPE stability which otherwise have been prone to photobleaching in matter of minutes or a few hours. Building on these results, future work could focus on coherent control of single spin and conclusive identification of the nature of underlying defect.

CHAPTER 7 : Conclusion and Future Directions

Since the first published report of QEs in h-BN [194] and ~ 250 reports since then, electronic and chemical nature of the underlying defects giving rise to visible quantum emission remain unknown. Pure SPEs and optically-addressable single spins have remained elusive. In this thesis, I worked to probe the optical and spin dynamics of QEs in h-BN at room temperature. Understanding of the optical dynamics and as a result the electronic level structure was achieved through PECS and numerical simulations of electronic level structure models. To the best of our knowledge, we reported the first observation of pure SPEs in h-BN having noise-limited photon antibunching, $g^{(2)}(0) = 0$. Understanding of the spin dynamics was achieved in two steps. First, PECS was used as an analytical tool to look for signature of single spins. Second, ODMR was used to confirm presence of spin, and optical and microwave pulse protocols were designed and used to probe spin dynamics. To the best of our knowledge, we were first to observe a pure single spin in h-BN. With the requirement of high purity SPEs and single spins for various quantum technological applications, both the above observations are important milestones in the progress of h-BN as an ideal defect host material. This thesis includes material adapted from manuscript in peer review [155] and preparation, at the time of writing of this thesis. Furthermore, this thesis includes devices, experimental setup and methods that made crucial contributions to manuscripts published in *Nature Communications* [66], *ACS Photonics* [30], *ACS Nano* [179] and two manuscripts in revision and peer review [70, 149].

In the study of solid-state QEs, confirming quantum or non-classical light emission is imperative. Thus, calculating photon correlations from Hanbury Brown and Twiss interferometry is ubiquitous. The photons contain vital information regarding the QE's electronic level structure due to the optical, spin and charge dynamics. These dynamics give rise to radiative and nonradiative transitions that determine the timing and other properties of the emitted photons such as its polarization. The dynamical information of the system is always present in the photon correlations. However, that information is seldom used to understand

the internal dynamics, which when used in conjunction with theoretical calculations can be used to predict the electronic level structure and thus the underlying defect structure. We utilize the information from the photon correlations of QEs in h-BN to understand the electronic level structure and postulate the underlying defect structure. Our observations and theoretical model explain previously unexplained optical dynamics. We also report the first observation of pure SPEs in h-BN having noise-limited photon antibunching, $g^{(2)}(0) = 0$, a strict requirement for various quantum technological applications. Our observations in ambient conditions affirms the potential of QEs in h-BN for room temperature quantum technologies. More generally, our framework is a powerful tool for probing QEs in any material platform.

Single spins in h-BN have been of great interest. However, they have remained elusive. In this thesis, we present a framework for probing presence of single spin using PECS. We observe magnetic-field-dependent photon correlations of a pure SPE, a clear signature of presence of spin. We confirm the presence of spin using cw and pulsed ODMR at room temperature – a first ever observation of a pure single spin in h-BN. We find absence of ZFS and isotropic g -factor ~ 2 . We postulate a double ($S = \frac{1}{2}$) spin state. Using optical and microwave pulse protocols, we probe the time-domain and spin dynamics of the single spin. We investigate the dark-state recovery rate and observe optical spin contrast, optimized using signal-to-noise ratio.

The progress on QEs in h-BN so far has been exciting and promising. The future directions and questions yet to be answered are plenty. Broadly, areas that require focus could be categorized into materials, defect structures, single spins, devices and applications. These areas require targeted approach that can help push the understanding of QEs in h-BN toward realization of scalable devices and practical applications. Several of the target areas are coupled to one another - advancement in one would lead to progress in others, requiring parallel efforts.

In the near term, materials is an important area where concentrated effort in materials

growth, treatment and characterization has an important role to play. Currently, various h-BN source materials are studied such as nanopowder, nanocrystals, exfoliated flakes from bulk crystals and large-area CVD thin films. The source and type of starting h-BN material means different device preparation and treatments. This is advantageous in being able to compare and contrast various h-BN source materials. However, the material heterogeneity affects the defect heterogeneity due to material treatment effects as well as it takes focus away from scalable materials such as bulk crystals or large thin films. For instance, h-BN devices for studying QEs have commonly undergone heat treatment of 850 °C in a furnace for 30 minutes irrespective of the h-BN source material. The QEs in h-BN are highly susceptible to photobleaching, making them unstable to survive for long. Exploring the optimum heat treatment to achieve photostable QEs in h-BN is a need of the hour. To be able to understand a QE to its fullest extent, its photostability is a must. Otherwise the characterization is incomplete. Partial success has been achieved in creating photostable QEs. In this thesis, several annealing temperatures and times were used to compare the photostability of QEs across devices consisting of h-BN prepared from similar bulk crystals (Appendix C). Limited data suggests longer annealing time of 2 hours at 850 °C lead to extremely photostable QEs that survived (and continues to survive) hundreds of hours of laser illumination under ambient conditions. Limited data suggests QEs have not been observed in devices annealed at certain temperatures, which might partly be dependent on the defect formation energies [209]. A lot remains to be understood on the material aspect including h-BN source material, device preparation and treatments that can lead to highly photostable QEs required for practical applications, shed light on the possible defect structures and their properties, and more.

Identifying defect structures giving rise to quantum emission in h-BN has been the primary goal. Recently, there has been some progress with the identification of the negatively-charged boron vacancy (V_B^-) occurring as an ensemble. However, single defects including single V_B^- are yet to be identified. One challenging though highly rewarding approach is to use electron microscopy to create and characterize single defects [88]. In this approach, a

scanning or transmission electron microscope could be used to controllably and deterministically create defects followed by its optical characterization. For instance, controllably removing single boron or nitrogen atom in an undoped h-BN film could create boron or nitrogen vacancy based defects. In a carbon doped h-BN film, carbon based defect complexes could be achieved such as $V_N C_B$ and $V_B C_N$. This could potentially help confirm or rule out various theoretical defect proposals by comparing the resulting defects' optical properties to theoretical proposals as well as experimental observations. Such focused efforts could help speed up the experimental identification of chemical nature of quantum defects in h-BN.

Optically interfaced single spins in h-BN have been pursued since QEs in h-BN were discovered. Until observed in work as part of this thesis, pure single spin in h-BN have remained elusive. Spin resonance of QEs in h-BN at cryogenic [39] and room temperature [184] was recently reported. Spin resonance of a pure SPE discussed in this thesis is the first observation of a pure single spin. However, a lot remains to be understood about the single spins including the nature of their origin and its coherent control for quantum technological applications. Knowing the defect structure can aid in material growth and device preparation for deterministic creation of single spins. Further, hyperfine interaction with the nearby nuclear spins can be used to make a quantum register or memory. With different boron and nitrogen isotopic concentration, the spin coherence as well as hyperfine interactions could be altered, opening avenue of material processing to achieve different isotopic purity for improving device performance.

Several studies have focused on applications of QEs in h-BN. As high purity SPEs at room temperature, they are ideal for room-temperature quantum sensing and communication. This is a big improvement in the temperature range h-BN QEs can operate at compared to several other solid-state systems that operate only at cryogenic temperatures. They have also been shown to have Fourier transform limited linewidth, a requirement for various applications. Nanophotonic devices enable material and device integration, tunable properties, and more. Recent observations of single spins open up new avenues of fundamen-

tal studies and applications of spin-photon entanglement. With h-BN's low dimensionality, single spins could be integrated with other low dimensional materials to obtain unique properties. For instance, a spin current in a low-dimensional magnetic material could be used for coherent control of single spin in an all electric control scheme. With h-BN's compatibility with numerous materials, the possibilities are countless.

The second quantum revolution has brought together academia, government and industry as the field of quantum information science is moving toward practical applications beyond a laboratory. The current time to work on quantum technologies is as exciting as it can be. There is a vast amount of research and development that is yet to happen over the coming decades. I am excited about the opportunities from exploring fundamental physics to real life applications. I look forward to the new developments in the field of quantum information sciences and the improvements it brings in the lives of billions around the world and the role played in it by quantum emitters in hexagonal boron nitride.

APPENDIX A: Experimental Setup

Figures 25-27 presents the pictures of the experimental setup showing the free-space optics, optomechanical components, stages, etc. Figure 25 shows the various optical paths dedicated to 532 nm cw excitation (green highlighted line), 592 nm cw excitation (orange highlighted line) and broadband excitation (white highlighted line) for a broadband pulsed (NKT Photonics, Fianium Whitelase) and continuous-wave (Hübner C-WAVE VIS) laser. Figure 26 shows the excitation (represented as orange line) and collection (represented as red line) path aligned at the long-pass dichroic. Figure 27 shows the X, Y, Z and Piezo stages controlling the position of the objective, the sample mounted on a rotation stage to control the dipole orientation and a magnet mounted on a linear stage to control the magnetic field strength. The linear stage is on a goniometer that controls the magnetic field orientation.

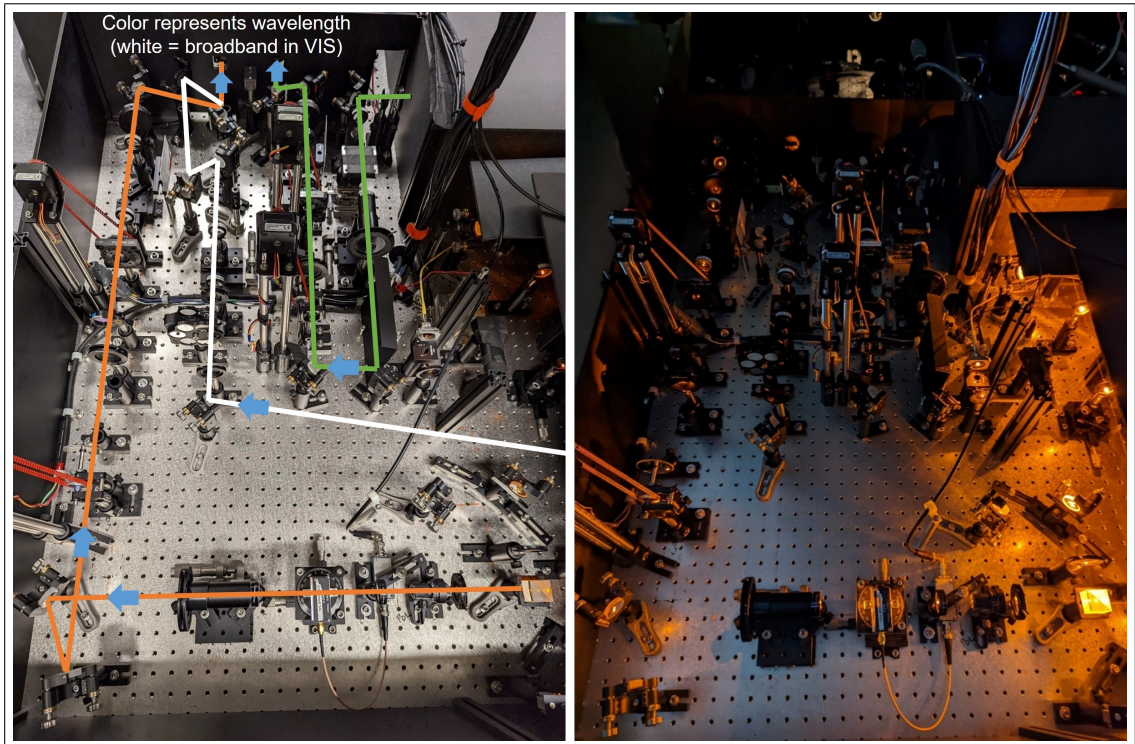


Figure 25: Free-Space Optics and Controls.

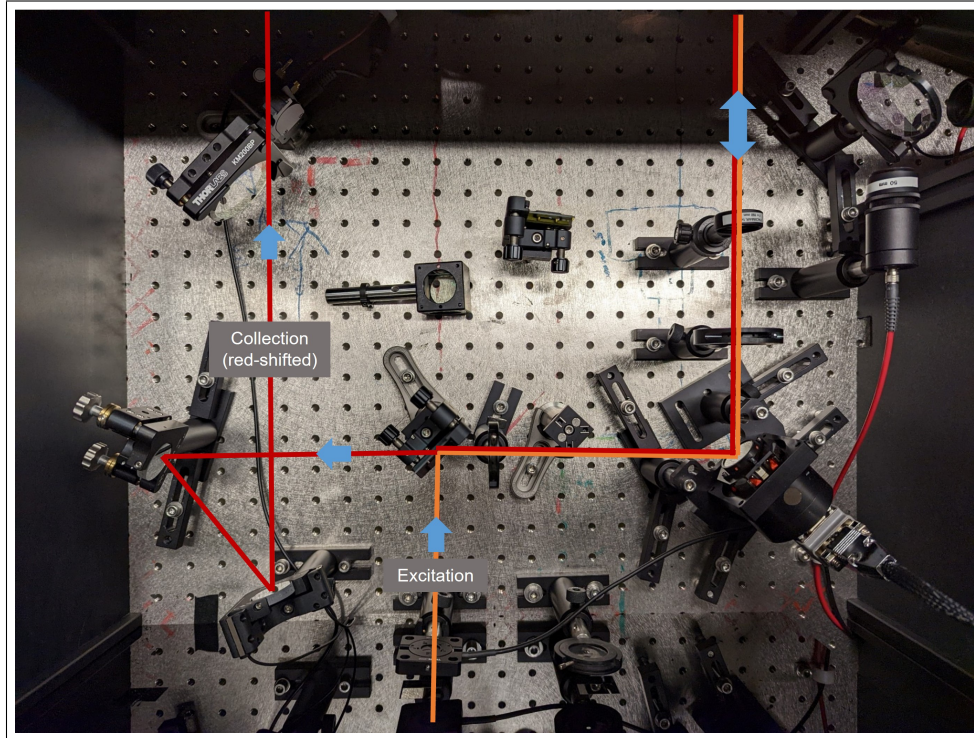


Figure 26: Excitation and Collection Optical Paths.

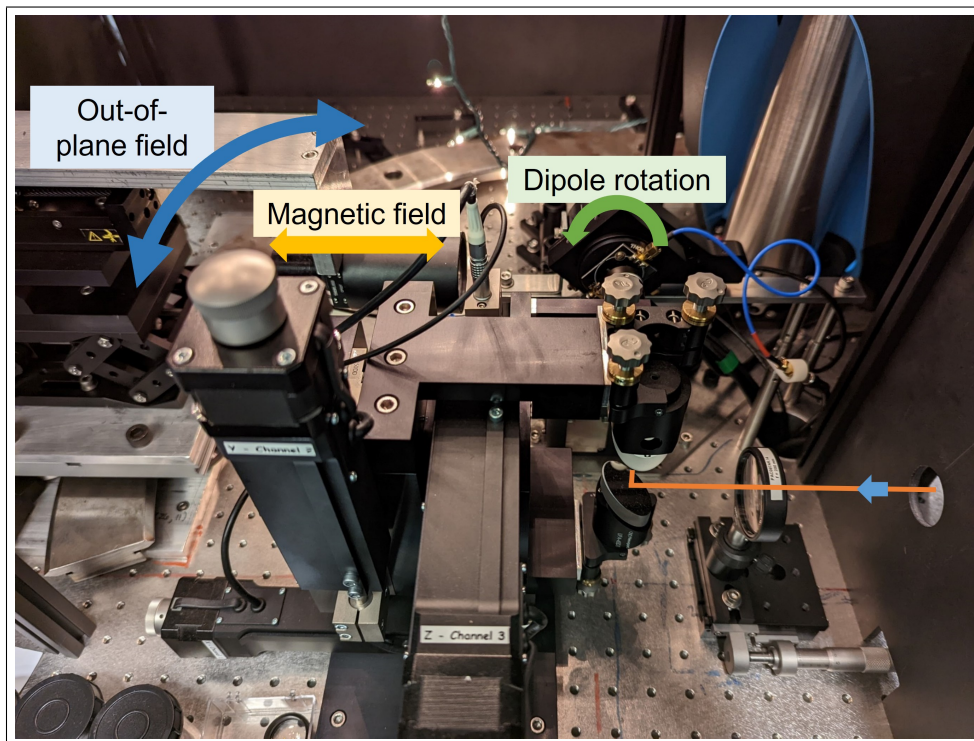


Figure 27: Sample Stage and Magnetic Field Control.

APPENDIX B: Custom Software Control

The experimental setup control and data acquisition for this thesis was done through custom software developed in MATLAB. The custom software was designed and developed to have the following features:

1. Hardware and software integration
2. Real-time status update using events and listeners
3. Automated data acquisition
4. Remotely controlled experimental setup
5. General purpose graphical user interface
6. Integrated analysis

The hardware integration was done by developing custom software drivers for a variety of optomechanical and electronic components. This enabled system integration of different hardware components and its real-time status update. The system integration enabled automated data acquisition with the experimental setup's capability to self-operate for days, only limited by the sample stability such as the photostability of QEs. The experimental setup was designed to be remotely controlled. Combined with automated data acquisition, the experimental setup built and used in this thesis enabled remote measurements of an array of ~ 150 nitrogen vacancy centers in nanodiamonds over a period of two weeks [179]. A general purpose graphical user interface (GUI) (Fig. 28-30) was developed to simplify and speed-up device characterization as well as make it accessible and user-friendly. It was designed to work on four distinct experimental setups in the lab. The GUI enabled integrated analysis of several measurements to speed-up device characterization. For instance, the excitation or emission polarization measurement was integrated with a fitting routine that provided the user with the dipole orientation of the QE, with the option to change the

excitation or emission polarization to the dipole orientation.

Figures 28-30 presents the general purpose GUI. The GUI consists of multiple panels that enables setup selection, control of measurement parameters or stages of the confocal microscope, and a few basic experiments. Several measurements are performed directly through the scripts. Figure 28 is a screenshot of the measurement control panel of the GUI. It enables the user to control a variety of measurement controls such as lasers, excitation polarization, excitation power, magnetic field strength, etc. The real-time status of all the measurement controls is updated and saved on the hard drive. The measurements are designed to save the status of the external controls with the raw data for future reference and consistency. Figure 29 is a screenshot of the stage controls of the confocal microscope's objective. Figure 30 is a screenshot of panel for photoluminescence scan.

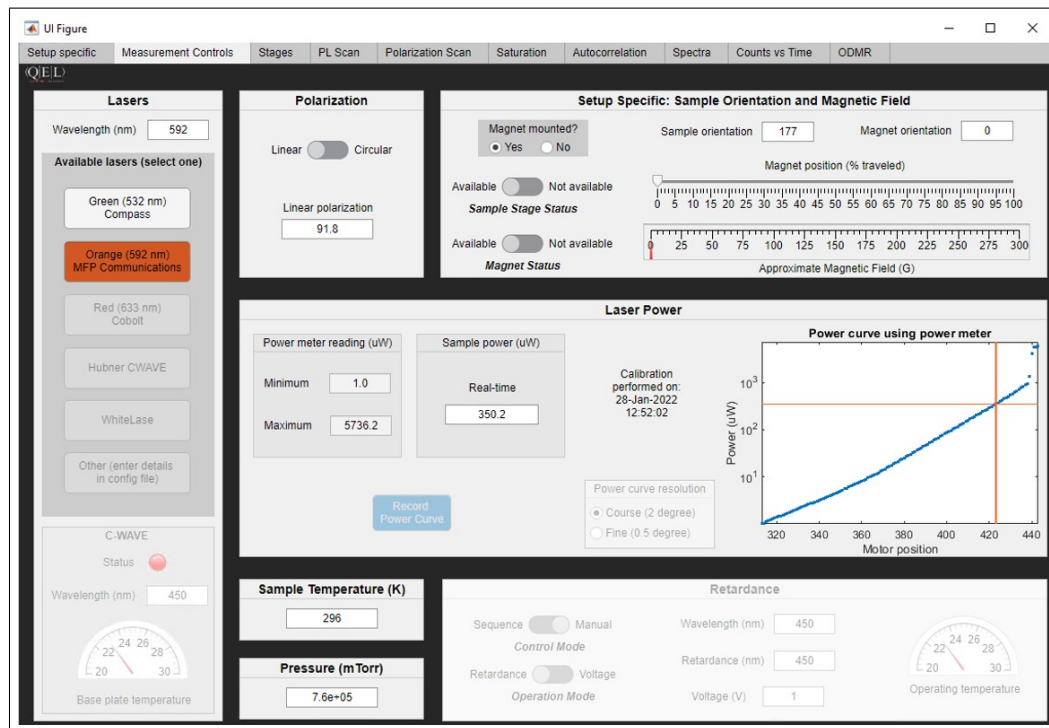


Figure 28: Measurement Controls

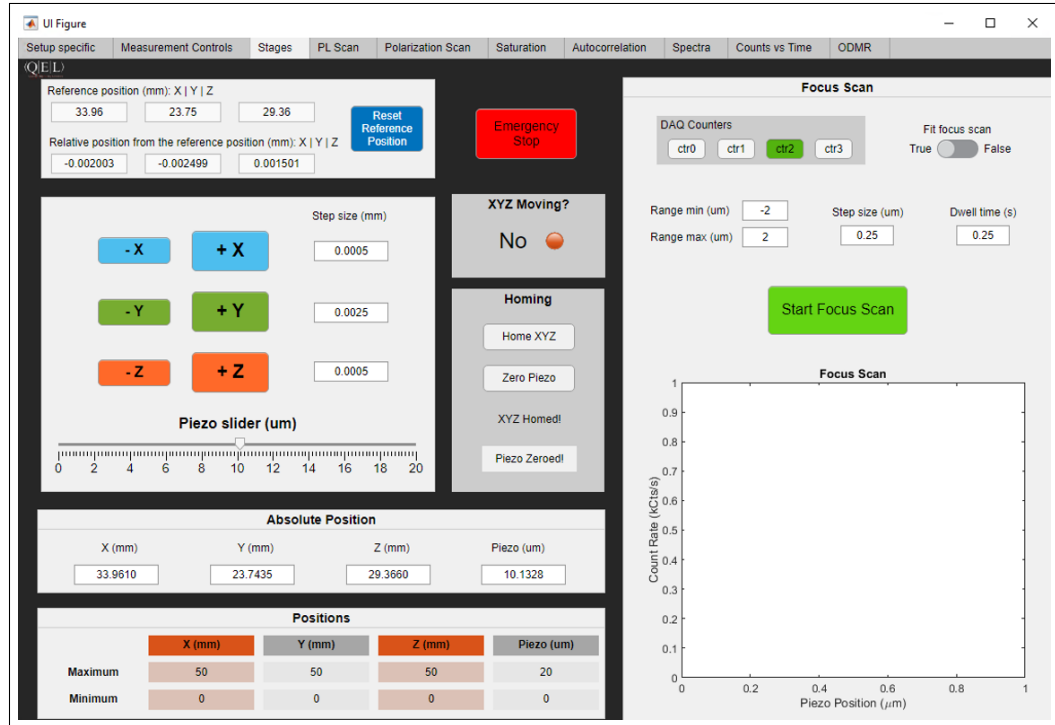


Figure 29: Stage Controls

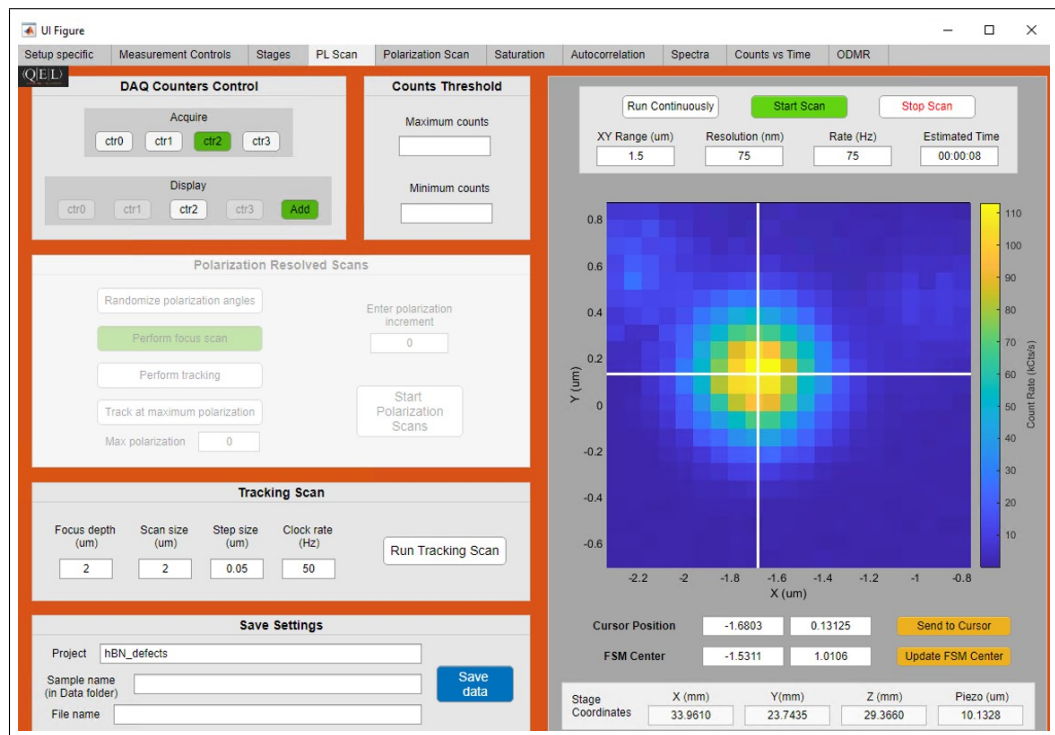


Figure 30: Photoluminescence Scan

APPENDIX C: Annealing Study

Annealing the h-BN is perhaps the most important step of device preparation and characterization. It affects the photostability of QEs, possibly the underlying defect structure that have different formation energies [209] and the overall device preparation and performance. Annealing h-BN substrates, most commonly in a tube furnace is believed to be responsible for creating optical defects. However, the underlying mechanism remains unknown. Thus, annealing is an important step of the process that has wide implications but has received the least attention. In this thesis, emitters were never observed in unannealed h-BN samples. Inspired from other solid-state materials, h-BN substrates are commonly annealed at 850 °C for 30 minutes, usually in an atmosphere of Ar or N. These conditions have failed to create QEs that are photostable and have homogeneous properties. While annealing is a step that would require revisiting once the defect structures are experimentally confirmed so that the process can be tuned and optimized for stable and homogeneous defects, there is a lot that needs to be done now. For instance, the process conditions could be tuned to search for annealing temperatures, times and pressure conditions that improves the photostability. Further, the effect of different annealing temperatures on the creation of optical defects and its properties could inform about possible formation energies and thus the possible defect structures. Thus, studying the effect of annealing conditions can help achieve stable defects as well as identify the underlying defect structures. As part of this thesis, annealing study was performed to improve the defect stability as well as explore the effect of temperature on defect creation. In a second study, the microwave substrates were annealed at various temperatures to understand the effect of temperature on the device's microwave transmission.

C.1. Effect of Annealing on Hexagonal Boron Nitride

The conditions explored were annealing temperature and time, on bulk h-BN crystal and exfoliated h-BN flakes. While the parameter space search performed was not exhaustive, it did lead to improved stability. First, bulk h-BN crystals were annealed at 850 °C for

30 minutes. The exfoliated flakes from annealed bulk crystals did not show any emitters. Second, substrates with exfoliated h-BN flakes were annealed at conditions summarized in

Table 5: Summary of Annealing Study of Exfoliated h-BN

Sample #	Treatment	Observations
5	Plasma clean pre-annealing: No Annealing temperature: 850 °C Annealing time: 30 min.	Number of regions scanned: 7 SPE confirmed: Not confirmed but a few likely due to highly polarized emission Stability: N/A Other information: N/A
9	Plasma clean pre-annealing: No Annealing temperature: 850 °C Annealing time: 30 min.	Number of regions scanned: 13 SPE confirmed: 1 confirmed and few more likely due to highly polarized emission Stability: N/A Other information: 1 region had no emitters
44	Plasma clean pre-annealing: No Annealing temperature: 850 °C Annealing time: 60 min.	Number of regions scanned: 4 SPE confirmed: Not confirmed but possibly ~3 across 2 regions based on highly polarized emission Stability: Other information: 1 region had no emitters
47	Plasma clean pre-annealing: Yes Annealing temperature: 850 °C Annealing time: 120 min.	Number of regions scanned: 11 SPE confirmed: ~5 across 3 regions Stability: Emitters photobleached in 2 regions, SPE in other 3 regions slowly photobleached Other information: No emitters found in 6 regions
51	Plasma clean pre-annealing: Yes Annealing temperature: 850 °C Annealing time: 120 min.	Number of regions scanned: 17 SPE confirmed: ~20 across 5 regions, having highly polarized emission but most of them non-magnetic Stability: bright, mostly stable Other information: 12 regions had many emitters which were either dim, unstable or not a SPE. A single-spin defect observed.
45	Plasma clean pre-annealing: No Annealing temperature: 875 °C Annealing time: 60 min.	Number of regions scanned: 12 SPE confirmed: 3 emitters having >80% visibility showed no SPE but possibly ~20 based on highly polarized emission Stability: 2 out 10 emitters photobleached Other information: 3 regions had no emitters
33	Plasma clean pre-annealing: No Annealing temperature: 900 °C Annealing time: 60 min.	Number of regions scanned: 7 SPE confirmed: No bright emitters were found in any region worth measuring Stability: Only 1 region had emitters which photobleached Other information: N/A
46	Plasma clean pre-annealing: No Annealing temperature: 900 °C Annealing time: 60 min.	Number of regions scanned: 7 SPE confirmed: No bright emitters were found in any region worth measuring Stability: 2 emitters each in 3 regions found photobleached Other information: N/A
35	Plasma clean pre-annealing: No Annealing temperature: 1150 °C Annealing time: 60 min.	Number of regions scanned: 4 SPE confirmed: 3 having highly polarized emission Stability: Bright and stable SPE Other information: ~720 ZPL for all 3 SPE

Table 5. Samples annealed below 850 °C (not presented here) never showed any emitters. As part of the annealing study, samples consisting of multiple h-BN flakes were annealed at temperatures in the range of 850 °C - 1150 °C in the time range of 30 - 120 minutes, excluding the temperate ramp of ~ 3 hours and overnight cool down. The key takeaways were:

1. Annealing at 850 °C for 120 minutes lead to highly photostable SPEs and single spins at ambient conditions that has survived hundreds of hours of laser illumination.
2. Certain temperature ranges do not create emitters, possibly due to formation energies of the underlying defects.

C.2. Effect of Annealing on Microwave Substrates

The microwave substrates (Fig. 2) were designed and developed to enable on chip AC magnetic field by microwave transmission through the metal in trenches. However, during the course of the sample preparation, we found the effect of annealing on the substrates post h-BN exfoliation. At high temperatures, the metal diffuses in to the substrate depending on the metal's diffusivity and the substrate material. To check the effect of annealing on the substrates and the degradation of microwave transmission due to metal diffusion, substrates were annealed at various temperatures followed by measuring its transmission and reflection S-parameters. The measurement was performed with the help of Dr. Mohamad Hossein Idjadi. Figure 31 presents the reflection S-parameters (S_{11} and S_{22}) and transmission S-parameters (S_{12} and S_{21}) of five different substrates, one unannealed and others annealed for 30 minutes. The transmission S-parameters show the degradation in microwave transmission with increase in annealing temperature. The transmission S-parameters for substrates annealed at 700 °C and 800 °C show significant loss in transmission. Further, the substrates unannealed or annealed at ≤ 600 °C had resistance as measured by multimeter of $\leq 564 \Omega$ whereas the substrates annealed at 700 °C and 800 °C had resistance of 7.1 k Ω and 18.15 k Ω , respectively. Thus, annealing the samples consisting of exfoliated h-BN on microwave substrates severely degraded transmission characteristics of the deposited metal and thus

couldn't be used for spin control measurements that would require on chip AC magnetic field. The issue was circumvented by wire bonding an aluminum wire to bonding pads on the microwave chip such that it would pass over the h-BN flake of interest on the substrate, as shown in Fig. 6. Future work should explore metal and substrate combination that would have no or low diffusivity on annealing at 850 °C for 120 minutes or higher.

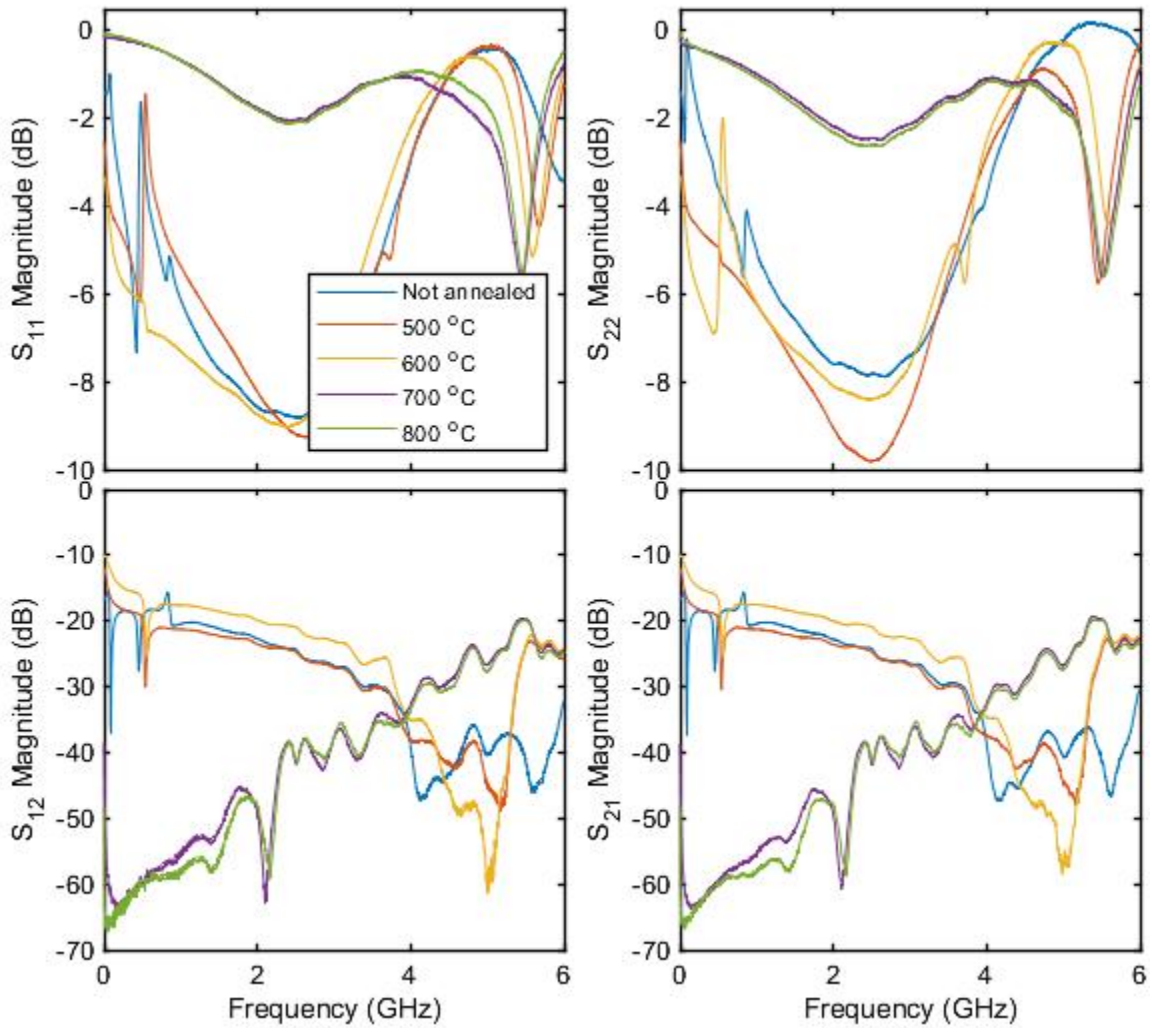


Figure 31: S-Parameters of Microwave Substrates Post Annealing

APPENDIX D: Photon Correlations: Acquisition, Analysis and Application

D.1. Framework

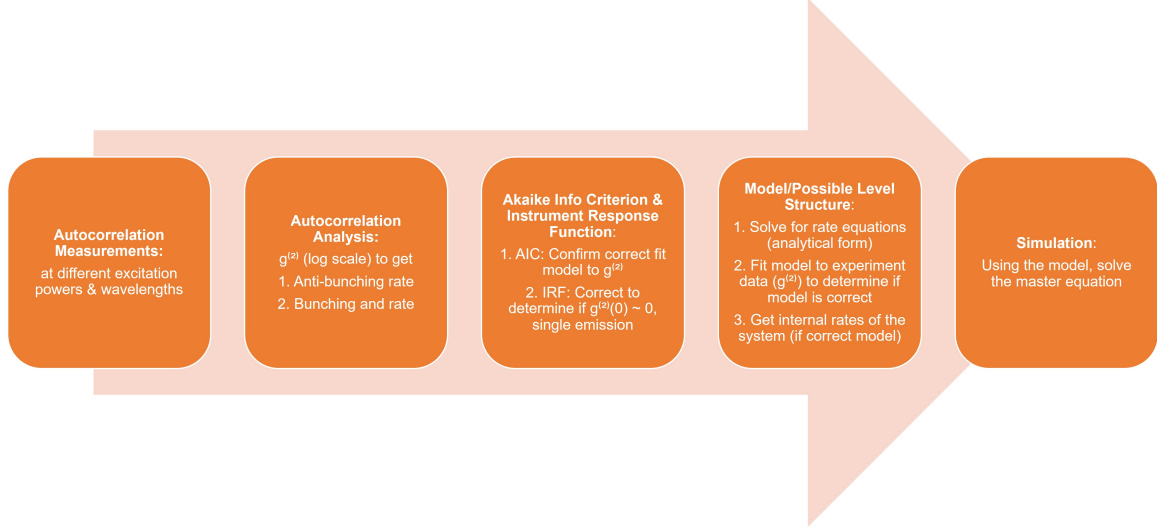


Figure 32: Framework for using Photon Correlations to Model Electronic Level Structure

Figure 32 presents a summary of the framework for using photon correlations to model electronic level structure [70], a summary of discussions in Chapter 4-5. The first step is to calculate second-order photon autocorrelation function (autocorrelation measurements for short) as a function of excitation power and wavelength. It involves data acquisition using Hanbury Brown and Twiss interferometry. The second step is to process the raw data and calculate the autocorrelation function, $g^{(2)}(\tau)$ at delay times τ . The analysis involves calculating $g^{(2)}(\tau)$ for short delay times or linear scale ($\tau \leq 50$ ns) such that it is an order of magnitude larger than the antibunching rate of the QE. The short-time scale $g^{(2)}(\tau)$ is used to determine the antibunching rate. The calculation is then performed for long delay times or logarithmic scale ($\tau \leq 1$ s) to get the bunching rates that are orders of magnitude slower than the antibunching rate and at times in \sim kHz range or slower. Since the antibunching and bunching rates are orders of magnitude different, commonly differing by six orders, the third step involves analysis to determine the best-fit empirical model. This involves using Akaike information criterion, instrument response function and reduced chi-squared

statistic to compare different empirical models as well as confirm single-photon emission with high confidence level. The fourth and final step involves modeling possible electronic level structures and simulating its optical dynamics to compare with experimental observations. There are two approaches - solving rate equations describing the dynamics analytically or performing numerical simulations. Analytical approach has limitations where higher level or complex models are challenging to solve. A simpler but iterative approach is to perform numerical simulations as used in this thesis by simulating the possible models.

D.2. Automated Processing

The steps 1 to 3 discussed in the previous section involves several large data sets. The first step involves automated data acquisition of photon correlations as a function of excitation power and wavelength and thus involves a large number of data sets for each QE. The second step involves processing each data set that can be a single or multiple measurements as a function of one free parameter such as excitation power or wavelength. Depending on the amount of data and processing parameters such as bin size used, the processing time can be a few to tens of minutes. Accounting for several such data sets the processing time can add up to several hours for each QE. The processing can be done for each data set one at a time. However, that is time consuming and has limitations because the user has to manually step through the process and it is prone to user error. To speed-up as well as scale the processing step, all data sets for a single QE are supplied together to a custom developed function in MATLAB. At the end, the function outputs all processed data sets. The function is set up to use parallel computing to speed-up the processing. This automated approach has multiple advantages - it frees up several hours of user manually running through the processing and speeds it up by 4-5 \times . This automated processing is done twice - first for processing the data for shorter times (linear timescale) and second for processing the data over longer times (logarithmic timescale). The processing steps are represented in Fig. 33 as autocorrelation at short and long delay times (or linear and logarithmic scales).

D.3. Adaptive Fitting

After each data processing step, the data are modeled using empirical fits as represented in



Figure 33: Procedure for Autocorrelation Data Processing and Empirical Fitting

Fig. 33. Empirical fits to the linear scale or short timescale data are performed to obtain antibunching parameters. Empirical fits to the logarithmic scale or long timescale data are performed to primarily obtain bunching parameters. However, the multiple exponential nature of the data requires rigorous fitting procedure to ensure accurate modeling of the data. Thus, an adaptive fitting procedure was developed as part of this thesis. As discussed in Chapter 4-5, empirical models up to $n = 5$ were used. This translates to 3 free parameters for $n = 2$ and 11 free parameters for $n = 5$ where the resultant best-fit parameters vary by several orders of magnitude. The adaptive fitting of the empirical fits (Eq. 4.7) is a fitting routine developed that self adapts to the autocorrelation data. It first starts with the simplest model, $n = 2$. The fitting procedure is designed to automatically determine good starting parameters for the fitting routine so that the boundary conditions are reasonable and the fitting procedure is able to find a global minima. From $n = 2$, adaptive fitting proceeds to next highest model, $n = 3$. Here, it uses the best-fit results from the previous fit, $n = 2$ as starting parameters but slightly perturbs it so that it is not strictly the global minima. The process continues until $n = 5$, or the highest model requested by the user. At each step, iterations are implemented as necessary if the fitting procedure fails. The user also has an option to provide starting parameters as well as other conditions as deemed necessary. In the absence of user inputs, the fitting routine is designed to be able to self

adapt to the data. In the final step, AIC (see Section 4.5) and reduced chi-squared statistic is used to determine global best-fit model for data sets of a QE.

APPENDIX E: Optical Dynamics - Supporting Information

E.1. Nitrogen Vacancy Center in Diamond

For most QEs characterized by direct optical transition between a ground and optically excited state, the antibunching rate as a function of excitation power is typically linear, where the zero-power intercept provides the inverse of the radiative lifetime and the slope relates the pumping power to excitation rate. This is the case for the NV center in diamond, for example. Figure 34 shows the antibunching rate, γ_1 as a function of excitation power for NV centers in two nanodiamonds. The nanodiamonds were dropcast on a silicon wafer and probed for single NV centers. The nanodiamond sample was studied in the same setup as the h-BN samples discussed in the main text. The data acquisition and analysis is as discussed in the main text (no IRF correction was performed). The data were acquired using green (532 nm) excitation. To check for linear dependence, the rates are fit using Eq. 6a. The zero-power intercept is calculated to be 51 MHz (NV in ND1) and 67 MHz (NV in ND2), which agrees with the inverse optical lifetimes for NV centers in nanodiamonds reported in the literature [21].

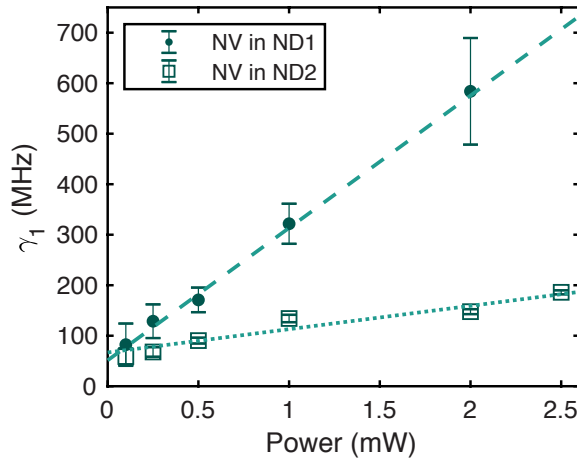


Figure 34: Antibunching Rate of NV Centers in Nanodiamonds. The antibunching rate (denoted by circles and squares) is measured as a function of excitation power. The lines (dashed and dotted) are fits to the rates. The error bars represent one standard deviation.

E.2. Antibunching Amplitude

Figures 35(a-e) presents the excitation power dependence of the antibunching amplitude, C_1 , of the QEs. Figure 35(f) presents the simulated antibunching amplitude for spontaneous and pumped transition mechanisms. The dashed lines are fits using the first order saturation model (Eq. 6b). The fit results are shown in Table 7.

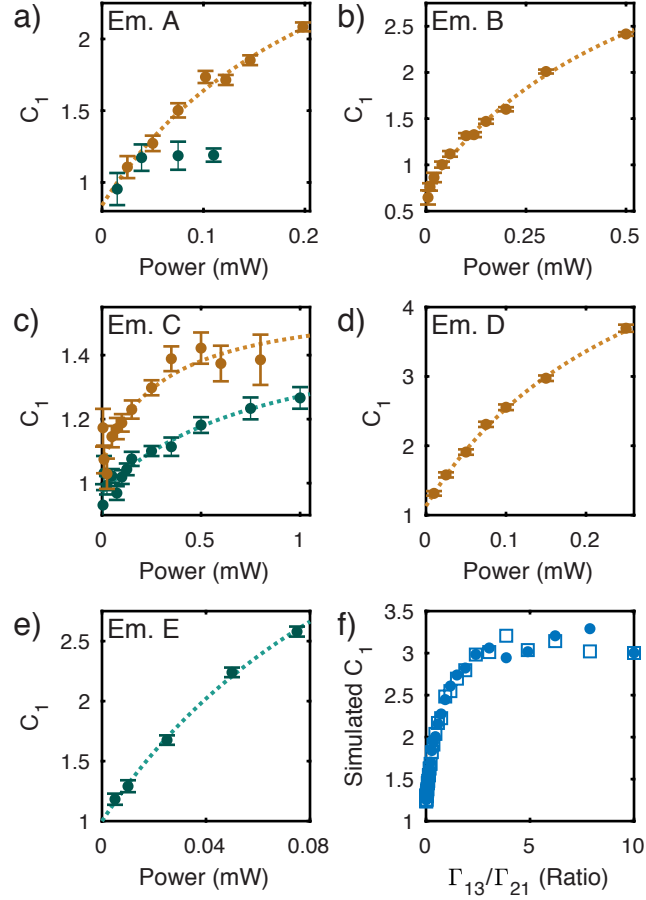


Figure 35: Antibunching Amplitudes. (a-e) Antibunching amplitudes (circles) of QEs A to E. The error bars represent one standard deviation. The dashed lines are fits using an empirical model discussed in the text. (f) Simulated antibunching amplitudes as a function of excitation rate for spontaneous (circles) and pumped (squares) transition mechanism discussed in the main text.

E.3. Quantum Emitter A

E.3.1. Extra Bunching Timescale

Under orange excitation, QE A is best modeled by 4 timescales ($n = 4$). Figure 36 shows the bunching rate, γ_4 , and amplitude, C_4 .

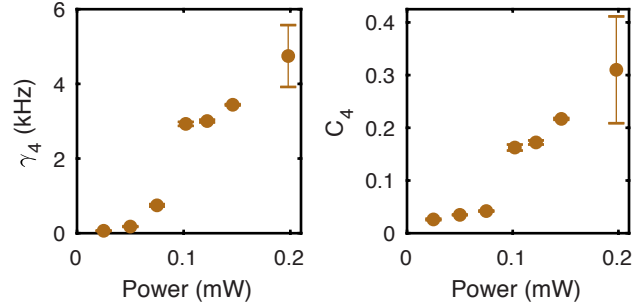


Figure 36: Quantum emitter A: γ_4 and C_4 for orange excitation. The error bars denote one standard deviation.

E.3.2. Lifetime Measurement

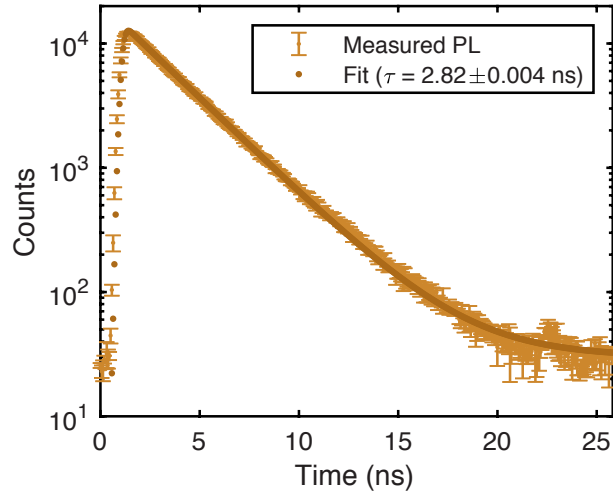


Figure 37: Quantum Emitter A: Lifetime Measurement. Time-resolved PL (light orange circles) and fit (dark orange circle) to the data. The error bars represent one standard deviation.

Figure 37 shows time-resolved PL of QE A. Time-resolved PL is acquired by using a pulsed laser (NKT Photonics, Fianium Whitelase) with the excitation wavelength centered ~ 580 nm and a 40 MHz pulse rate. The PL is recorded in histogram mode using a TCSPC module (PicoQuant, PicoHarp 300). The lifetime is obtained by fitting the convolution of

the IRF and an empirical model, $\text{IRF} * (A \exp(-t/\tau) + B)$. The IRF is obtained in same configuration as the time-resolved PL of the QE. The measured lifetime is 2.82 ± 0.004 ns, corresponding to a decay rate of 355 MHz.

E.3.3. Simulating Optical Dynamics

Figure 38 shows the result of simulations to recreate the observed optical dynamics of QE A. The same model discussed in the main text is used in the simulations (Fig. 13(a)). The radiative and nonradiative rates are chosen such that the resultant dynamics best recreates the observed optical dynamics of QE A (1st column of Fig. 12). There are two important qualitative features of simulating QE A that differ from the simulations presented in Fig. 13 of the main text. The first is that when $\kappa_{32} < \Gamma_{21}$, we find that the observed antibunching rate, γ_1 , is less than the spontaneous emission rate, Γ_{21} , over a wide range of power settings. Here, $\Gamma_{21} = 300$ MHz and $\kappa_{32} = 60$ MHz. The second important feature of simulating QE A is that the nonradiative transition mechanism involves both the spontaneous and optically pumped components. The nonradiative rates κ_{24} and κ_{41} are given the following form:

$$\kappa_{ij} = \kappa_{ij,0} + \beta_{ij} \frac{\Gamma_{13}}{\Gamma_{21}} \quad (\text{E.1})$$

where $\kappa_{ij,0}$ is the spontaneous emission rate, and β_{ij} is a scaling factor for the optically pumped transition, giving the corresponding transition rate at saturation when $\Gamma_{13} = \Gamma_{21}$. Here, we set $\kappa_{24,0} = 24$ kHz, $\kappa_{41,0} = 18$ kHz, $\beta_{24} = 9$ kHz, and $\beta_{41} = 3$ kHz. The combination of spontaneous and pumped transition quantitatively reproduces the non-zero offset of the bunching rate and the quasi-linear power scaling.

E.4. Simulating Optical Dynamics for Non-Zero Ratio of Pumping Rates

Figure 39 presents result of simulations for $\Gamma_{12}/\Gamma_{13} = [0, 2]$, for the case of spontaneous transition via level 4. As highlighted in the main text, the result of simulations for different Γ_{12}/Γ_{13} are qualitatively similar.

E.5. Empirical Fits to Photon Emission Statistics

Table 6 and 7 summarize the results of fits in Fig. 12 and Fig. 35.

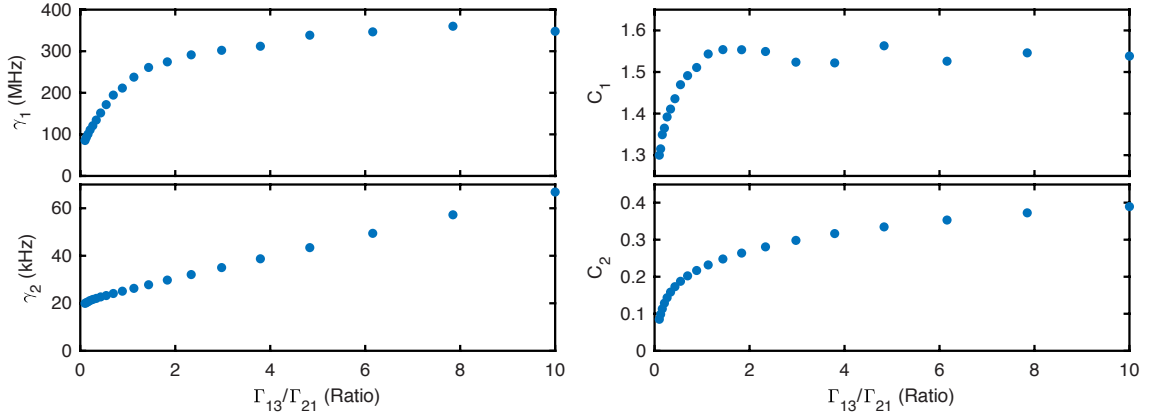


Figure 38: Simulating Optical Dynamics of QE A. Antibunching and bunching parameters resulting from simulation of the model discussed in main text by setting the radiative and nonradiative rates to best recreate the observed optical dynamics of QE A. The simulation is using the parameters discussed in the text: $\Gamma_{21} = 300$ MHz, $\Gamma_{32} = 60$ MHz, $\Gamma_{12} = 0$ MHz, $\kappa_{24,0} = 24$ kHz, $\beta_{24} = 9$ kHz, $\kappa_{41,0} = 18$ kHz and $\beta_{41} = 3$ kHz. The results are plotted as a function of Γ_{13}/Γ_{21} , where Γ_{21} is a fixed parameter.

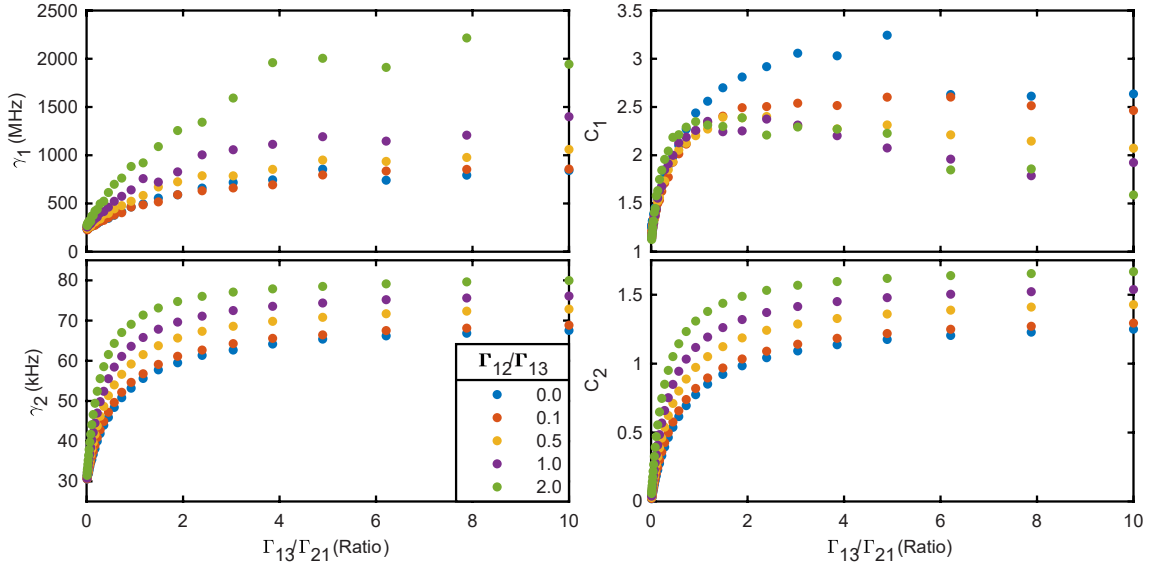


Figure 39: Simulation of Optical Dynamics for Different Γ_{12}/Γ_{13} . Antibunching and bunching parameters resulting from simulation of the model discussed in main text for Γ_{12} as a factor of Γ_{13} for spontaneous transition. Simultaneous excitation to level 2 and level 3 takes place at different rates which is ratio of the two rates.

Table 6: Results of Fitting Empirical Functions in Eq. 5.3a - 5.3d to PECS: Rates

QE	A	B	C	D	E
γ_1	532 nm: <u>1st Order Saturation</u> $R_0 = 0.00 \pm 261.5$ MHz $R_{sat} = 426.9 \pm 230.6$ MHz $P_{sat} = 17.23 \pm 23.90$ μ W 592 nm: <u>Saturation</u> $R_0 = 0.00 \pm 167.4$ MHz $R_{sat} = 411.4 \pm 154.1$ MHz $P_{sat} = 26.32 \pm 20.10$ μ W	592 nm: <u>1st Order Saturation</u> $R_0 = 276.6 \pm 1.0$ MHz $R_{sat} = 156.5 \pm 2.19$ MHz $P_{sat} = 135.8 \pm 7.23$ MHz/ μ W	532 nm: <u>2nd Order Saturation</u> $R_0 = 452.0 \pm 47.1$ MHz $m_0 = 3.06 \pm 3.32$ MHz/ μ W $m_1 = 0.3 \pm 0.07$ MHz/ μ W ² $P_{sat} = 52.2 \pm 60.8$ μ W 592 nm: <u>2nd Order Saturation</u> $R_0 = 502.3 \pm 46.8$ MHz $m_0 = 4.48 \pm 2.84$ MHz/ μ W $m_1 = 0.1 \pm 0.1$ MHz/ μ W ² $P_{sat} = 75.3 \pm 57.2$ μ W	592 nm: <u>Linear</u> $R_0 = 135.8 \pm 4.7$ MHz $m_0 = 0.18 \pm 0.03$ MHz/ μ W	532 nm: <u>Linear</u> $R_0 = 227.7 \pm 12.5$ MHz $m_0 = 1.0 \pm 0.24$ MHz/ μ W
γ_2	592 nm: <u>Linear</u> $R_0 = 16.7 \pm 0.4$ kHz $m_0 = 0.15 \pm 0.005$ kHz/ μ W	592 nm: <u>2nd Order Saturation</u> $R_0 = 0.0 \pm 9.87$ kHz $m_0 = 3.13 \pm 7.02$ kHz/ μ W $m_1 = 0.0363 \pm 0.0028$ kHz/ μ W ² $P_{sat} = 3.66 \pm 5.29$ μ W	532 nm: <u>1st Order Saturation</u> $R_0 = 0.0 \pm 4.3$ MHz $R_{sat} = 24.1 \pm 4.3$ MHz $P_{sat} = 119.4 \pm 40.8$ μ W 592 nm: <u>1st Order Saturation</u> $R_0 = 0.0 \pm 0.8$ MHz $R_{sat} = 328.5 \pm 4.2$ MHz $P_{sat} = 1177.2 \pm 32.7$ μ W	592 nm: <u>Linear</u> $R_0 = 1.74 \pm 0.08$ kHz $m_0 = 0.02 \pm 0.001$ kHz/ μ W	532 nm: <u>Linear</u> $R_0 = 3.07 \pm 0.02$ MHz $m_0 = 0.06 \pm 0.004$ kHz/ μ W
γ_3	592 nm: <u>Quadratic</u> $R_0 = 1.4 \pm 1.4$ kHz $m_0 = 0.00 \pm 0.03$ kHz/ μ W $m_1 = 0.0007 \pm 0.0001$ kHz/ μ W ²	592 nm: <u>2nd Order Saturation</u> $R_0 = 0.0 \pm 0.63$ kHz $m_0 = 1.10 \pm 0.43$ kHz/ μ W $m_1 = 0.0076 \pm 0.0001$ kHz/ μ W ² $P_{sat} = 3.01 \pm 0.66$ μ W	532 nm: <u>1st Order Saturation</u> $R_0 = 0.0 \pm 0.6$ kHz $R_{sat} = 4336.2 \pm 2.8$ kHz $P_{sat} = 540.0 \pm 0.8$ μ W 592 nm: <u>1st Order Saturation</u> $R_0 = 0.0 \pm 0.2$ kHz $R_{sat} = 2815.4 \pm 61.8$ kHz $P_{sat} = 1550.4 \pm 42.2$ μ W	592 nm: <u>Linear</u> $R_0 = 0.82 \pm 0.03$ kHz $m_0 = 0.002 \pm 0.000$ kHz/ μ W	532 nm: <u>Quadratic</u> $R_0 = 0.00 \pm 1.05$ kHz $m_0 = 0.211 \pm 0.075$ kHz/ μ W $m_1 = 0.004 \pm 0.0009$ kHz/ μ W ²

Table 7: Results of Fitting Empirical Functions in Eq. 5.3a - 5.3d to PECS: Amplitudes

QE	A	B	C	D	E
C₁	592 nm: <u>1st Order</u> <u>Saturation</u> $R_0 = 0.84 \pm 0.13$ $R_{sat} = 2.74 \pm 0.6$ $P_{sat} = 241.95 \pm 128.4 \mu\text{W}$	592 nm: <u>1st Order</u> <u>Saturation</u> $R_0 = 0.74 \pm 0.03$ $R_{sat} = 3.75 \pm 0.25$ $P_{sat} = 617.5 \pm 78.5 \mu\text{W}$	532 nm: <u>1st Order</u> <u>Saturation</u> $R_0 = 0.97 \pm 0.02$ $R_{sat} = 0.55 \pm 0.16$ $P_{sat} = 841.0 \pm 483.5 \mu\text{W}$ 592 nm: <u>1st Order</u> <u>Saturation</u> $R_0 = 1.06 \pm 0.03$ $R_{sat} = 0.53 \pm 0.1$ $P_{sat} = 304.4 \pm 148.5 \mu\text{W}$	592 nm: <u>1st Order</u> <u>Saturation</u> $R_0 = 1.13 \pm 0.04$ $R_{sat} = 5.45 \pm 0.47$ $P_{sat} = 284.84 \pm 44.06 \mu\text{W}$	532 nm: <u>1st Order</u> <u>Saturation</u> $R_0 = 1.0 \pm 0.06$ $R_{sat} = 4.49 \pm 1.11$ $P_{sat} = 136.17 \pm 54.55 \mu\text{W}$
C₂	592 nm: <u>1st Order</u> <u>Saturation</u> $R_0 = 0.0 \pm 1.82$ $R_{sat} = 0.95 \pm 4.15$ $P_{sat} = 137.4 \pm 1745.8 \mu\text{W}$	592 nm: <u>Linear</u> $R_0 = 0.029 \pm 0.416$ $m_0 = 0.0028 \pm 0.0021 \mu\text{W}^{-1}$	532 nm: <u>Linear</u> $R_0 = 0.000 \pm 0.004$ $m_0 = 0.00016 \pm 0.00001 \mu\text{W}^{-1}$ 592 nm: <u>1st Order</u> <u>Saturation</u> $R_0 = 0.0 \pm 0.84$ $R_{sat} = 0.32 \pm 2.82$ $P_{sat} = 799.3 \pm 18276.6 \mu\text{W}$	592 nm: <u>1st Order</u> <u>Saturation</u> $R_0 = 0.0 \pm 0.02$ $R_{sat} = 5.59 \pm 0.29$ $P_{sat} = 321.0 \pm 27.8 \mu\text{W}$	532 nm: <u>Linear</u> $R_0 = 0.065 \pm 0.012$ $m_0 = 0.017 \pm 0.000 \mu\text{W}^{-1}$
C₃	592 nm: <u>1st Order</u> <u>Saturation</u> $R_0 = 0.0 \pm 0.017$ $R_{sat} = 0.252 \pm 0.015$ $P_{sat} = 21.52 \pm 3.06 \mu\text{W}$	592 nm: <u>1st Order</u> <u>Saturation</u> $R_0 = 0.0 \pm 0.0013$ $R_{sat} = 0.259 \pm 0.002$ $P_{sat} = 81.53 \pm 2.25 \mu\text{W}$	532 nm: <u>1st Order</u> <u>Saturation</u> $R_0 = 0.004 \pm 0.574$ $R_{sat} = 0.27 \pm 3.34$ $P_{sat} = 581.9 \pm 17034.4 \mu\text{W}$ 592 nm: <u>1st Order</u> <u>Saturation</u> $R_0 = 0.004 \pm 0.0004$ $R_{sat} = 0.531 \pm 0.002$ $P_{sat} = 163.6 \pm 2.3 \mu\text{W}$	592 nm: <u>1st Order</u> <u>Saturation</u> $R_0 = 0.0 \pm 0.35$ $R_{sat} = 0.20 \pm 0.35$ $P_{sat} = 3.29 \pm 7.65 \mu\text{W}$	532 nm: <u>1st Order</u> <u>Saturation</u> $R_0 = 0.0042 \pm 0.0006$ $R_{sat} = 1.85 \pm 0.1$ $P_{sat} = 251.56 \pm 16.45 \mu\text{W}$

E.6. Generalized Electronic Level Structure

Figure 40 generalizes the electronic level structure and transition diagram discussed in Section 5.5. The general version shows how effective transitions that are proportional to optical pumping power (e.g., optically pumped transitions κ_{24} and κ_{41}) can result from combinations of other possible transitions such as re-pumping from level 2 \rightarrow 3 with rate Γ_{23} , re-pumping from level 4 \rightarrow 3 with rate Γ_{43} and nonradiative transition from level 3 \rightarrow 4 with rate κ_{34} .

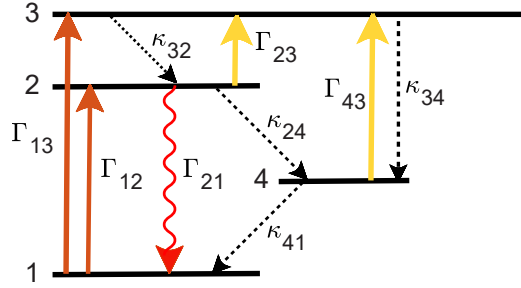


Figure 40: General Electronic Level Structure.

E.7. Theoretical Calculations

We perform first-principles density-functional theory calculations as implemented in the VASP code [119, 120]. We utilize the hybrid functional of Heyd, Scuseria, and Ernzerhof [91, 92] to ensure accurate energetics, electronic structure, and atomic geometries. The fraction of Hartree-Fock exchange is set to 40%, consistent with previous studies [197, 200]. A plane-wave basis with projector augmented-wave potentials [24] is used, and the energy cutoff for the basis is set to 520 eV.

The boron dangling bond is modeled in a 240-atom supercell with volume 2110 Å³ within periodic boundary conditions [72]. A single, special \mathbf{k} -point (0.25, 0.25, 0.25) is used to sample the Brillouin zone. Lattice vectors are held fixed while the atomic forces are relaxed to below 0.01 eV/Å. To calculate the nonradiative capture coefficient, we utilize the formalism of Ref. [9] implemented in the Nonrad code [198].

E.7.1. Calculation of the capture coefficient for the boron dangling bond

We calculate the nonradiative capture coefficient C_n for the capture of an electron from the conduction band into the boron dangling bond using the formalism implemented in the Nonrad code [198]. We will focus on the ground state [level 1 in Fig. 5(a)] and the optically active excited state [level 2 in Fig. 5(a)] of the dangling bond, which are separated by 2.06 eV [197]. In equilibrium, the dangling bond is in the negative charge state and is occupied by two electrons. When the excitation energy is sufficiently large, an electron can be excited into the conduction band and the dangling bond is photoionized, changing the charge state from negative to neutral [process Γ_{13} in Fig. 5(a)]. Subsequent re-capture of this electron returns the dangling bond to the negative charge state. We consider two potential scenarios for this nonradiative process mediated by electron-phonon coupling: (1)

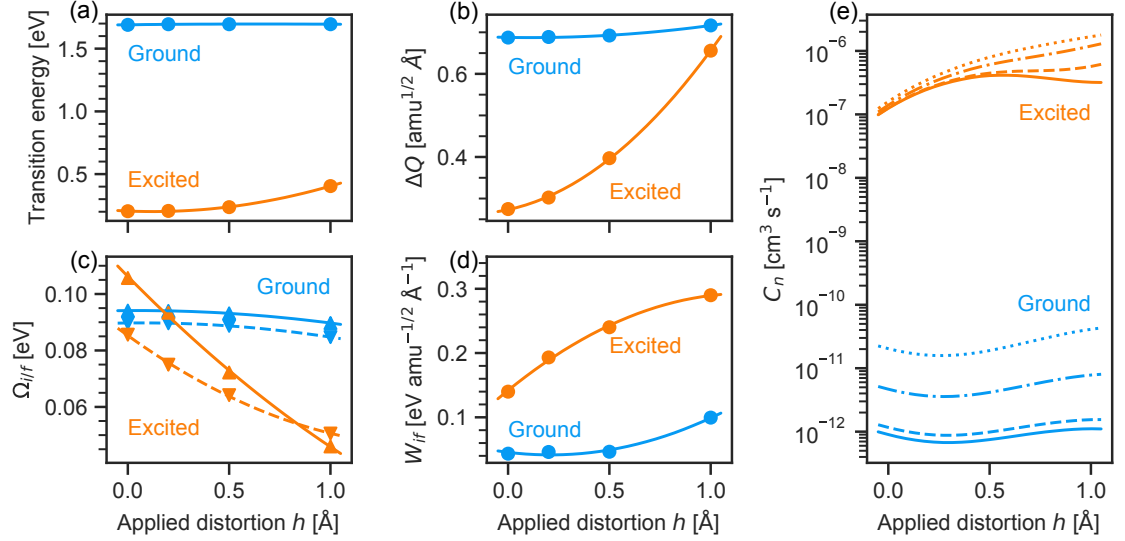


Figure 41: Calculated Parameters and Capture Coefficient for Capture of an Electron from the Conduction Band into the Neutral Boron Dangling Bond, as a Function of Applied Distortion h . Calculated (a) transition energy, (b) mass-weighted root-mean-square difference in atomic geometries, (c) initial (up triangle) and final (down triangle) phonon frequencies, and (d) electron-phonon coupling matrix elements. The lines are a quadratic fit to the calculated parameters and are intended to guide the eye. The calculated (e) electron capture coefficient at 10 K (solid), 300 K (dashed), 600 K (dashed dotted), and 900 K (dotted). The parameters for capture into the ground state are shown in blue and the excited state are shown in orange.

The electron is captured directly into the ground state of the dangling bond, with rate κ_{31} [not depicted in Fig. 5(a)], or (2) the electron is captured into the excited state of the dangling bond [κ_{32} in Fig. 5(a)]. Process (2) puts the defect in the optically active excited state, from which a photon can then be emitted, with an emissive dipole unaligned with the absorptive dipole.

To evaluate the nonradiative capture coefficients, we extract several parameters from our density-functional theory calculations: the transition energy, the mass-weighted root-mean-square difference in atomic geometries ΔQ , the phonon frequencies in the initial (i) and final (f) states $\Omega_{i/f}$, and the electron-phonon coupling matrix element W_{if} . The transition level for capture into excited state, which is used to determine the transition energy, is above the conduction-band minimum, while the single-particle states are in the gap. For the purposes of our capture coefficient evaluation, we shift the transition energy to be consistent with the 200 meV difference observed experimentally [104]; we verified that the conclusions are insensitive to the choice of the energy shift. The degeneracy factor in the nonradiative rate [198] is set to 1 since the dangling bond does not possess any configurational degeneracy. A scaling factor that accounts for charged defect interactions [see Sec. III. E. of Ref. [9]] is not necessary in this case because capture occurs in the neutral charge state and the electron-phonon coupling is evaluated in the neutral charge state.

At room temperature, we calculate C_n for capture into the ground state to be $1.2 \times 10^{-12} \text{ cm}^3 \text{ s}^{-1}$ and into the excited state to be $1.2 \times 10^{-7} \text{ cm}^3 \text{ s}^{-1}$. We can thus safely assume that capture into the excited state will dominate. These capture coefficients are larger than typical radiative capture coefficients, which are on the order of $10^{-13} - 10^{-14} \text{ cm}^3 \text{ s}^{-1}$ [59], justifying our implicit assumption of nonradiative rather than radiative capture.

Previous work has already demonstrated that out-of-plane distortions are important for understanding both the symmetry [197] and transition rates [200] of the boron dangling bond. Here we include the effect of out-of-plane distortions on the capture coefficient, following the methodology of Ref. [200]. In short, a plane neighboring the dangling bond

is bent to create a “bubble”, with the height of the bubble being referred to as the applied distortion h . The bubble induces an out-of-plane distortion in the dangling bond and allows us to study its effect on the capture coefficient. The influence of the out-of-plane distortion on the calculated parameters is shown in Fig. 41. For comparison purposes, we will use the average at room temperature $4 \times 10^{-7} \text{ cm}^3 \text{ s}^{-1}$ as a representative value for capture into the excited state.

BIBLIOGRAPHY

- [1] Abdi, M., Chou, J. P., Gali, A., & Plenio, M. B. 2018, *ACS Photonics*, 5, 1967
- [2] Abdi, M., Hwang, M.-J., Aghtar, M., & Plenio, M. B. 2017, *Physical Review Letters*, 119, 233601
- [3] Abobeih, M. H. et al. 2019, *Nature*, 576, 411
- [4] Aharonovich, I., Englund, D., & Toth, M. 2016, *Nature Photonics*, 10, 631
- [5] Aharonovich, I. & Toth, M. 2017, *Science*, 358, 170
- [6] Akbari, H., Lin, W.-H., Vest, B., Jha, P. K., & Atwater, H. A. 2021, *Physical Review Applied*, 15, 014036
- [7] Alcántara Ortigoza, M. & Stolbov, S. 2022, *Physical Review B*, 105, 165306
- [8] Alem, N., Erni, R., Kisielowski, C., Rossell, M. D., Gannett, W., & Zettl, A. 2009, *Physical Review B*, 80, 155425
- [9] Alkauskas, A., Yan, Q., & Van de Walle, C. G. 2014, *Physical Review B*, 90, 75202
- [10] Andrei, E. Y., Katzir, A., & Suss, J. T. 1976, *Physical Review B*, 13, 2831
- [11] Ari, O., Polat, N., Fırat, V., Çakır, Ö., & Ates, S. 2018, arXiv preprint arXiv:1808.10611
- [12] Aslam, N. et al. 2017, *Science*, 357, 67
- [13] Atatüre, M., Englund, D., Vamivakas, N., Lee, S.-Y., & Wrachtrup, J. 2018, *Nature Reviews Materials*, 3, 38
- [14] Attacalite, C., Bockstedte, M., Marini, A., Rubio, A., & Wirtz, L. 2011, *Physical Review B*, 83, 144115
- [15] Auburger, P. & Gali, A. 2021, *Physical Review B*, 104, 075410
- [16] Awschalom, D. D., Bassett, L. C., Dzurak, A. S., Hu, E. L., & Petta, J. R. 2013, *Science*, 339, 1174
- [17] Awschalom, D. D., Hanson, R., Wrachtrup, J., & Zhou, B. B. 2018, *Nature Photonics*, 12, 516
- [18] Baber, S., Malein, R. N. E., Khatri, P., Keatley, P. S., Guo, S., Withers, F., Ramsay, A. J., & Luxmoore, I. J. 2022, *Nano Letters*, 22, 461
- [19] Basha Dhu-al-jalali wal, A. & Palla, P. 2021, *Scientific Reports*, 11

- [20] Bassett, L. C., Alkauskas, A., Exarhos, A. L., & Fu, K.-M. C. 2019, *Nanophotonics*, 8, 1867
- [21] Berthel, M., Mollet, O., Dantelle, G., Gacoin, T., Huant, S., & Drezet, A. 2015, *Physical Review B*, 91, 035308
- [22] Berzina, B., Korsaks, V., Trinkler, L., Sarakovskis, A., Grube, J., & Bellucci, S. 2016, *Diamond & Related Materials*, 68, 131
- [23] Bhang, J., Ma, H., Yim, D., Galli, G., & Seo, H. 2021, *ACS Applied Materials & Interfaces*, 13, 45768
- [24] Blöchl, P. E. 1994, *Physical Review B*, 50, 17953
- [25] Block, M. et al. 2021, *Physical Review Applied*, 16, 024024
- [26] Boll, M. K., Radko, I. P., Huck, A., & Andersen, U. L. 2020, *Optics Express*, 28, 7475
- [27] Bommer, A. & Becher, C. 2019, *Nanophotonics*, 8, 2041
- [28] Bourrellier, R. et al. 2016, *Nano Letters*, 16, 4317
- [29] Bradley, C. E. et al. 2019, *Physical Review X*, 9, 031045
- [30] Breitweiser, S. A., Exarhos, A. L., Patel, R. N., Saouaf, J., Porat, B., Hopper, D. A., & Bassett, L. C. 2020, *ACS Photonics*, 7, 288
- [31] Brouri, R., Beveratos, A., Poizat, J.-P., & Grangier, P. 2000, *Physical Review A*, 62, 063817
- [32] Buluta, I., Ashhab, S., & Nori, F. 2011, *Reports on Progress in Physics*, 74, 104401
- [33] Caldwell, J. D., Aharonovich, I., Cassabois, G., Edgar, J. H., Gil, B., & Basov, D. N. 2019, *Nature Reviews Materials*, 4, 552–567
- [34] Camphausen, R., Marini, L., Tawfik, S. A., Tran, T. T., Ford, M. J., & Palomba, S. 2020, *APL Photonics*, 5, 076103
- [35] Cao, S., Jin, Y., Dong, H., Guo, T., He, J., & He, S. 2021, *J. Phys. Mater.*, 4, 035001
- [36] Cassabois, G., Valvin, P., & Gil, B. 2016, *Nature Photonics*, 10, 262
- [37] Chakraborty, C., Vamivakas, N., & Englund, D. 2019, *Nanophotonics*, 8, 2017
- [38] Chejanovsky, N. et al. 2017, *Scientific Reports*, 7
- [39] —. 2021, *Nature Materials*, 20, 1079
- [40] —. 2016, *Nano Letters*, 16, 7037

- [41] Chen, Y. et al. 2021, ACS Applied Materials & Interfaces, 13, 47283
- [42] Chen, Y. & Quek, S. Y. 2021, The Journal of Physical Chemistry C, 125, 21791
- [43] Chen, Y. et al. 2020, ACS Applied Materials and Interfaces, 12, 25464
- [44] Choi, S. et al. 2016, ACS Applied Materials & Interfaces, 8, 29642
- [45] Cirac, J. I. & Zoller, P. 1995, Physical Review Letters, 74, 4091
- [46] Comtet, J. et al. 2019, Nano Letters, 19, 2516
- [47] Cretu, O., Ishizuka, A., Yanagisawa, K., Ishizuka, K., & Kimoto, K. 2021, ACS Nano, 15, 5316
- [48] Dai, S. et al. 2014, Science, 343, 1125
- [49] Davies, G. 1974, Journal of Physics C : Solid State Physics, 7, 3797
- [50] de Leon, N. P. et al. 2021, Science, 372, eabb2823
- [51] Degen, C. L., Reinhard, F., & Cappellaro, P. 2017, Reviews of Modern Physics, 89, 035002
- [52] Dev, P. 2020, Physical Review Research, 2, 022050
- [53] Devoret, M. H. & Schoelkopf, R. J. 2013, Science, 339, 1169
- [54] Dietrich, A. et al. 2018, Physical Review B, 98, 081414
- [55] Dietrich, A., Doherty, M. W., Aharonovich, I., & Kubanek, A. 2020, Physical Review B, 101, 081401
- [56] Doherty, M. W., Du, C. R., & Fuchs, G. D. 2022, Journal of Applied Physics, 131, 010401
- [57] Doherty, M. W., Manson, N. B., Delaney, P., Jelezko, F., Wrachtrup, J., & Hollenberg, L. C. L. 2013, Physics Reports, 528, 1
- [58] Dowling, J. P. & Milburn, J. 2003, Philosophical Transactions of the Royal Society of London A, 361, 1655
- [59] Dreyer, C. E., Alkauskas, A., Lyons, J. L., & de Walle, C. G. 2020, Physical Review B, 102, 85305
- [60] Duong, N. M. H. et al. 2018, ACS Applied Materials & Interfaces, 10, 24886
- [61] —. 2019, Nano Letters, 19, 5417

- [62] Eftekhari, Z., Ghobadi, A., Soydan, M. C., Yildirim, D. U., Cinel, N., & Ozbay, E. 2021, *Optics Letters*, 46, 1664
- [63] Elshaari, A. W. et al. 2021, *Advanced Quantum Technologies*, 4, 2100032
- [64] Epstein, R. J., Mendoza, F. M., Kato, Y. K., & Awschalom, D. D. 2005, *Nature Physics*, 1, 94
- [65] Exarhos, A. L., Hopper, D. A., Grote, R. R., Alkauskas, A., & Bassett, L. C. 2017, *ACS Nano*, 11, 3328
- [66] Exarhos, A. L., Hopper, D. A., Patel, R. N., Doherty, M. W., & Bassett, L. C. 2019, *Nature Communications*, 10, 222
- [67] Feldman, M. A., Marvinney, C. E., Puretzky, A. A., & Lawrie, B. J. 2021, *Optica*, 8, 1
- [68] Feng, J., Deschout, H., Caneva, S., Hofmann, S., Lončarić, I., Lazić, P., & Radenovic, A. 2018, *Nano Letters*, 18, 1739
- [69] Fischer, M. et al. 2021, *Science Advances*, 7, 7138
- [70] Fishman, R. E. K., Patel, R. N., Hopper, D. A., Huang, T.-Y., & Bassett, L. C. 2021, arXiv preprint arXiv:2111.01252
- [71] Fournier, C. et al. 2021, *Nature Communications*, 12, 3779
- [72] Freysoldt, C., Grabowski, B., Hickel, T., Neugebauer, J., Kresse, G., Janotti, A., & de Walle, C. G. 2014, *Reviews of Modern Physics*, 86, 253
- [73] Fröch, J. E., Kim, S., Mendelson, N., Kianinia, M., Toth, M., & Aharonovich, I. 2020, *ACS nano*, 14, 7085
- [74] Fröch, J. E. et al. 2021, *Nano Letters*, 21, 6549
- [75] Gao, S., Chen, H. Y., & Bernardi, M. 2021, *npj Computational Materials*, 7
- [76] Gao, X. et al. 2021, *Nano Letters*, 21, 7708
- [77] Gao, X., Pandey, S., Kianinia, M., Ahn, J., Ju, P., Aharonovich, I., Shivaram, N., & Li, T. 2021, *ACS Photonics*, 8, 994
- [78] Gao, X. et al. 2022, arXiv preprint arXiv:2203.13184
- [79] Gisin, N. & Thew, R. 2007, *Nature Photonics*, 1, 165
- [80] Glushkov, E. et al. 2021, *ACS Photonics*, 8, 2033
- [81] Gottscholl, A. et al. 2021, *Nature Communications*, 12

- [82] —. 2021, *Science Advances*, 7, eabf3630
- [83] —. 2020, *Nature Materials*, 19, 540
- [84] Grosso, G. et al. 2020, *ACS Photonics*, 7, 1410
- [85] —. 2017, *Nature Communications*, 8
- [86] Guo, N.-J. et al. 2022, *ACS Omega*, 7, 1733
- [87] Hamdi, H., Thiering, G., Bodrog, Z., Ivády, V., & Gali, A. 2020, *npj Computational Materials*, 6
- [88] Hayee, F. et al. 2020, *Nature Materials*, 19, 534
- [89] Hensen, B. et al. 2015, *Nature*, 526, 682
- [90] Hernández-Mínguez, A., Lähnemann, J., Nakhaie, S., Lopes, J. M., & Santos, P. V. 2018, *Physical Review Applied*, 10, 044031
- [91] Heyd, J., Scuseria, G. E., & Ernzerhof, M. 2003, *The Journal of Chemical Physics*, 118, 8207
- [92] —. 2006, *The Journal of Chemical Physics*, 124, 219906
- [93] Hoese, M., Reddy, P., Dietrich, A., Koch, M. K., Fehler, K. G., Doherty, M. W., & Kubanek, A. 2020, *Science Advances*, 6, eaba6038
- [94] Hopper, D. A., Shulevitz, H. J., & Bassett, L. C. 2018, *Micromachines*, 9, 437
- [95] Hou, S. et al. 2018, *2D Materials*, 5, 015010
- [96] Huang, Y., Sutter, E., Shi, N. N., Zheng, J., Yang, T., Englund, D., Gao, H.-J., & Sutter, P. 2015, *ACS Nano*, 9, 10612
- [97] Huber, S. P., Gullikson, E., Van De Kruijs, R. W. E., Bijkerk, F., & Prendergast, D. 2015, *Physical Review B*, 92, 245310
- [98] Iikawa, F., Hernández-Mínguez, A., Aharonovich, I., Nakhaie, S., Liou, Y. T., Lopes, J. M. J., & Santos, P. V. 2019, *Applied Physics Letters*, 114, 171104
- [99] Ivády, V., Barcza, G., Thiering, G., Li, S., Hamdi, H., Chou, J.-P., Legeza, Ö., & Gali, A. 2020, *npj Computational Materials*, 6, 1
- [100] Jara, C. et al. 2021, *Journal of Physical Chemistry A*, 125, 1325
- [101] Jelezko, F. & Wrachtrup, J. 2006, *Journal of Physics: Condensed Matter*, 18, 807

- [102] Jeong, K. Y., Lee, S. W., Choi, J. H., So, J. P., & Park, H. G. 2020, *Nanomaterials*, 10, 1
- [103] Jungwirth, N. R., Calderon, B., Ji, Y., Spencer, M. G., Flatte, M. E., & Fuchs, G. D. 2016, *Nano Letters*, 16, 6052
- [104] Jungwirth, N. R. & Fuchs, G. D. 2017, *Physical Review Letters*, 119, 057401
- [105] Kanai, S. et al. 2022, *PNAS*, 119, e2121808119
- [106] Katzir, A., Suss, J. T., Zunger, A., & Halperin, A. 1975, *Physical Review B*, 11, 2370
- [107] Khatri, P., Luxmoore, I. J., & Ramsay, A. J. 2019, *Physical Review B*, 100, 125305
- [108] Khatri, P., Ramsay, A. J., Malein, R. N. E., Chong, H. M., & Luxmoore, I. J. 2020, *Nano Letters*, 20, 4256
- [109] Kianinia, M. et al. 2018, *Nature Communications*, 9
- [110] Kianinia, M., White, S., Fröch, J. E., Bradac, C., & Aharonovich, I. 2020, *ACS Photonics*, 7, 2147
- [111] Kim, S. et al. 2019, *Advanced Optical Materials*, 7, 1901132
- [112] —. 2018, *Nature Communications*, 9
- [113] Kok, P., Munro, W. J., Nemoto, K., Ralph, T. C., Dowling, J. P., & Milburn, G. J. 2007, *Reviews of Modern Physics*, 79, 135
- [114] Konthasinghe, K., Chakraborty, C., Mathur, N., Qiu, L., Mukherjee, A., Fuchs, G. D., & Vamivakas, A. N. 2019, *Optica*, 6, 542
- [115] Koperski, M., Nogajewski, K., & Potemski, M. 2018, *Optics Communications*, 411, 158
- [116] Korona, T. & Chojecki, M. 2019, *International Journal of Quantum Chemistry*, 119, e25925
- [117] Koronski, K., Kaminska, A., Zhigadlo, N. D., Elias, C., Cassabois, G., & Gil, B. 2019, *Superlattices and Microstructures*, 131, 1
- [118] Krečmarová, M., Canet-Albiach, R., Pashaei-Adl, H., Gorji, S., Muñoz-Matutano, G., Nesládek, M., Martínez-Pastor, J. P., & Sánchez-Royo, J. F. 2021, *ACS Applied Materials & Interfaces*, 13, 46105
- [119] Kresse, G. & Furthmüller, J. 1996, *Computational Materials Science*, 6, 15
- [120] —. 1996, *Physical Review B*, 54, 11169

- [121] Lazić, S. et al. 2019, *Communications Physics*, 2
- [122] Li, C., Fröch, J. E., Nonahal, M., Tran, T. N., Toth, M., Kim, S., & Aharonovich, I. 2021, *ACS Photonics*, 8, 2966
- [123] Li, C., Xu, Z., Mendelson, N., Kianinia, M., Wan, Y., Toth, M., Aharonovich, I., & Bradac, C. 2020, *2D Materials*, 7, 045015
- [124] Li, C., Xu, Z. Q., Mendelson, N., Kianinia, M., Toth, M., & Aharonovich, I. 2019, *Nanophotonics*, 8, 2049
- [125] Li, K., Smart, T., & Ping, Y. 2021, arXiv preprint arXiv:2110.01787
- [126] Li, X., Scully, R. A., Shayan, K., Luo, Y., & Strauf, S. 2019, *ACS Nano*, 13, 6992
- [127] Li, X., Shepard, G. D., Cupo, A., Camporeale, N., Shayan, K., Luo, Y., Meunier, V., & Strauf, S. 2017, *ACS Nano*, 11, 6652
- [128] Linderälv, C., Wieczorek, W., & Erhart, P. 2021, *Physical Review B*, 103, 115421
- [129] Liu, H., You, C. Y., Li, J., Galligan, P. R., You, J., Liu, Z., Cai, Y., & Luo, Z. 2021, *Nano Materials Science*, 3, 291
- [130] Liu, W. et al. 2021, arXiv preprint arXiv:2101.11220
- [131] —. 2020, *Physica E: Low-Dimensional Systems and Nanostructures*, 124, 114251
- [132] López-Morales, G. I. et al. 2021, *Optical Materials Express*, 11, 3478
- [133] Lyu, C., Zhu, Y., Gu, P., Qiao, J., Watanabe, K., Taniguchi, T., & Ye, Y. 2020, *Applied Physics Letters*, 117, 244002
- [134] Maciaszek, M., Razinkovas, L., & Alkauskas, A. 2022, *Physical Review Materials*, 6, 014005
- [135] Mackoitis-Sinkeviciene, M., Maciaszek, M., Van De Walle, C. G., & Alkauskas, A. 2019, *Applied Physics Letters*, 115, 212101
- [136] Maradudin, A. A. 1966, *Solid State Physics*, 18, 273
- [137] Martinez, L. J., Peline, T., Waselowski, V., Maze, J. R., Gil, B., Cassabo, G., & Jacques, V. 2016, *Physical Review B*, 94, 121405
- [138] Mathur, N., Mukherjee, A., Gao, X., Luo, J., McCullian, B. A., Li, T., Vamivakas, A. N., & Fuchs, G. D. 2021, arXiv preprint arXiv:2112.06191
- [139] McDougall, N. L., Partridge, J. G., Nicholls, R. J., Russo, S. P., & McCulloch, D. G. 2017, *Physical Review B*, 96, 144106

- [140] Mendelson, N. et al. 2020, *Nature Materials*, 20, 321
- [141] Mendelson, N., Doherty, M., Toth, M., Aharonovich, I., & Tran, T. T. 2020, *Advanced Materials*, 32, 1908316
- [142] Mendelson, N., Xu, Z.-Q., Trong Tran, T., Kianinia, M., Scott, J., Bradac, C., Aharonovich, I., & Toth, M. 2019, *Nano Letters*, 13, 3132–3140
- [143] Meuret, S., Tizei, L. H. G., Cazimajou, T., Bourrellier, R., Chang, H. C., Treussart, F., & Kociak, M. 2015, *Physical Review Letters*, 114, 197401
- [144] Monazam, M. R. A., Ludacka, U., Komsa, H. P., & Kotakoski, J. 2019, *Applied Physics Letters*, 115, 071604
- [145] Monroe, C. 2002, *Nature*, 416, 238
- [146] Mu, Z. et al. 2022, *Physical Review Letters*, 128, 216402
- [147] Murzakhanov, F. F. et al. 2022, *Nano Letters*, 22, 2718
- [148] Na, Y. S. et al. 2021, *2D Materials*, 8, 045041
- [149] Narun, L. R., Fishman, R. E. K., Shulevitz, H. J., Patel, R. N., & Bassett, L. C. 2021, arXiv preprint arXiv:2112.05654
- [150] Neu, E., Agio, M., & Becher, C. 2012, *Optics Express*, 20, 19956
- [151] Nikolay, N. et al. 2019, *Optica*, 6, 1084
- [152] Nikolay, N., Mendelson, N., Sadzak, N., Böhm, F., Tran, T. T., Sontheimer, B., Aharonovich, I., & Benson, O. 2019, *Physical Review Applied*, 11, 041001
- [153] Noh, G., Choi, D., Kim, J.-H., Im, D.-G., Kim, Y.-H., Seo, H., & Lee, J. 2018, *Nano Letters*, 18, 4710
- [154] Palombo Blascetta, N., Liebel, M., Lu, X., Taniguchi, T., Watanabe, K., Efetov, D. K., & Van Hulst, N. F. 2020, *Nano Letters*, 20, 1992
- [155] Patel, R. N. et al. 2022, arXiv preprint arXiv:2201.08881
- [156] Peline, T. et al. 2019, *Physical Review Materials*, 3, 094001
- [157] Pham, T., Gibb, A. L., Li, Z., Gilbert, S. M., Song, C., Louie, S. G., & Zettl, A. 2016, *Nano Letters*, 16, 7142
- [158] Preuß, J. A. et al. 2022, *Optica*, 9, 522
- [159] Preuß, J. A., Rudi, E., Kern, J., Schmidt, R., Bratschitsch, R., & de Vasconcellos, S. M. 2021, *2D Materials*, 8, 035005

- [160] Proscia, N. V., Collison, R. J., Meriles, C. A., & Menon, V. M. 2019, *Nanophotonics*, 8, 2057
- [161] Proscia, N. V., Jayakumar, H., Ge, X., Lopez-Morales, G., Shotan, Z., Zhou, W., Meriles, C. A., & Menon, V. M. 2020, *Nanophotonics*, 9, 2937
- [162] Qian, C. et al. 2022, arXiv preprint arXiv:2202.10980
- [163] Ramsay, A. J., Hekmati, R., Patrickson, C. J., Baber, S., Arvidsson-Shukur, D. R. M., Bennett, A. J., & Luxmoore, I. J. 2022, arXiv preprint arXiv:2205.12747
- [164] Re Fiorentin, M., Kiprono, K. K., & Risplendi, F. 2020, *Nanomaterials and Nanotechnology*, 10, 1847980420949349
- [165] Reimers, J. R., Sajid, A., Kobayashi, R., & Ford, M. J. 2018, *Journal of Chemical Theory and Computation*, 14, 1602
- [166] Reimers, J. R., Shen, J., Kianinia, M., Bradac, C., Aharonovich, I., Ford, M. J., & Piecuch, P. 2020, *Physical Review B*, 102, 144105
- [167] Sajid, A., Reimers, J. R., & Ford, M. J. 2018, *Physical Review B*, 97, 064101
- [168] Sajid, A., Reimers, J. R., Kobayashi, R., & Ford, M. J. 2020, *Physical Review B*, 102, 144104
- [169] Sajid, A. & Thygesen, K. S. 2020, *2D Materials*, 7, 031007
- [170] Scavuzzo, A. et al. 2019, *Applied Physics Letters*, 114, 062104
- [171] Schell, A. W., Svedendahl, M., & Quidant, R. 2018, *Advanced Materials*, 30, 1704237
- [172] Schell, A. W., Takashima, H., Tran, T. T., Aharonovich, I., & Takeuchi, S. 2017, *ACS Photonics*, 4, 761
- [173] Schell, A. W., Tran, T. T., Takashima, H., Takeuchi, S., & Aharonovich, I. 2016, *APL Photonics*, 1, 091302
- [174] Schirhagl, R., Chang, K., Loretz, M., & Degen, C. L. 2014, *Annu. Rev. Phys. Chem*, 65, 83
- [175] Schué, L. et al. 2019, *Physical Review Letters*, 122, 067401
- [176] Shandilya, P. K. et al. 2019, *Nano Letters*, 19, 1343
- [177] Shevitski, B. et al. 2019, *Physical Review B*, 100, 155419
- [178] Shotan, Z. et al. 2016, *ACS Photonics*, 3, 2490

- [179] Shulevitz, H. J., Huang, T. Y., Xu, J., Neuhaus, S. J., Patel, R. N., Choi, Y. C., Bassett, L. C., & Kagan, C. R. 2022, *ACS Nano*, 16, 1847
- [180] Smart, T. J., Li, K., Xu, J., & Ping, Y. 2021, *npj Computational Materials*, 7
- [181] Sontheimer, B., Braun, M., Nikolay, N., Sadzak, N., Aharonovich, I., & Benson, O. 2017, *Physical Review B*, 96, 121202
- [182] Spokoyny, B., Utzat, H., Moon, H., Grosso, G., Englund, D., & Bawendi, M. G. 2020, *Journal of Physical Chemistry Letters*, 11, 1330
- [183] Steane, A. 1998, *Reports on Progress in Physics*, 61, 117
- [184] Stern, H. L. et al. 2022, *Nature Communications*, 13
- [185] —. 2019, *ACS Nano*, 13, 4538
- [186] Stewart, J. C. et al. 2021, *ACS Nano*, 15, 13591
- [187] Stoneham, A. M. 1975, *Theory of Defects in Solids* (Clarendon Press, Oxford)
- [188] Strand, J., Larcher, L., & Shluger, A. L. 2020, *Journal of Physics Condensed Matter*, 32, 055706
- [189] Tan, Q. et al. 2022, *Nano Letters*, 22, 1331
- [190] Tawfik, S. A. et al. 2017, *Nanoscale*, 9, 13575
- [191] Toledo, J. R. et al. 2018, *Physical Review B*, 98, 155203
- [192] Toledo, J. R. & Krambrock, K. 2020, *Journal of Physics D: Applied Physics*, 54, 065303
- [193] Tran, T. T., Bray, K., Ford, M. J., Toth, M., & Aharonovich, I. 2016, *Nature Nanotechnology*, 11, 37
- [194] Tran, T. T. et al. 2016, *ACS Nano*, 10, 7331
- [195] Tran, T. T., Wang, D., Xu, Z.-Q., Yang, A., Toth, M., Odom, T. W., & Aharonovich, I. 2017, *Nano Letters*, 17, 2634
- [196] Tran, T. T. et al. 2016, *Physical Review Applied*, 5, 034005
- [197] Turiansky, M. E., Alkauskas, A., Bassett, L. C., & Van De Walle, C. G. 2019, *Physical Review Letters*, 123, 127401
- [198] Turiansky, M. E., Alkauskas, A., Engel, M., Kresse, G., Wickramaratne, D., Shen, J.-X., Dreyer, C. E., & de Walle, C. G. 2021, *Computer Physics Communications*, 267, 108056

- [199] Turiansky, M. E. & Van De Walle, C. G. 2021, *Journal of Applied Physics*, 129, 64301
- [200] Turiansky, M. E. & Van de Walle, C. G. 2021, *2D Materials*, 8, 024002
- [201] Vogl, T., Campbell, G., Buchler, B. C., Lu, Y., & Lam, P. K. 2018, *ACS Photonics*, 5, 2305
- [202] Vogl, T., Doherty, M. W., Buchler, B. C., Lu, Y., & Lam, P. K. 2019, *Nanoscale*, 11, 14362
- [203] Vogl, T., Knopf, H., Weissflog, M., Lam, P. K., & Eilenberger, F. 2021, *Physical Review Research*, 3, 013296
- [204] Vogl, T., Lu, Y., & Koy Lam, P. 2017, *Journal of Physics D: Applied Physics*, 50, 295101
- [205] Vokhmintsev, A., Weinstein, I., & Zamyatin, D. 2019, *Journal of Luminescence*, 208, 363
- [206] Vuong, T. Q. P., Cassabois, G., Valvin, P., Ouerghi, A., Chassagneux, Y., Voisin, C., & Gil, B. 2016, *Physical Review Letters*, 117, 097402
- [207] Wang, Q. et al. 2018, *Nano Letters*, 18, 6898
- [208] Wang, Y., Lee, J., Berezovsky, J., & Feng, P. X. 2021, *Applied Physics Letters*, 118, 244003
- [209] Weston, L., Wickramaratne, D., Mackoite, M., Alkauskas, A., & Van De Walle, C. G. 2018, *Physical Review B*, 97, 214104
- [210] White, S. J., Duong, N. M. H., Solntsev, A. S., Kim, J.-H., Kianinia, M., & Aharonovich, I. 2020, *Physical Review Applied*, 14, 044017
- [211] White, S. J. et al. 2021, *Journal of Optics*, 23, 01LT01
- [212] Wigger, D. et al. 2019, *2D Materials*, 6, 035006
- [213] Winter, M., Bousquet, M. H. E., Jacquemin, D., Duchemin, I., & Blase, X. 2021, *Physical Review Materials*, 5, 095201
- [214] Wolfowicz, G., Heremans, F. J., Anderson, C. P., Kanai, S., Seo, H., Gali, A., Galli, G., & Awschalom, D. D. 2021, *Nature Reviews Materials*, 6, 906
- [215] Wong, D. et al. 2015, *Nature Nanotechnology*, 10, 949
- [216] Wu, F., Galatas, A., Sundararaman, R., Rocca, D., & Ping, Y. 2017, *Physical Review Materials*, 1, 71001

- [217] Xia, Y., Li, Q., Kim, J., Bao, W., Gong, C., Yang, S., Wang, Y., & Zhang, X. 2019, *Nano Letters*, 19, 7100
- [218] Xu, X. et al. 2021, *Nano Letters*, 21, 8182
- [219] Xu, Z. Q. et al. 2018, *Nanoscale*, 10, 7957
- [220] —. 2020, *2D Materials*, 7, 031001
- [221] Xue, Y. et al. 2018, *ACS Nano*, 12, 7127
- [222] Yan, Q., Kioupakis, E., Jena, D., & de Walle, C. G. 2014, *Physical Review B*, 90, 121201
- [223] Yim, D., Yu, M., Noh, G., Lee, J., & Seo, H. 2020, *ACS Applied Materials & Interfaces*, 12, 36362
- [224] You, J. Q. & Nori, F. 2005, *Physics Today*, 58, 42
- [225] Yu, P. et al. 2022, *Nano Letters*, 22, 3545
- [226] Zhang, G., Cheng, Y., Chou, J. P., & Gali, A. 2020, *Applied Physics Reviews*, 7, 031308
- [227] Ziegler, J. et al. 2018, *Nano Letters*, 18, 2683
- [228] Ziegler, J., Klaiss, R., Blaikie, A., Miller, D., Horowitz, V. R., & Alemán, B. J. 2019, *Nano Letters*, 19, 2121
- [229] Zobelli, A., Ewels, C. P., Gloter, A., & Seifert, G. 2007, *Physical Review B*, 75, 094104
- [230] Zunger, A. & Katzir, A. 1975, *Physical Review B*, 11, 2378

ProQuest Number: 29319204

INFORMATION TO ALL USERS

The quality and completeness of this reproduction is dependent on the quality and completeness of the copy made available to ProQuest.



Distributed by ProQuest LLC (2022).

Copyright of the Dissertation is held by the Author unless otherwise noted.

This work may be used in accordance with the terms of the Creative Commons license or other rights statement, as indicated in the copyright statement or in the metadata associated with this work. Unless otherwise specified in the copyright statement or the metadata, all rights are reserved by the copyright holder.

This work is protected against unauthorized copying under Title 17, United States Code and other applicable copyright laws.

Microform Edition where available © ProQuest LLC. No reproduction or digitization of the Microform Edition is authorized without permission of ProQuest LLC.

ProQuest LLC
789 East Eisenhower Parkway
P.O. Box 1346
Ann Arbor, MI 48106 - 1346 USA